Influence of zero-modes on the inertial-range anisotropy of Rayleigh-Taylor and unstably stratified homogeneous turbulence

Olivier Soulard and Benoît-Joseph Gréa
CEA, DAM, DIF, 91297 Arpajon, France
(Received 20 February 2017; published 20 July 2017)

The purpose of this work is to study the anisotropic properties of the inertial range of Rayleigh-Taylor and unstably stratified homogeneous (USH) turbulence. More precisely, we aim to understand the role played by the so-called zero-modes, i.e., modes that nullify the anisotropic part of transfer terms. To this end, we determine several characteristic properties of zero-modes using an eddy-damped quasinormal Markovianized (EDQNM) model. Then we perform a high-Reynolds-number EDQNM simulation of a USH flow and check whether the predicted zero-mode properties are indeed observed in this idealized setting. Finally, we carry out a large-eddy simulation of a Rayleigh-Taylor flow and verify if zero-modes can also be identified in this configuration. Among the main findings of this work, we show that the small-scale anisotropy of the velocity and concentration spectra is dominated by the nonlocal contribution of zero-modes rather than by the local action of buoyancy forces. As a result, we predict inertial scaling exponents close to $-7/3$ (rather than -3) for the second-order harmonics of the velocity and concentration spectra. By contrast, the concentration flux spectrum remains controlled by buoyancy forces. Still, we show that the zero-mode contribution vanishes slowly as the Reynolds number increases. This translates into a slow convergence of the scaling exponent of the second-order harmonic of the concentration flux to $-7/3$.

DOI: 10.1103/PhysRevFluids.2.074603

I. INTRODUCTION

Most theoretical studies dedicated to the small scales of Rayleigh-Taylor turbulence have focused on determining the isotropic properties of the velocity and concentration spectra in the inertial range [1–6], leaving aside the question of anisotropy. Yet, as observed in numerical simulations [7], anisotropy has a strong imprint on inertial scales and requires a description of its own.

One of the first attempts at explaining Rayleigh-Taylor inertial-range anisotropy was made in Ref. [8]. In this work, anisotropy was considered to be induced by buoyancy forces in the form of a small perturbation around the isotropic Kolmogorov-Obukhov spectrum. This perturbation was then studied with the help of the spectral Langevin model proposed in Ref. [9]. The latter predicts the existence, in the inertial range, of a local equilibrium between the anisotropic components of the nonlinear transfer terms and buoyancy production. The outcome of this equilibrium is an anisotropic perturbation of the velocity and concentration spectrum proportional to a second-order angular harmonic and scaling as N^2k^{-3}, with N the stratification frequency and k the wave number. This result is fully compatible with the dimensional analysis initiated in Ref. [10] and extended to stratified flows in Ref. [11], and which initially motivated the study developed in Ref. [8]. Note that the dimensional analysis of [11] finds its roots in the work of Lumley [12,13] and that developments similar to those in Ref. [8] were made in Ref. [14] in the context of stably stratified turbulence. Note also that the smallness of buoyancy forces compared to their inertial counterpart was first emphasized in Ref. [15].

In the meantime, an idealized version of Rayleigh-Taylor turbulence, called unstably stratified homogeneous (USH) turbulence, was proposed [16–21]. The interesting aspect of USH turbulence is that it retains all the ingredients of Rayleigh-Taylor turbulence except for inhomogeneity. Therefore, with the assumption that Rayleigh-Taylor small scales are quasihomogeneous, it is expected that

Rayleigh-Taylor and USH inertial ranges display similar features. In fact, this expectation was already implicitly used in Ref. [8] to predict the properties of Rayleigh-Taylor small scales: The spectral Langevin model used in Ref. [8] strictly applies to USH turbulence, but its range of validity was implicitly extended to Rayleigh-Taylor small scales under the condition that they are quasihomogeneous. Indeed, the similarity between USH and Rayleigh-Taylor inertial ranges was verified in several direct numerical simulations (DNSs) of USH and Rayleigh-Taylor turbulence [8,16]. In particular, most of the scalings and angular dependences predicted in Ref. [8] appeared to be verified in both types of configuration.

However, the Rayleigh-Taylor and USH verification of the predictions made in Ref. [8] could only be performed at moderate Reynolds numbers, i.e., up to a Taylor Reynolds number on the order of 100. To overcome this limitation, an eddy-damped quasinormal Markovianized (EDQNM) model was proposed for USH turbulence and thoroughly validated against DNS [19,21]. Then this model was used to explore higher Reynolds numbers [20,21]. What was observed in Refs. [20,21] was a systematic departure from the predictions made in Ref. [8]. In particular, at the largest wave numbers, the anisotropy of the velocity spectrum was found to scale closer to $k^{-7/3}$ than to k^{-3}. Therefore, the question arises as to the origin of this discrepancy.

To answer this question, we note a fundamental difference between the spectral Langevin model used in Ref. [8] and the EDQNM model used in Ref. [20]. The former model uses an extremely simplified description of the anisotropic components of nonlinear transfer terms. This simplification allows for only one possible local anisotropic equilibrium between nonlinear transfer terms and buoyancy forces. This in turn leads to a unique characterization of the anisotropic perturbation around the isotropic Kolmogorov-Obukhov spectrum, with a fixed k^{-3} scaling. By contrast, the EDQNM model, which retains more physics in its description of the anisotropy of nonlinear transfer terms, allows for a whole family of equilibrium solutions. This family consists in the sum of a particular solution ensuring the balance between transfer and buoyancy forces and a set of homogeneous solutions that have a zero contribution to anisotropic nonlinear transfer terms. This general structure was put forth in Ref. [22], albeit in the context of shear flows and for a Lagrangian renormalization approximation. The homogeneous contributions are called zero-modes and their study is referred to as zero-mode analysis.

Zero-mode analysis has allowed to make tremendous progress in the characterization of the inertial range anisotropy of a wide variety of configurations [23], including shear flows [24], passive scalar advection [25], or magnetic-field advection [26]. It has also been applied to very diverse models [23,27]. In particular, it has been used to analyze the anisotropic properties of a direct-interaction approximation model for the velocity field [24]. In the inertial range, the formulation of this model is almost identical to an EDQNM model, so the results obtained in Ref. [24] are directly relevant to our situation. One of the main result obtained in Ref. [24] is that the second-order harmonic of the velocity field's zero-modes scales approximately as $k^{-7/3}$.

This suggests that the presence of zero-modes can possibly explain the difference between the observations made in Ref. [20] and the predictions made in Ref. [8]. However, one may in principle imagine other mechanisms leading to a $k^{-7/3}$ anisotropy. Therefore, a further characterization of zero-modes is required to ensure that they are indeed responsible for what is seen in Ref. [20]. Besides, even if small, differences in the closures used in Refs. [19,24] exist. The effects of these differences should be looked at. Finally, if zero-modes are present, they should modify not only the velocity spectrum but also the concentration spectrum and the concentration flux spectrum. The presence of zero-modes for these spectra should also be investigated. In particular, the local equilibrium described in Ref. [8] predicts a $k^{-7/3}$ scaling for the concentration flux spectrum. This scaling appears to be reached in the simulations of [20], but with a very slow convergence in terms of Reynolds number. Such a slow convergence was also observed in a different context in Refs. [28,29]. The potential role played by zero-modes in this slow convergence should be probed.

Thus, the purpose of this work is to examine, with the help of an EDQNM model, the influence of zero-modes on the inertial-range anisotropy of Rayleigh-Taylor and unstably stratified homogeneous turbulence. To this end, we start with the previously mentioned idea that the inertial range

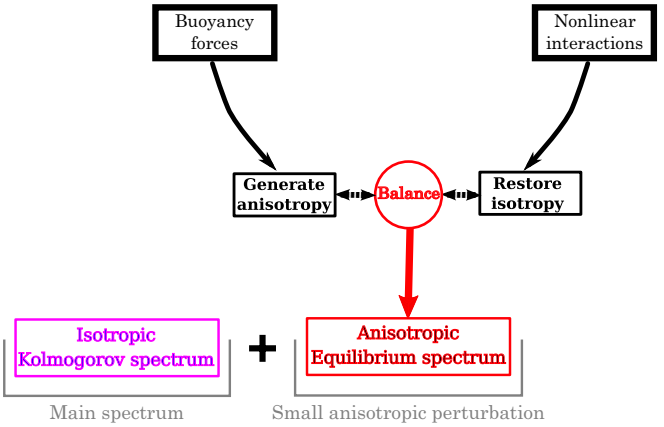

FIG. 1. Sketch of the idea followed in Ref. [8] to analyze the inertial-range anisotropy of Rayleigh-Taylor and USH turbulence.

properties of Rayleigh-Taylor and USH turbulence are similar. This idea stems from the expected quasihomogeneity of Rayleigh-Taylor small scales and from the verification already performed in Ref. [16]. Given the ability of the EDQNM model proposed in Ref. [19] to reproduce DNS simulations of USH turbulence, we assume that this model provides a sufficiently accurate description of USH small scales and by extension of Rayleigh-Taylor small scales. Equipped with this model, we apply the methodology developed in Ref. [24] to find zero-modes and study some of their properties. Then we sum the found zero-modes with the equilibrium spectra already derived in Ref. [8] and examine how the two contributions interact. Finally, we perform a validation in two steps. First, we carry out an EDQNM simulation of USH turbulence at a Reynolds number of 10^7. Second, we complete a large-eddy simulation (LES) of a Rayleigh-Taylor flow. In both cases, we attempt to determine whether zero-modes can be identified or not and if their properties are consistent with the zero-mode analysis.

II. FURTHER CONSIDERATION OF ZERO-MODES AND EQUILIBRIUM SPECTRA

Before entering the core of the subject, we would like to rephrase some of the statements already made in the Introduction in order to clarify further the key physical ideas that form the backbone of this study. First of all, we would like to recall the description of inertial range anisotropy initially proposed in Ref. [8] for Rayleigh-Taylor turbulence and emphasize its shortcomings. This description is schematized in Fig. 1. As already explained in the Introduction, it consists in assuming that, in the inertial range, buoyancy forces induce a small anisotropic perturbation around the isotropic Kolmogorov spectrum. By contrast, nonlinear effects are considered to restore isotropy and to counteract the action of buoyancy forces. The balance of the two processes leads to the emergence of an anisotropic equilibrium spectrum. in Ref. [8], this balance was studied with the help of the spectral Langevin model proposed in Ref. [9], but the overall idea stands independently of this particular choice. The main predictions made in Ref. [8] are the following: The equilibrium contribution exhibits a second-order-harmonic angular dependence and scales as k^{-3} for the velocity and concentration spectra and as $k^{-7/3}$ for the concentration flux spectrum. These scalings are compatible with dimensional arguments, such as those proposed in Refs. [11,13].

The issue with these results comes from the physical idea followed in Ref. [8] and schematized in Fig. 1. This idea oversimplifies the role played by nonlinear interactions: Nonlinear interactions may not only restore isotropy, also promote anisotropy. For instance, they can transfer information from large anisotropic scales to small more isotropic ones or exchange anisotropy between the different components of the spectra, some of which may be more anisotropic than others. Because of these

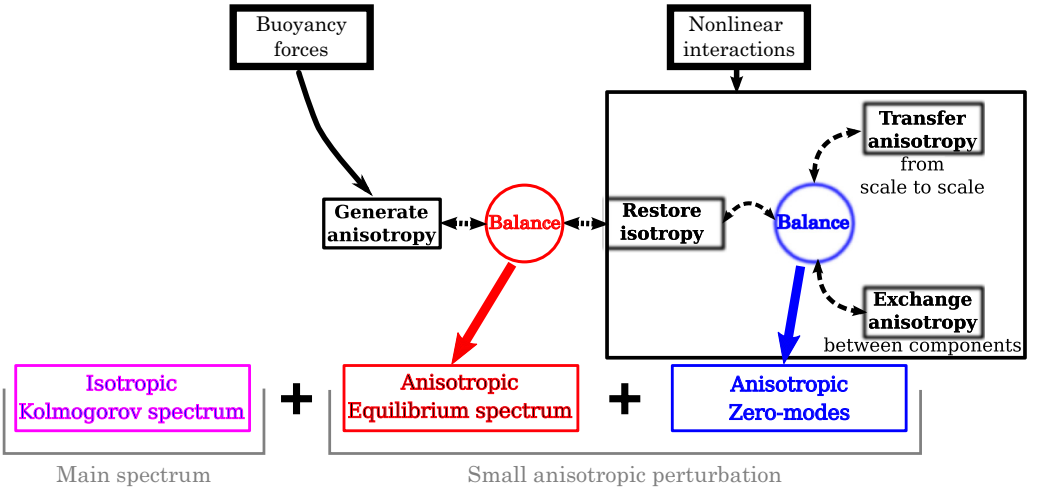

FIG. 2. Sketch of the idea followed in this work to analyze the inertial-range anisotropy of Rayleigh-Taylor and USH turbulence.

antagonizing effects, an additional balance, involving only nonlinear interactions, can take place. When this happens, zero-mode spectra emerge [22–27]. The latter denomination comes from the fact that zero-modes cancel out the nonlinear transfer terms of the turbulent spectra or at least their anisotropic part. This physical description of inertial-range anisotropy is schematized in Fig. 2.

Zero-modes do not replace equilibrium spectra but are superimposed with them [22]. One of the question we would like to address in this work is how the inclusion of zero-modes modifies the predictions originally made in Ref. [8]. In particular, we would like to determine whether the zero-mode contributions decay faster or slower than their equilibrium counterparts, i.e., to determine which of these contributions becomes predominant when the wave number k becomes large.

This question, asked in terms of scalings, has deep physical implications. Its answer determines which mechanism sustains anisotropy for small inertial scales: Is small-scale anisotropy generated locally by the direct action of buoyancy forces or is it maintained by the nonlocal action of nonlinear interactions?

III. THE EDQNM MODEL FOR USH TURBULENCE

As explained in the Introduction, the expected quasihomogeneity of Rayleigh-Taylor small scales and the verification already performed in Ref. [16] suggests a close similarity between the inertial range properties of Rayleigh-Taylor and USH turbulence. Hence, we will hereafter focus on the latter simpler configuration and apply the results derived for it to Rayleigh-Taylor turbulence. In this section, we start by recalling the governing equations of USH turbulence, along with the main assumptions underlying the definition of this idealized flow. Then we recall the evolution equations of the EDQNM model proposed in Ref. [19] for USH turbulence.

A. Governing equations of USH turbulence

We consider a turbulent flow submitted to a gravitational field. We denote by $\hat{\boldsymbol{n}}$ the direction of gravity and we introduce a Cartesian frame $(\boldsymbol{e}_1,\boldsymbol{e}_2,\boldsymbol{e}_3)$ such that $\boldsymbol{e}_1$ and $\boldsymbol{e}_2$ are transverse to $\hat{\boldsymbol{n}}$ while $\boldsymbol{e}_3$ is equal to it: $\boldsymbol{e}_3 = \hat{\boldsymbol{n}}$. We assume that two incompressible fluids with densities ρ_h and $\rho_l < \rho_h$ are being mixed and that their Atwood number $\mathtt{A}_t = (\rho_h - \rho_l)/(\rho_l + \rho_h)$ is small compared to one. The Boussinesq approximation can then be applied to the Navier-Stokes equations. In addition, as in stably stratified turbulence [11,30–35], we assume that turbulence is homogeneous and that mean

gradients are uniform in space. With these hypotheses, we obtain the following evolutions for the velocity and concentration fluctuations in USH turbulence:

$$\partial_{t^\star} c^\star + u_j^\star \partial_j^\star c^\star = \frac{u_3^\star}{L} + \nu^\star \partial_{jj}^\star c^\star, \tag{1a}$$

$$\partial_{t^\star} u_i^\star + u_j^\star \partial_j^\star u_i^\star = -\partial_i^\star p^\star + 2\mathtt{A}_t g c^\star \delta_{i3} + \nu^\star \partial_{jj}^\star u_i^\star, \tag{1b}$$

$$\partial_j^\star u_j^\star = 0, \tag{1c}$$

with $t^\star$ the time and $u_i^\star$, $c^\star$, and $p^\star$ the respective fluctuations of the velocity field, of the concentration of one of the fluids, and of the reduced pressure. We also denote by g the intensity of the gravity field, constant in time and uniform, and by L the opposite of the inverse of the mean concentration gradient (which has been assumed to be uniform). For the sake of simplicity, the Schmidt number is taken equal to one so that the same molecular diffusion coefficient $\nu^\star$ appears in the velocity and concentration equations. The Einstein convention on the summation of indices is used and the notation $\partial_j^\star$ refers to the partial derivative with respect to $x_j^\star$, the spatial coordinate in the direction $\boldsymbol{e}_j$.

Because of the quasihomogeneity assumption, the evolution of the mean flow only appears in the system of equations (1) through the definition of L. In this work, we consider one of the simplest choice for setting L. As in Refs. [19–21], we assume that L is constant in time: $\partial_{t^\star} L = 0$. Other choices are possible in order to mimic more closely the evolution of a Rayleigh-Taylor mixing zone [16,17], but they have little incidence on the anisotropic properties of inertial scales compared to their simpler counterpart.

In order to simplify the analysis, we now introduce variables nondimensionalized by L and $\mathtt{A}_t g$. These two quantities can be combined to define a buoyancy or Brunt-Väissällä frequency N as well as a stratification velocity V_N:

$$N = \sqrt{\frac{2\mathtt{A}_t g}{L}}, \quad V_N = \sqrt{2\mathtt{A}_t g L}.$$

Using these mean flow characteristics, we nondimensionalize time $t^\star$, space coordinates $\boldsymbol{x}^\star$, and molecular diffusion $\nu^\star$, as well as the velocity field $\boldsymbol{u}^\star$, the reduced pressure $p^\star$, and the concentration $c^\star$ as follows:

$$dt = N dt^\star, \quad x_i = \frac{x_i^\star}{L}, \quad u_i = \frac{u_i^\star}{V_N}, \quad p = \frac{p^\star}{V_N^2}, \quad c = c^\star, \quad \nu = \frac{\nu^\star}{V_N^2/N}. \tag{2}$$

With these assumptions and notation, the dimensionless fluctuating field of a USH turbulent flow with constant g and L evolves as

$$\partial_t c + u_j \partial_j c = u_3 + \nu \partial_{jj}^2 c, \tag{3a}$$

$$\partial_t u_i + u_j \partial_j u_i = -\partial_i p + c\delta_{i3} + \nu \partial_{jj}^2 u_i, \tag{3b}$$

$$\partial_j u_j = 0. \tag{3c}$$

B. The EDQNM model equations

We introduce $\boldsymbol{u}^{\mathrm{F}}(\boldsymbol{k})$ and $c^{\mathrm{F}}(\boldsymbol{k})$, the Fourier transforms with respect to $\boldsymbol{x}$ of the velocity and concentration fields, taken at a given wave vector $\boldsymbol{k}$. We then define the velocity spectrum $\boldsymbol{R}$, the concentration spectrum B, and the concentration flux spectrum $\boldsymbol{F}$ as follows:

$$R_{ab}(\boldsymbol{k})\delta(\boldsymbol{k}+\boldsymbol{k}') = \tfrac{1}{2}\big[\overline{u_a^{\mathrm{F}}(\boldsymbol{k}) u_b^{\mathrm{F}}(\boldsymbol{k}')} + \overline{u_a^{\mathrm{F}}(\boldsymbol{k}') u_b^{\mathrm{F}}(\boldsymbol{k})}\big],$$

$$B(\boldsymbol{k})\delta(\boldsymbol{k}+\boldsymbol{k}') = \overline{c^{\mathrm{F}}(\boldsymbol{k}) c^{\mathrm{F}}(\boldsymbol{k}')},$$

$$F_a(\boldsymbol{k})\delta(\boldsymbol{k}+\boldsymbol{k}') = \tfrac{1}{2}\big[\overline{u_a^{\mathrm{F}}(\boldsymbol{k}) c^{\mathrm{F}}(\boldsymbol{k}')} + \overline{u_a^{\mathrm{F}}(\boldsymbol{k}') c^{\mathrm{F}}(\boldsymbol{k})}\big],$$

where $\overline{Q}$ refers to the average of a given quantity Q. The evolution equations for these spectra can be derived from the system of equations (3). They take the form

$$(\partial_t + 2\nu k^2)R_{ab}(\boldsymbol{k}) = T^R_{ab}(\boldsymbol{k}) + P_{a3}(\hat{\boldsymbol{k}})F_b(\boldsymbol{k}) + P_{b3}(\hat{\boldsymbol{k}})F_a(\boldsymbol{k}), \tag{4a}$$

$$(\partial_t + 2\nu k^2)B(\boldsymbol{k}) = T^B(\boldsymbol{k}) + 2F_3(\boldsymbol{k}), \tag{4b}$$

$$(\partial_t + 2\nu k^2)F_a(\boldsymbol{k}) = T^F_a(\boldsymbol{k}) + P_{a3}(\hat{\boldsymbol{k}})B(\boldsymbol{k}) + R_{a3}(\boldsymbol{k}), \tag{4c}$$

where P_{ab} is the projector on incompressible fields

$$P_{ab}(\hat{\boldsymbol{k}}) = \delta_{ab} - \hat{k}_a\hat{k}_b.$$

Note that, for a given vector $\boldsymbol{v}$, we use the denotations v and $\hat{\boldsymbol{v}}$ to refer, respectively, to its modulus and to its direction. For instance, k is the modulus of $\boldsymbol{k}$ and $\hat{\boldsymbol{k}}$ is its direction

$$k = \sqrt{k_i k_i}, \quad \hat{\boldsymbol{k}} = \frac{\boldsymbol{k}}{k}.$$

The nonlinear transfer terms of the velocity, concentration, and concentration flux spectra are respectively denoted by $\boldsymbol{T}^R$, T^B, and $\boldsymbol{T}^F$. Their exact definitions can be deduced from Eq. (3) and can be found, for instance, in Ref. [19]. In this work, we will only use their modeled expressions obtained with the EDQNM closure detailed in Ref. [19] and based on standard EDQNM procedures that are explained, for instance, in Refs. [36,37].

The closed EDQNM expressions of T^R_{ab}, T^B, and T^F_a proposed in Ref. [19] are the following:

$$\begin{aligned} T^R_{ab}(\boldsymbol{k}) = \frac{k}{2}\mathcal{P}_{alm}(\hat{\boldsymbol{k}}) \int_{\boldsymbol{k}+\boldsymbol{k}'+\boldsymbol{k}''=0} d\boldsymbol{k}'\Theta_{kk'k''}[k\mathcal{P}_{bij}(\hat{\boldsymbol{k}})R_{il}(\boldsymbol{k}')R_{jm}(\boldsymbol{k}'') \\ + k'\mathcal{P}_{lij}(\hat{\boldsymbol{k}}')R_{ib}(\boldsymbol{k})R_{jm}(\boldsymbol{k}'') + k''\mathcal{P}_{mij}(\hat{\boldsymbol{k}}'')R_{ib}(\boldsymbol{k})R_{jl}(\boldsymbol{k}')] + \text{Sym. } a \leftrightarrow b, \end{aligned} \tag{5a}$$

$$\begin{aligned} T^B(\boldsymbol{k}) = 2k_i \int_{\boldsymbol{k}+\boldsymbol{k}'+\boldsymbol{k}''=0} d\boldsymbol{k}'\Theta_{kk'k''}\{k_j[F_i(\boldsymbol{k}'')F_j(\boldsymbol{k}') + R_{ij}(\boldsymbol{k}'')B(\boldsymbol{k}')] \\ + k'_j[F_i(\boldsymbol{k}'')F_j(\boldsymbol{k}) + R_{ij}(\boldsymbol{k}'')B(\boldsymbol{k})] + k''\mathcal{P}_{ijm}(\hat{\boldsymbol{k}}'')F_m(\boldsymbol{k}')F_j(\boldsymbol{k})\}, \end{aligned} \tag{5b}$$

$$\begin{aligned} T^F_a(\boldsymbol{k}) = \frac{k}{2}\mathcal{P}_{alm}(\hat{\boldsymbol{k}}) \int_{\boldsymbol{k}+\boldsymbol{k}'+\boldsymbol{k}''=0} d\boldsymbol{k}'\Theta_{kk'k''}\{k_j[R_{lj}(\boldsymbol{k}')F_m(\boldsymbol{k}'') + R_{mj}(\boldsymbol{k}'')F_l(\boldsymbol{k}')] \\ + k'\mathcal{P}_{ljn}(\boldsymbol{k}')R_{mn}(\boldsymbol{k}'')F_j(\boldsymbol{k}) + k''\mathcal{P}_{mjn}(\boldsymbol{k}'')R_{ln}(\boldsymbol{k}')F_j(\boldsymbol{k})\} \\ + k_j \int_{\boldsymbol{k}+\boldsymbol{k}'+\boldsymbol{k}''=0} d\boldsymbol{k}'\Theta_{kk'k''}\{k'_n[R_{nj}(\boldsymbol{k}'')F_a(\boldsymbol{k}) + F_j(\boldsymbol{k}'')R_{na}(\boldsymbol{k})] \\ + k\mathcal{P}_{anm}(\hat{\boldsymbol{k}})R_{mj}(\boldsymbol{k}'')F_n(\boldsymbol{k}') + k''\mathcal{P}_{jnm}(\hat{\boldsymbol{k}}'')R_{ma}(\boldsymbol{k})F_n(p)\}, \end{aligned} \tag{5c}$$

where

$$\mathcal{P}_{ajm}(\hat{\boldsymbol{k}}) = \hat{k}_j P_{am}(\hat{\boldsymbol{k}}) + \hat{k}_m P_{aj}(\hat{\boldsymbol{k}}), \quad \Theta_{kk'k''} = \frac{1}{\nu(k^2 + k'^2 + k''^2) + \eta(k) + \eta(k') + \eta(k'')}.$$

The time scale $\Theta_{kk'k''}$ models the effects of eddy damping as well as the time history of the triple correlations. Its expression is given here for large times. As for the eddy-damping inverse time scale $\eta(k)$, it is defined as

$$\eta(k) = a_0\left(\int_0^k p^2 E(p)dp\right)^{1/2} + a_1 N,$$

with $a_0 = 0.36$, $a_1 = 0.33$, and $E(k) = \frac{k^2}{2}\int R_{jj}(\boldsymbol{k})d\hat{\boldsymbol{k}}$. Compared to the standard formulation of the EDQNM model, a contribution linked to buoyancy effects $a_1 N$ has been added. This contribution

was found to be necessary to ensure good agreement between DNS and EDQNM simulations in Ref. [19].

IV. LINEARIZATION OF THE EDQNM MODEL

Central to this work is the assumption that inertial-range anisotropy is weak. The purpose of this section is to summarize this assumption and to examine its consequences on the expression of the nonlinear transfer terms modeled by the EDQNM closure given by Eqs. (5).

A. Weak anisotropy hypothesis

We consider a USH turbulent flow with a very large Reynolds number and look at the properties of the turbulent spectra within the corresponding inertial range. As in Refs. [8,10,11,24], we assume that, in this inertial range, the anisotropic components of the turbulent spectra exist in the form of a small perturbation around the isotropic Kolmogorov-Obukhov spectrum. Thus, we decompose the velocity and concentration spectra as

$$\boldsymbol{R}(\boldsymbol{k}) = \boldsymbol{R}^{\mathrm{KO}}(\boldsymbol{k}) + \boldsymbol{r}(\boldsymbol{k}), \quad B(\boldsymbol{k}) = B^{\mathrm{KO}}(\boldsymbol{k}) + b(\boldsymbol{k}), \quad \boldsymbol{F}(\boldsymbol{k}) = \boldsymbol{F}^{\mathrm{KO}}(\boldsymbol{k}) + \boldsymbol{f}(\boldsymbol{k}), \tag{6}$$

where $\boldsymbol{R}^{\mathrm{KO}}$, B^{KO}, and $\boldsymbol{F}^{\mathrm{KO}}$ denote the Kolmogorov-Obukhov spectrum

$$R_{ab}^{\mathrm{KO}}(\boldsymbol{k}) = \frac{E^{\mathrm{KO}}(k)}{4\pi k^2} P_{ab}(\hat{\boldsymbol{k}}), \quad B^{\mathrm{KO}}(\boldsymbol{k}) = \frac{E_B^{\mathrm{KO}}(k)}{4\pi k^2}, \quad F_a^{\mathrm{KO}}(\boldsymbol{k}) = 0, \tag{7a}$$

with

$$E^{\mathrm{KO}}(k) = c_K \overline{\varepsilon}^{2/3} k^{-5/3}, \quad E_B^{\mathrm{KO}}(k) = c_O \overline{\varepsilon}_B \overline{\varepsilon}^{-1/3} k^{-5/3}, \tag{7b}$$

with $\overline{\varepsilon} = \nu \overline{\partial_j u_i \partial_j u_i}$ and $\overline{\varepsilon}_B = 2\nu \overline{\partial_j c \partial_j c}$ the respective dissipations of the kinetic energy and of the scalar variance, with c_K the Kolmogorov constant and c_O the Obukhov constant. The perturbation around the Kolmogorov-Obukhov spectrum is denoted by $\boldsymbol{r}$, b, and $\boldsymbol{f}$ and is assumed to verify

$$\|\boldsymbol{r}(\boldsymbol{k})\| \ll \|\boldsymbol{R}^{\mathrm{KO}}(\boldsymbol{k})\|, \quad |b(\boldsymbol{k})| \ll B^{\mathrm{KO}}(\boldsymbol{k}), \quad |\boldsymbol{f}(\boldsymbol{k})| = \sqrt{f_a(\boldsymbol{k}) f_a(\boldsymbol{k})} \ll \sqrt{R_{jj}^{\mathrm{KO}}(\boldsymbol{k}) B^{\mathrm{KO}}(\boldsymbol{k})}. \tag{8}$$

In order to characterize further the anisotropy of the perturbation spectra, we decompose them into spherical harmonics. Before doing so, we first recall that the velocity spectrum $\boldsymbol{r}$ can be split into an isotropic, a polarization, and a directional contribution (see [38,39]) and the scalar spectrum b into an isotropic and a directional one:

$$r_{ab}(\boldsymbol{k}) = r_{ab}^{\mathrm{iso}}(\boldsymbol{k}) + r_{ab}^{\mathrm{dir}}(\boldsymbol{k}) + r_{ab}^{\mathrm{pol}}(\boldsymbol{k}), \quad b(\boldsymbol{k}) = b^{\mathrm{iso}}(k) + b^{\mathrm{dir}}(\boldsymbol{k}), \tag{9}$$

with

$$r_{ab}^{\mathrm{iso}}(\boldsymbol{k}) = \frac{r_0(k)}{4\pi\kappa^2} P_{ab}(\hat{\boldsymbol{k}}), \quad b^{\mathrm{iso}}(k) = \frac{b_0(k)}{4\pi\kappa^2}, \quad r_0(k) = \frac{k^2}{2} \int r_{jj}(\boldsymbol{k}) d\hat{\boldsymbol{k}}, \quad b_0(k) = k^2 \int b(\boldsymbol{k}) d\hat{\boldsymbol{k}},$$

$$r_{ab}^{\mathrm{dir}}(\boldsymbol{k}) = \left(\frac{1}{2} r_{jj}(\boldsymbol{k}) - \frac{r_0(k)}{4\pi\kappa^2} \right) P_{ab}(\hat{\boldsymbol{k}}), \quad b^{\mathrm{dir}}(\boldsymbol{k}) = b(\boldsymbol{k}) - b^{\mathrm{iso}}(k),$$

$$r_{ab}^{\mathrm{pol}}(\boldsymbol{k}) = r_{ab}(\boldsymbol{k}) - \frac{1}{2} r_{jj}(\boldsymbol{k}) P_{ab}(\hat{\boldsymbol{k}}),$$

where $\int \cdots d\hat{\boldsymbol{k}}$ refers to the integration over the surface of the unit sphere of normal $\hat{\boldsymbol{k}}$. The directional anisotropy of $\boldsymbol{r}$ (b) measures the differences in energy (scalar variance) carried along each wave-vector direction $\hat{\boldsymbol{k}}$ at a given $|\boldsymbol{k}|$. As for the polarization anisotropy of $\boldsymbol{r}$, it measures the differences between the intensities of the components of the Fourier transform of the velocity u_a^{F} at a given wave number $\boldsymbol{k}$. More details can be found in Ref. [38]. Note that the flux $\boldsymbol{f}$ was

also decomposed into an isotropic and a directional component in Ref. [8], but this notion is rather ambiguous and is dropped in favor of a more general harmonic decomposition.

We also recall that the flow is symmetric around the axis $\hat{\boldsymbol{n}} = \boldsymbol{e}_3$, so we only need to consider circular harmonics depending on $\cos\theta$, the cosine of the angle between the direction of the wave vector $\hat{\boldsymbol{k}}$ and $\hat{\boldsymbol{n}}$:

$$\cos\theta = \hat{\boldsymbol{k}} \cdot \hat{\boldsymbol{n}}.$$

With these specifications, we can now expand $\boldsymbol{r}$, b, and $\boldsymbol{f}$ using spherical harmonics as follows:

$$4\pi k^2 r_{ab}^{\mathrm{dir}}(\boldsymbol{k}) = P_{ab}(\hat{\boldsymbol{k}}) \sum_{\ell \geqslant 2} r_\ell^{\mathrm{dir}}(k) Y_\ell(\cos\theta), \quad 4\pi k^2 r_{ab}^{\mathrm{pol}}(\boldsymbol{k}) = D_{ab}(\hat{\boldsymbol{k}},\hat{\boldsymbol{n}}) \sum_{\ell \geqslant 2} r_\ell^{\mathrm{pol}}(k) \ddot{Y}_\ell(\cos\theta), \tag{10a}$$

$$4\pi k^2 f_a(\boldsymbol{k}) = P_{a3}(\hat{\boldsymbol{k}}) \sum_{\ell \geqslant 2} f_\ell(k) \dot{Y}_{\ell-1}(\cos\theta), \quad 4\pi k^2 b^{\mathrm{dir}}(\boldsymbol{k}) = \sum_{\ell \geqslant 2} b_\ell(k) Y_\ell(\cos\theta), \tag{10b}$$

with

$$r_\ell^{\mathrm{dir}}(k) = \frac{2\ell+1}{2} k^2 \int r_{ab}(\boldsymbol{k}) P_{ab}(\hat{\boldsymbol{k}}) Y_\ell(\cos\theta) d\hat{\boldsymbol{k}}, \tag{10c}$$

$$r_\ell^{\mathrm{pol}}(k) = \frac{2(2\ell+1)}{(\ell-1)\ell(\ell+1)(\ell+2)} k^2 \int r_{ab}(\boldsymbol{k}) D_{ab}(\hat{\boldsymbol{k}},\hat{\boldsymbol{n}}) \ddot{Y}_\ell(\cos\theta) d\hat{\boldsymbol{k}}, \tag{10d}$$

$$f_\ell(k) = \frac{2\ell-1}{(\ell-1)\ell} k^2 \int f_a(\boldsymbol{k}) P_{a3}(\hat{\boldsymbol{k}}) \dot{Y}_{\ell-1}(\cos\theta) d\hat{\boldsymbol{k}}, \tag{10e}$$

$$b_\ell(k) = (2\ell+1) k^2 \int b(\boldsymbol{k}) Y_\ell(\cos\theta) d\hat{\boldsymbol{k}}, \tag{10f}$$

where $Y_\ell(x)$ is the standard Legendre polynomial of order ℓ, $\dot{Y}_\ell$ its derivative, and $\ddot{Y}_\ell$ its second-order derivative (the notation Y_ℓ is used instead of the more common one P_ℓ in order to avoid confusion with the projector P_{ab}). The tensor D_{ab} is defined as

$$D_{ab}(\hat{\boldsymbol{k}},\hat{\boldsymbol{n}}) = \mathcal{D}_{abcd}(\hat{\boldsymbol{k}}) n_c n_d, \tag{11}$$

with

$$\mathcal{D}_{abcd}(\hat{\boldsymbol{k}}) = \frac{P_{ab}(\hat{\boldsymbol{k}}) P_{cd}(\hat{\boldsymbol{k}})}{2} - P_{ac}(\hat{\boldsymbol{k}}) P_{bd}(\hat{\boldsymbol{k}}).$$

The decomposition of b^{dir} corresponds to the standard circular harmonic one. The decomposition of $\boldsymbol{f}$ uses the vector spherical harmonic expansion detailed, for instance, in Ref. [40]. This decomposition relies on the expansion of each of the components of $\boldsymbol{f}$ in the spherical basis based on $\hat{\boldsymbol{k}}$. The latter is also referred to as the poloidal-toroidal basis in spectral space [36]. Because of the axisymmetry of the flow and of the incompressibility condition, only the poloidal component of $\boldsymbol{f}$ is nonzero, which explains why only one circular harmonic is sufficient to describe $\boldsymbol{f}$. As for $\boldsymbol{r}^{\mathrm{dir}}$ and $\boldsymbol{r}^{\mathrm{pol}}$, we applied the same formalism as in Ref. [24], with a slight modification to obtain an orthogonal basis. in Ref. [24], $\boldsymbol{r}$ was expanded along the basis $B_{1,\ell}^{ab}(\hat{\boldsymbol{k}}) = P_{ab} Y_\ell(\cos\theta)$ and $B_{2,\ell}^{ab}(\hat{\boldsymbol{k}}) = k^{-\ell}[k^2 \partial_a \partial_b - (\ell - 1)(k_b \partial_a + k_a \partial_b) + \ell(\ell-1)\delta_{ab}][k^\ell Y_\ell(\cos\theta)]$. In Eq. (10) we retained $B_{1,\ell}^{ab}(\hat{\boldsymbol{k}})$ but instead of $B_{2,\ell}^{ab}(\hat{\boldsymbol{k}})$ we used $B_{3,\ell}^{ab}(\hat{\boldsymbol{k}}) = \ell(\ell-1) B_{1,\ell}^{ab}(\hat{\boldsymbol{k}})/2 - B_{2,\ell}^{ab}(\hat{\boldsymbol{k}}) = D_{ab}(\hat{\boldsymbol{k}},\hat{\boldsymbol{n}}) \ddot{Y}_\ell(\cos\theta)$. An advantage of this choice is that $B_{1,\ell}$ and $B_{3,\ell}$ are orthogonal, due to the relation $P_{ij} D_{ij} = 0$. Another advantage of this choice is that the resulting decomposition of $\boldsymbol{r}$ gives direct access to the polarization and directional contributions of $\boldsymbol{r}$. Note that an almost identical variant of the decomposition proposed in Ref. [24] has already been described in Ref. [39].

Also, we would like to stress that given the parities of $\boldsymbol{r}$, $\boldsymbol{f}$, and b, only even values of ℓ need to be taken into account in the sums present in Eqs. (10) and that the spectra r_0 and b_0 introduced in

Eqs. (9) correspond to the order 0 of the harmonic decomposition of $\boldsymbol{r}^{\mathrm{dir}}$ and b. In addition, we note that the weak anisotropy condition (8) implies that, for $\ell \geqslant 2$,

$$\left|r_\ell^{\mathrm{dir}}(k)\right| \ll E^{\mathrm{KO}}(k), \quad \left|r_\ell^{\mathrm{pol}}(k)\right| \ll E^{\mathrm{KO}}(k), \quad |b_\ell(k)| \ll E_B^{\mathrm{KO}}(k), \quad |f_\ell(k)| \ll \sqrt{E^{\mathrm{KO}}(k)E_B^{\mathrm{KO}}(k)}.$$

To conclude the description of the anisotropic perturbation spectra, we hereafter assume that, in the inertial range, r_ℓ^{dir}, r_ℓ^{pol}, f_ℓ, and b_ℓ obey a power law

$$r_\ell^{\mathrm{dir}}(k) = c_\ell^{\mathrm{dir}} k^{-\xi_\ell}, \quad r_\ell^{\mathrm{pol}}(k) = c_\ell^{\mathrm{pol}} k^{-\xi_\ell}, \quad f_\ell(k) = c_\ell^F k^{-\xi_\ell^F}, \quad b_\ell(k) = c_\ell^B k^{-\xi_\ell^B}, \tag{12}$$

where c_ℓ^{dir}, c_ℓ^{pol}, c_ℓ^F, and c_ℓ^B are parameters independent of k and ξ_ℓ, ξ_ℓ^F, and ξ_ℓ^B are the inertial range exponents of the harmonics of order ℓ of the different spectra.

B. Linearization of the EDQNM transfer terms

We now inject the weak anisotropy decomposition (6) with the condition (8) into the EDQNM transfer terms defined by Eq. (5). Considering that the inertial range has an infinite extent, the contribution of the isotropic Kolmogorov-Obukhov spectrum to the transfer terms is equal to 0: Replacing R_{ab}, B, and F_a by, respectively, R_{ab}^{KO}, B^{KO}, and F_a^{KO} in Eqs. (5) leads to

$$T_{ab}^{R,\mathrm{KO}}(\boldsymbol{k}) = 0, \quad T^{B,\mathrm{KO}}(\boldsymbol{k}) = 0, \quad T_a^{F,\mathrm{KO}}(\boldsymbol{k}) = 0.$$

Therefore, the main contribution to T_{ab}^R, T^B, and T_a^F in the inertial range comes from terms that are linear in r_{ab}, b, and f_a. Keeping only those terms, we obtain linearized EDQNM transfer terms, whose full derivation is presented in Appendix A. The expressions of these linearized EDQNM transfer terms can be simplified by projecting them onto spherical harmonics and using the procedure developed in Ref. [24] and recalled in Appendix B. The transfer term harmonics are defined in a way similar to r_ℓ^{dir}, r_ℓ^{pol}, b_ℓ, and f_ℓ:

$$T_\ell^{\mathrm{dir}}(k) = \frac{2\ell+1}{2} k^2 \int T_{ab}^R(\boldsymbol{k}) P_{ab}(\hat{\boldsymbol{k}}) Y_\ell(\cos\theta) d\hat{\boldsymbol{k}}, \tag{13a}$$

$$T_\ell^{\mathrm{pol}}(k) = \frac{2(2\ell+1)}{(\ell-1)\ell(\ell+1)(\ell+2)} k^2 \int T_{ab}^R(\boldsymbol{k}) D_{ab}(\hat{\boldsymbol{k}},\hat{\boldsymbol{n}}) \ddot{Y}_\ell(\cos\theta) d\hat{\boldsymbol{k}}, \tag{13b}$$

$$T_\ell^F(k) = \frac{2\ell-1}{(\ell-1)\ell} k^2 \int T_a^F(\boldsymbol{k}) P_{a3}(\hat{\boldsymbol{k}}) \dot{Y}_{\ell-1}(\cos\theta) d\hat{\boldsymbol{k}}, \tag{13c}$$

$$T_\ell^B(k) = (2\ell+1) k^2 \int T^B(\boldsymbol{k}) Y_\ell(\cos\theta) d\hat{\boldsymbol{k}}. \tag{13d}$$

Inserting the linearized expression of T_{ab}^R, T^B, and T_a^F into the definitions of these harmonics and using the method developed in Ref. [24], we obtain that

$$T_\ell^{\mathrm{dir}}(k) = c_T \bar{\varepsilon}^{1/3} k^{2/3-\xi_\ell} \frac{1}{4} \left[L_\ell^{11}(\xi_\ell) c_\ell^{\mathrm{dir}} + L_\ell^{12}(\xi_\ell) c_\ell^{\mathrm{pol}} \right], \tag{14a}$$

$$T_\ell^{\mathrm{pol}}(k) = c_T \bar{\varepsilon}^{1/3} k^{2/3-\xi_\ell} \frac{1}{(\ell-1)\ell(\ell+1)(\ell+2)} \left[L_\ell^{21}(\xi_\ell) c_\ell^{\mathrm{dir}} + L_\ell^{22}(\xi_\ell) c_\ell^{\mathrm{pol}} \right], \tag{14b}$$

$$T_\ell^F(k) = c_T \bar{\varepsilon}^{1/3} k^{2/3-\xi_\ell^F} \frac{1}{2(\ell-1)\ell} L_\ell^F\left(\xi_\ell^F\right) c_\ell^F, \tag{14c}$$

$$T_\ell^B(k) = c_T \bar{\varepsilon}^{1/3} k^{2/3-\xi_\ell^B} \left(L_\ell^B\left(\xi_\ell^B\right) c_\ell^B + \frac{c_O \bar{\varepsilon}_B}{c_K \bar{\varepsilon}} k^{\xi_\ell^B - \xi_\ell} \left[L_\ell^{B1}(\xi_\ell) c_\ell^{\mathrm{dir}} + L_\ell^{B2}(\xi_\ell) c_\ell^{\mathrm{pol}} \right] \right), \tag{14d}$$

where $c_T = 2\sqrt{c_K}/\sqrt{3}a_0$ is a constant and the expressions for L_ℓ^{ij}, L_ℓ^F, L_ℓ^B, L_ℓ^{B1}, and L_ℓ^{B2} are given in Appendix B. We recall that c_ℓ^{dir}, c_ℓ^{pol}, c_ℓ^F, and c_ℓ^B are the prefactors of the power laws assumed in

Eq. (12) and ξ_ℓ, ξ_ℓ^F, and ξ_ℓ^B the exponents of these laws. All the quantities $L_\ell^*(\xi)$ depend only on ℓ and on the value of the exponent ξ.

It is worth noting that the velocity transfer terms $T_\ell^{\rm dir}$ and $T_\ell^{\rm pol}$ only depend on the ℓth harmonic of the velocity perturbation spectrum $\boldsymbol{r}$, through the exponent ξ_ℓ and the prefactors $c_\ell^{\rm dir}$ and $c_\ell^{\rm pol}$. Similarly, the transfer term T_ℓ^F of the concentration flux spectrum only depends on the ℓth harmonic of $\boldsymbol{f}$, through ξ_ℓ^F and c_ℓ^F. It is entirely independent of the anisotropy of the velocity and concentration spectra. By contrast, the concentration transfer term T_ℓ^B depends not only on the ℓth harmonic of the concentration perturbation spectrum b, through ξ_ℓ^B and c_ℓ^B, but also on the ℓth harmonic of the velocity spectrum, through ξ_ℓ, $c_\ell^{\rm dir}$, and $c_\ell^{\rm pol}$. Thus, T_ℓ^B has an explicit dependence on the anisotropy of the velocity spectrum.

Another point worth mentioning is the existence of a "window of locality" for the coefficients $L_\ell^{ij}(\xi)$, $L_\ell^F(\xi)$, $L_\ell^B(\xi)$, $L_\ell^{B1}(\xi)$, and $L_\ell^{B2}(\xi)$. As explained in Ref. [24], these coefficients involve integrals over the wave number k that can diverge at small k if the exponent ξ is too high. The limit exponent ensuring the convergence of these integrals is denoted by $\xi_\ell^\star$. For all the coefficients, it can be shown that $\xi_\ell^\star$ is the same as the one already determined in Ref. [24] for L_ℓ^{ij}:

$$\xi_\ell^\star = 3 \quad \text{for } \ell \leqslant 2, \quad \xi_\ell^\star = \ell - 1 \quad \text{for } \ell > 2. \tag{15}$$

Finally, we would like to emphasize the scaling of the linearized transfer terms given by Eq. (14), when the window of locality criterion is met. Unless the factors depending on the quantities $L_\ell^*(\xi)$ in Eq. (14) are equal to 0, the transfer terms of the velocity spectrum scale as $k^{2/3-\xi_\ell}$ and the transfer term of the concentration flux spectrum scales as $k^{2/3-\xi_\ell^F}$. As for the transfer term of the concentration spectrum, it scales, for large k, as either $k^{2/3-\xi_\ell^B}$ or $k^{2/3-\xi_\ell}$ depending on whether ξ_ℓ^B is larger or smaller than ξ_ℓ. This observation can be summed up as follows: For nonzero L_ℓ^* factors in Eq. (14),

$$\frac{T_\ell^{\rm dir}}{r_\ell^{\rm dir}}, \frac{T_\ell^{\rm pol}}{r_\ell^{\rm pol}}, \frac{T_\ell^F}{f_\ell} \propto c_T \bar{\varepsilon}^{1/3} k^{2/3}, \quad \frac{T_\ell^B}{b_\ell} \propto \begin{cases} c_T \bar{\varepsilon}^{1/3} k^{2/3} & \text{for } \xi_\ell^B \leqslant \xi_\ell \\ \frac{T_\ell^{(B)}}{r_\ell^{\rm pol}} \propto c_T \bar{\varepsilon}^{1/3} k^{2/3} & \text{otherwise.} \end{cases} \tag{16}$$

If these ratios (which correspond to nonlinear frequencies) depart from their $k^{2/3}$ scalings and all exponents are smaller than $\xi_\ell^\star$, then the conclusion is that the factors depending on the quantities $L_\ell^*(\xi)$ in Eq. (14) are equal to 0. In other words, it indicates that the perturbation spectra involved in the definitions of these factors behave as zero-modes.

V. ZERO-MODE PROPERTIES

In this section, we derive the scalings of the zero-modes of the velocity and concentration spectra of a USH flow modeled with the EDQNM closure (5). This derivation is based on the linearized expression (14) for the transfer term harmonics. In addition, we also put forward the existence of several proportionality relations between zero-modes. By extension, these results are assumed to also apply to a Rayleigh-Taylor flow. Note that we only discuss the zero-mode properties of harmonics of order $\ell \geqslant 2$. For $\ell = 0$, zero-modes simply exhibit a Kolmogorov-Obukhov scaling.

A. Zero-modes of the velocity spectrum

The zero-modes of the ℓth harmonic of the velocity spectrum correspond to a family of spectra $r_\ell^{\rm dir}$ and $r_\ell^{\rm pol}$ such that the nonlinear transfer terms $T_\ell^{\rm dir}$ and $T_\ell^{\rm pol}$ are null: $T_\ell^{\rm dir}(k) = T_\ell^{\rm pol}(k) = 0$. Given the expression (14) of the linearized transfer terms, this condition is achieved provided

$$L_\ell^{11}(\xi_\ell) c_\ell^{\rm dir} + L_\ell^{12}(\xi_\ell) c_\ell^{\rm pol} = 0, \quad L_\ell^{21}(\xi_\ell) c_\ell^{\rm dir} + L_\ell^{22}(\xi_\ell) c_\ell^{\rm pol} = 0.$$

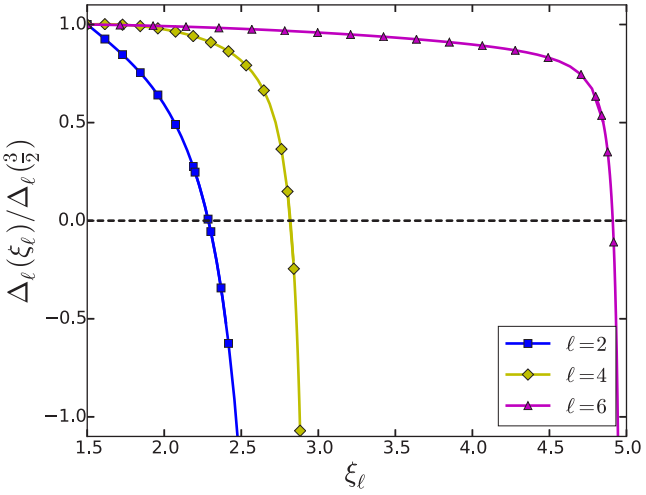

FIG. 3. Value of the determinants Δ_ℓ as a function of the anisotropy exponent ξ for $\ell = 2$, 4, and 6.

Therefore, a zero-mode of the velocity spectrum exists if

$$\Delta_\ell(\xi_\ell) = \det[\boldsymbol{L}_\ell(\xi_\ell)] = L_\ell^{11}(\xi_\ell)L_\ell^{22}(\xi_\ell) - L_\ell^{12}(\xi_\ell)L_\ell^{21}(\xi_\ell) = 0.$$

For a given ℓ, the solution to this equation determines the value of the power-law exponent ξ_ℓ that a velocity zero-mode must possess. In order to solve this equation, we apply the numerical methods proposed in Ref. [24] and recalled in Appendix C. Using this numerical method, we compute the value $\Delta_\ell(\xi_\ell)$ for $\ell = 2$, 4, and 6. The result is shown in Fig. 3. Denoting by $\xi_{\ell 0}$ the value of ξ_ℓ such that $\Delta_\ell(\xi_{\ell 0}) = 0$, we can see from Fig. 3 that

$$\xi_{20} \approx 2.286 \approx \tfrac{7}{3} - 0.047, \quad \xi_{40} \approx 2.819 \approx 3 - 0.18, \quad \xi_{60} \approx 4.911 \approx 5 - 0.09. \tag{17}$$

Thus, if a second-order-harmonic zero-mode exists, it scales approximately like $k^{-7/3}$, while a fourth-order-harmonic zero-mode scales approximately like k^{-3} and a sixth-order-harmonic one like k^{-5}. More generally, an ℓth-order-harmonic zero-mode is expected to scale like $k^{-(\ell-1)}$ for $\ell \geqslant 4$, as explained in Ref. [24]. The higher the harmonic is, the faster the zero-mode decays at large k. It must also be stressed that the relative differences between ξ_{20} and $\frac{7}{3}$ and between $\xi_{\ell 0}$ and $\ell - 1$ for $\ell \geqslant 4$ are so small that they are unlikely to be observable in most simulations. They will consequently not be commented on further in the remainder of this study.

Similar results were already obtained in Ref. [24], with slightly different exponents. This similarity was expected: As far as the velocity spectrum is concerned, the only difference between this work and [24] comes from the closure of the model frequency $\Theta_{kk'k''}$. in Ref. [24], it includes a dependence on the directional anisotropy of R_{ab}, but not in our case. This minor difference is found to have a small impact.

Beyond the results already obtained in Ref. [24], another prediction can also be made from the zero-mode analysis. Because of the relation $L_\ell^{ij} c_\ell^{(j)} = 0$, the ratio between $c_\ell^{\rm dir}$ and $c_\ell^{\rm pol}$ is fixed and so is the ratio between $r_\ell^{\rm dir}(k)$ and $r_\ell^{\rm pol}(k)$. It is given by

$$\frac{r_\ell^{\rm dir}(k)}{r_\ell^{\rm pol}(k)} = \frac{c_\ell^{\rm dir}}{c_\ell^{\rm pol}} = -\frac{L_\ell^{12}(\xi_{\ell 0})}{L_\ell^{11}(\xi_{\ell 0})} = -\frac{L_\ell^{22}(\xi_{\ell 0})}{L_\ell^{21}(\xi_{\ell 0})}.$$

The last two ratios are equal because $\Delta(\xi_{\ell 0}) = 0$. Their numerical evaluation yields

$$\frac{r_2^{\rm dir}(k)}{r_2^{\rm pol}(k)} = \frac{c_2^{\rm dir}}{c_2^{\rm pol}} \approx 7.73, \quad \frac{r_4^{\rm dir}(k)}{r_4^{\rm pol}(k)} = \frac{c_4^{\rm dir}}{c_4^{\rm pol}} \approx -6.76, \quad \frac{r_6^{\rm dir}(k)}{r_6^{\rm pol}(k)} = \frac{c_6^{\rm dir}}{c_6^{\rm pol}} \approx -16.8. \tag{18}$$

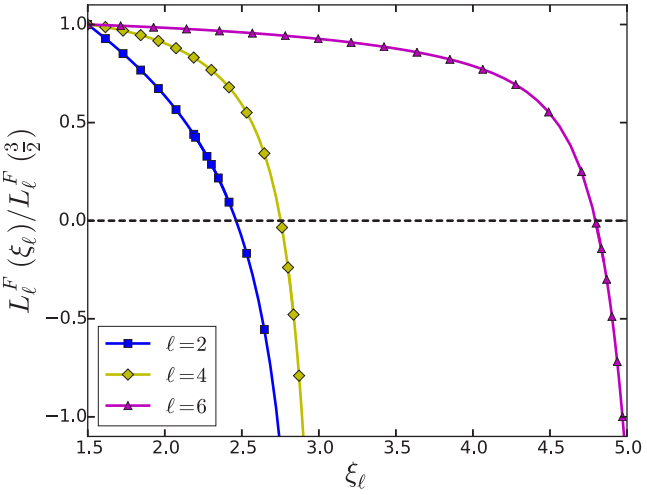

FIG. 4. Value of L_ℓ^F as a function of the anisotropy exponent ξ for $\ell = 2$, 4, and 6.

We note that, in absolute value, $r_\ell^{\rm dir}(k)$ appears to be always larger than $r_\ell^{\rm pol}(k)$. In addition, the second harmonic stands apart from the other ones because $r_2^{\rm dir}(k)$ and $r_2^{\rm pol}(k)$ share the same sign while $r_{\ell\geqslant 4}^{\rm dir}(k)$ and $r_{\ell\geqslant 4}^{\rm pol}(k)$ have opposite signs.

To conclude the discussion of the zero-modes of the velocity spectrum, we would like to discuss a limitation of the present results. As already noted, the higher the harmonic is, the faster the zero-mode decays at large k. This statement should be completed by another one: For $\ell \geqslant 4$, the higher the harmonic is, the closer its scaling exponent is to the window of locality exponent $\xi_\ell^\star$. We recall that for $\xi \geqslant \xi_\ell^\star$ the coefficients $L_\ell^{ij}(\xi)$ diverge at small k. Furthermore, when $\xi < \xi_\ell^\star$ gets closer to $\xi_\ell^\star$, small wave numbers contribute more and more to the value of the coefficients $L_\ell^{ij}(\xi)$. For the infinite inertial range considered in this theoretical study, this is not an issue. However, for a finite inertial range, this implies that scales not pertaining to the inertial range will eventually contribute significantly to $L_\ell^{ij}(\xi)$ as ξ gets closer $\xi_\ell^\star$, thus invalidating the approach. Therefore, the proximity of the zero-mode exponent $\xi_{\ell 0}$ to $\xi_\ell^\star$ for $\ell \geqslant 4$ prompts the question of which Reynolds number must be attained to verify the zero-mode features predicted in this part for a given harmonic ℓ. Equivalently, for a finite Reynolds number, there should be a harmonic $\ell_{\rm max}$ beyond which the analysis proposed here will cease to be valid. This does not mean that zero-modes should not be observed for $\ell \geqslant \ell_{\rm max}$, but only that their properties will be different from the ones predicted here for an infinite Reynolds number.

B. Zero-modes of the concentration flux spectrum

The zero-modes of the ℓth harmonic of the concentration flux spectrum correspond to a family of spectra $f_\ell(k)$ such that $T_\ell^F = 0$. Therefore, from Eq. (14), a zero-mode exists if

$$L_\ell^F\left(\xi_\ell^F\right) = 0.$$

We solve this equation using the same numerical techniques as for L_ℓ^{ij} (see Appendix C). The result, displayed in Fig. 4, shows that $L_\ell^F(\xi_\ell^F) = 0$ for $\xi_\ell^F = \xi_{\ell\ 0}^F$, with

$$\xi_{2\ 0}^F \approx 2.46 \approx \tfrac{7}{3} + 0.13, \quad \xi_{4\ 0}^F \approx 2.74 \approx 3 - 0.26, \quad \xi_{6\ 0}^F \approx 4.75 \approx 5 - 0.25. \tag{19}$$

The evolution of $\xi_{\ell\ 0}^F$ closely follows that of $\xi_{\ell 0}$. In particular, a second-order-harmonic zero-mode of $\boldsymbol{f}$ scales approximately like $k^{-7/3}$, while higher-order-harmonic zero-modes scale approximately

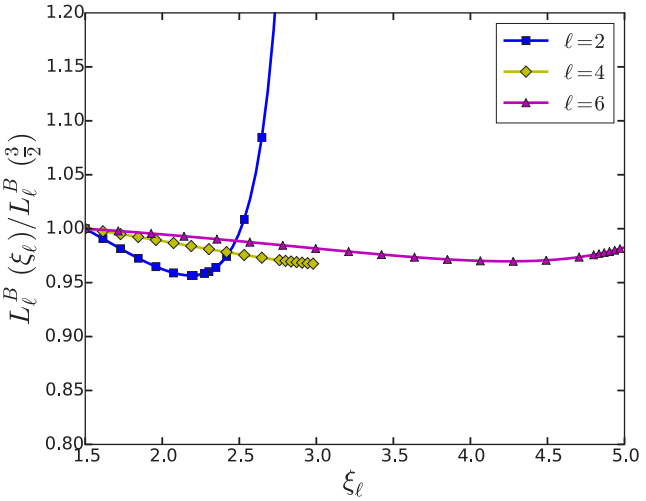

FIG. 5. Value of L_ℓ^B as a function of the anisotropy exponent ξ_ℓ for $\ell = 2$, 4, and 6.

like $k^{-(\ell-1)}$. Again, the higher the harmonic is, the faster the zero-mode decays at large k. In addition, the same limitation as for the velocity zero-modes applies to finite-Reynolds-number flows: When ℓ increases, the proximity of ${\xi_\ell^F}_0$ to $\xi_\ell^\star$ should eventually prevent observing the zero-mode predictions made here for the harmonic ℓ. A distinction must nonetheless be made between ${\xi_\ell^F}_0$ and $\xi_{\ell 0}$. The relative differences between ${\xi_2^F}_0$ and $\frac{7}{3}$ and between ${\xi_\ell^F}_0$ and $\ell - 1$ for $\ell \geqslant 4$ appear to be larger than those obtained for $\xi_{\ell 0}$ and are not necessarily negligible. In particular, the difference between ${\xi_2^F}_0$ and $\frac{7}{3}$ plays a significant role that will be detailed further in Sec. VI C.

As already noted, the zero-modes of $\boldsymbol{f}$ and $\boldsymbol{r}$ are independent from one another. The anisotropic zero-mode of $\boldsymbol{f}$ can appear whenever a mean concentration gradient exists. In particular, it can appear even when the velocity spectrum is isotropic, i.e., when $\boldsymbol{r} = 0$. This situation can be found, for instance, when a mean passive concentration gradient sustains the anisotropy of $\boldsymbol{f}$ but leaves unchanged an initially isotropic velocity spectrum.

C. Zero-modes of the concentration spectrum

As explained in Sec. IV B, the concentration transfer term T_ℓ^B displays an explicit dependence on the anisotropy of the velocity spectrum. Therefore, the zero-modes of the concentration spectrum cannot be looked for independently from those of the velocity spectrum. Here we will consider that the zero-modes of the ℓth harmonic of the concentration spectrum correspond to a family of spectra $b_\ell(k)$ such that $T_\ell^B = 0$, with the condition that r_ℓ^{dir} and r_ℓ^{pol} are zero-modes of the velocity spectrum. Then, from Eq. (14), we deduce that a zero-mode exists simultaneously for the concentration and velocity spectrum if

$$L_\ell^B\left(\xi_\ell^B\right)c_\ell^B + \frac{c_O\overline{\varepsilon}_B}{c_K\overline{\varepsilon}}k^{\xi_\ell^B-\xi_{\ell 0}}\left[L_\ell^{B1}(\xi_{\ell 0})c_\ell^{\mathrm{dir}} + L_\ell^{B2}(\xi_{\ell 0})c_\ell^{\mathrm{pol}}\right] = 0,$$

where $\xi_{\ell 0}$ is the zero-mode exponent of the velocity spectrum, as defined in Sec. V A. Figure 5 shows the evolution of $L_\ell^B(\xi_\ell^B)$ as a function of ξ_ℓ^B. It can be seen that L_ℓ^B is never equal to 0. As a result, the only possibility for a concentration zero-mode to exist along a velocity zero-mode is to have

$$\xi_\ell^B = \xi_{\ell 0}, \quad c_\ell^B = -\frac{c_O\overline{\varepsilon}_B}{c_K\overline{\varepsilon}}\left(\frac{L_\ell^{B1}(\xi_{\ell 0})}{L^B(\xi_{\ell 0})}c_\ell^{\mathrm{dir}} + \frac{L_\ell^{B2}(\xi_{\ell 0})}{L^B(\xi_{\ell 0})}c_\ell^{\mathrm{pol}}\right).$$

Consequently, the zero-mode of the scalar field is entirely determined by the anisotropy of the velocity field. This property can be made more explicit by combining the above expression of c_ℓ^B with the definitions of b_ℓ, $r_\ell^{\rm dir}$, and $r_\ell^{\rm pol}$. This yields

$$b_\ell(k) = -\frac{c_O\overline{\varepsilon}_B}{c_K\overline{\varepsilon}}\left(\frac{L_\ell^{B1}(\xi_{\ell 0})}{L^B(\xi_{\ell 0})}r_\ell^{\rm dir} + \frac{L_\ell^{B2}(\xi_{\ell 0})}{L^B(\xi_{\ell 0})}r_\ell^{\rm pol}\right). \tag{20}$$

An additional step is possible: Using the proportionality relation between $c_\ell^{\rm dir}$ and $c_\ell^{\rm pol}$ for a velocity zero-mode, we can rewrite the last equality as

$$\frac{b_\ell(k)}{r_\ell^{\rm dir}(k)} = \frac{c_\ell^B}{c_\ell^{\rm dir}} = \frac{c_O\overline{\varepsilon}_B}{c_K\overline{\varepsilon}}\Gamma_\ell^{B1}(\xi_{\ell 0})$$

or equivalently

$$\frac{b_\ell(k)}{r_\ell^{\rm pol}(k)} = \frac{c_\ell^B}{c_\ell^{\rm pol}} = \frac{c_O\overline{\varepsilon}_B}{c_K\overline{\varepsilon}}\Gamma_\ell^{B2}(\xi_{\ell 0}),$$

with

$$\Gamma_\ell^{B1}(\xi) = -\frac{L_\ell^{B1}(\xi)}{L_\ell^B(\xi)} + \frac{L_\ell^{11}(\xi)}{L_\ell^{12}(\xi)}\frac{L_\ell^{B2}(\xi)}{L_\ell^B(\xi)}, \quad \Gamma_\ell^{B2}(\xi) = \frac{L_\ell^{12}(\xi)}{L_\ell^{11}(\xi)}\frac{L_\ell^{B1}(\xi)}{L_\ell^B(\xi)} - \frac{L_\ell^{B2}(\xi)}{L_\ell^B(\xi)}.$$

Thus, only one arbitrary constant, either $c_\ell^{\rm dir}$ or $c_\ell^{\rm pol}$, sets the levels of the directional, polarization, and scalar anisotropy for the zero-modes of the velocity and concentration spectra. Computing numerically the values of $\Gamma_\ell^{B1}(\xi_{\ell 0})$ and $\Gamma_\ell^{B2}(\xi_{\ell 0})$ and knowing that $\frac{c_O\overline{\varepsilon}_B}{c_K\overline{\varepsilon}} = \frac{E_B^{\rm KO}(k)}{E^{\rm KO}(k)}$, we can write that

$$\frac{b_2(k)}{r_2^{\rm dir}(k)} \approx 1.02\frac{E_B^{\rm KO}(k)}{E^{\rm KO}(k)}, \quad \frac{b_4(k)}{r_4^{\rm dir}(k)} \approx 1.45\frac{E_B^{\rm KO}(k)}{E^{\rm KO}(k)}, \quad \frac{b_6(k)}{r_6^{\rm dir}(k)} \approx 1.61\frac{E_B^{\rm KO}(k)}{E^{\rm KO}(k)}.$$

Therefore, for zero-modes, $b_\ell(k)$ has the same sign as $r_\ell^{\rm dir}$ and their ratio is on the same order as the ratio of the main components of the potential and kinetic energy spectra in the inertial range.

VI. SUMMING EQUILIBRIUM AND ZERO-MODE SPECTRA

In the preceding section, we described the properties of the zero-modes of the EDQNM model proposed in Ref. [19] in order to improve our understanding of the inertial range anisotropy of USH and Rayleigh-Taylor turbulence. However, zero-modes are not the only components contributing to the anisotropy of the inertial range: As recalled in the Introduction and in Sec. II, another component is also required to ensure the balance between buoyancy production and nonlinear transfer terms. This additional component is referred to as the equilibrium spectrum.

The purpose of this section is to describe the equilibrium spectrum and, above all, its superposition with zero-modes.

A. Equilibrium spectrum

The equilibrium contribution was studied in Ref. [8] for Rayleigh-Taylor and implicitly for USH flows. When recasting the results of [8] with the same notation as in this work, it is predicted in Ref. [8] that the equilibrium contributions of $r_\ell^{\rm dir}$, $r_\ell^{\rm pol}$, f_ℓ, and b_ℓ are negligible for $\ell \geqslant 4$ and that

$$r_2^{\rm dir}(k)|^{\rm ES} = a^{\rm dir}k^{-3}, \quad r_2^{\rm pol}(k)|^{\rm ES} = a^{\rm pol}k^{-3}, \quad f_2(k)|^{\rm ES} = a^F k^{-7/3}, \quad b_2(k)|^{\rm ES} = a^B k^{-3}, \tag{21}$$

with $a^{\rm dir} = a^{\rm pol} = -\frac{2}{3}c_e(c_K + c_O\overline{\varepsilon}_B/\overline{\varepsilon})$, $a^F = c_F\overline{\varepsilon}^{1/3}(c_K + c_O\overline{\varepsilon}_B/\overline{\varepsilon})$, and $a^B = -\frac{4}{3}c_p(c_K + c_O\overline{\varepsilon}_B/\overline{\varepsilon})$, where the exponent ES in Eq. (21) stands for equilibrium spectrum. As explained in the Introduction, the scalings in Eq. (21) are compatible with dimensional arguments, such as those

proposed in Refs. [11,13]. The values $c_e \approx 1.2$, $c_f \approx 1.1$, and $c_p \approx 1.1$ were obtained in Ref. [8] by fitting the data of a direct simulation of a Rayleigh-Taylor flow with a moderate Reynolds number. While these values may be approximate (and were indeed reevaluated in Ref. [20]) there is one prediction, other than the scalings, that is independent of them. Namely, the ratio $r_2^{\mathrm{dir}}(k)/r_2^{\mathrm{pol}}(k)$ is predicted to be equal to 1:

$$\left.\frac{r_2^{\mathrm{dir}}(k)}{r_2^{\mathrm{pol}}(k)}\right|^{\mathrm{ES}} = 1. \tag{22}$$

From the EDQNM standpoint, the values of the constants appearing in Eq. (21) cannot be determined save for c_F. Equating buoyancy production and nonlinear transfer in the EDQNM model equation for f_2, one obtains that

$$c_F|^{\mathrm{EDQNM}} = -\frac{4}{c_T L_2^F\left(\frac{7}{3}\right)} \approx 3.8, \tag{23}$$

with $c_T = 2\sqrt{c_K}/\sqrt{3}a_0 \approx 3.8$ and $L_2^F(7/3) \approx -0.28$. Similar predictions for c_e and c_p are hindered by the necessity to account for nonuniversal parts of the spectrum. We note that the value of c_F is much higher than the one previously estimated in Ref. [8] or even in Ref. [20]. This difference will be commented on further in Sec. VI C.

Now zero-modes must be superimposed on this equilibrium solution. Using the results derived in Sec. V, we consequently obtain the following description of the inertial range anisotropic spectra, for $\ell = 2$:

$$r_2^{\mathrm{dir}}(k) = r_2^{\mathrm{dir}}(k)|^{\mathrm{ES}} + r_2^{\mathrm{dir}}(k)|^{\mathrm{ZM}} = a^{\mathrm{dir}}k^{-3} + c_2^{\mathrm{dir}}k^{-\xi_{20}}, \tag{24a}$$

$$r_2^{\mathrm{pol}}(k) = r_2^{\mathrm{pol}}(k)|^{\mathrm{ES}} + r_2^{\mathrm{pol}}(k)|^{\mathrm{ZM}} = a^{\mathrm{pol}}k^{-3} + c_2^{\mathrm{pol}}k^{-\xi_{20}}, \tag{24b}$$

$$f_2(k) = f_2(k)|^{\mathrm{ES}} + f_2(k)|^{\mathrm{ZM}} = a^F k^{-7/3} + c_2^F k^{-\xi_{2\,0}^F}, \tag{24c}$$

$$b_2(k) = b_2(k)|^{\mathrm{ES}} + b_2(k)|^{\mathrm{ZM}} = a^B k^{-3} + c_2^B k^{-\xi_{2\,0}^B}, \tag{24d}$$

where the exponents ZM and ES refer, respectively, to the zero-mode and equilibrium spectrum contributions. For $\ell \geqslant 4$, $r_\ell^{\mathrm{dir}}(k)|^{\mathrm{ES}}$, $r_\ell^{\mathrm{pol}}(k)|^{\mathrm{ES}}$, $f_\ell(k)|^{\mathrm{ES}}$, and $b_\ell(k)|^{\mathrm{ES}}$ are predicted to be negligible compared to the $\ell = 2$ harmonic, but are not precise. Hence, we will hereafter focus our discussion on the $\ell = 2$ harmonic.

in Ref. [8], zero-modes were not accounted for and the anisotropic properties of the inertial range of Rayleigh-Taylor and USH turbulence were consequently deemed to be those of the sole equilibrium contribution (21). Thus, the question we would like to address in this section is how the inclusion of zero-modes modifies the predictions originally made in Ref. [8].

B. Velocity and concentration spectra

Since $\xi_{20} = \xi_{2\,0}^B \approx 7/3 < 3$, the zero-mode contribution appearing in Eqs. (24a), (24b), and (24d) decays more slowly when k increases than the equilibrium contribution. As a result, for asymptotically small scales, the zero-mode contribution of r_2^{dir}, r_2^{pol}, and b_2 is the dominant one: Spectra with a slope close to $-7/3$ should be observed. This prediction is very different from the one originally made in Ref. [8] and that assumed that k^{-3} velocity and concentration anisotropic spectra extended down to the smallest inertial scales. This difference is not only quantitative. The k^{-3} spectrum predicted in Ref. [8] implies that anisotropy is maintained by the direct and local action of buoyancy forces. By contrast, anisotropy is shown here to be maintained by the action of nonlocal nonlinear interactions, which transfer anisotropy from scale to scale and exchange it between components. These two physical mechanisms are fundamentally different.

Another significant difference arising from the presence of zero-modes comes from the ratio between $r_2^{\rm dir}$ and $r_2^{\rm pol}$. The equilibrium solution predicted in Ref. [8] yields a ratio equal to 1 [see Eq. (22)]. By contrast, the zero-mode solution yields a ratio equal approximately to 7.73 [see Eq. (18)]. Therefore, the zero-mode value is much larger than its equilibrium counterpart:

$$\left.\frac{r_2^{\rm dir}}{r_2^{\rm pol}}\right|^{\rm ZM} \approx 7.73 > \left.\frac{r_2^{\rm dir}}{r_2^{\rm pol}}\right|^{\rm ES} = 1.$$

This difference is especially striking when considering the directional or polarization decomposition of the vertical velocity spectrum R_{33} [see Eq. (9)]. Indeed, neglecting spherical harmonics $\ell \geqslant 4$, one has $\frac{R_{33}^{\rm dir}}{R_{33}^{\rm pol}} = \frac{r_2^{\rm dir}}{6r_2^{\rm pol}}$. Therefore, while the analysis presented in Ref. [8] predicts a ratio $\frac{R_{33}^{\rm dir}}{R_{33}^{\rm pol}}$ much smaller than one, the zero-mode analysis implies that this ratio is on the order of one, with $R_{33}^{\rm dir}$ even larger than $R_{33}^{\rm pol}$.

Similarly, the ratio between b_2 and $r_2^{\rm dir}$ differs when zero-modes are accounted for. Without them, one would obtain $\frac{b_2|^{\rm ES}}{r_2^{\rm dir}(k)|^{\rm ES}} = \frac{a^B}{a^{\rm dir}} \approx 1.8$. However, with zero-modes, one should instead observe, as explained in Sec. V C, $\frac{b_2}{r_2^{\rm dir}} \approx 1.02\frac{E_B^{\rm KO}}{E^{\rm KO}}$. With $E_B^{\rm KO} \approx E^{\rm KO}$ in the inertial range, one should get a ratio $b_2/r_2^{\rm dir}$ closer to 1 when accounting for zero-modes than without them.

To conclude the discussion of these aspects, we note that k^{-3} equilibrium spectra may still be observed for $r_2^{\rm dir}$, $r_2^{\rm pol}$, and b_2, but only for an intermediate range corresponding to the largest inertial scales. The predominance of zero-modes is indeed only asymptotic. Furthermore, since $a^{\rm dir} = a^{\rm pol}$ and $c_2^{\rm dir} \approx 7.73 c_2^{\rm pol}$, we can conclude, using Eq. (24), that if such a k^{-3} range exists, then it will be observed first and foremost for the polarization harmonic $r_2^{\rm pol}$.

C. Concentration flux spectrum

In Sec. V B, we obtained that $\xi_2^F{}_0$ is larger than 7/3. As a result, Eq. (24c) indicates that the slope of the flux spectrum converges to $-7/3$ for very large k, even if a zero-mode exists. However, because $\xi_2^F{}_0 - 7/3 \approx 0.13$ is small, the convergence of the slope of the flux to $-7/3$ is very slow if a zero-mode is present. This convergence can be understood in terms of increasing wave numbers k, given an infinite Reynolds number. In particular, according to Eqs. (24) and (21), one should observe that

$$|1 - f_2^\star| \propto k^{-\delta\xi^F}, \tag{25}$$

with

$$f_2^\star = \frac{f_2(k)}{c_F\bar{\varepsilon}^{1/3}(c_K + c_O\bar{\varepsilon}_B/\bar{\varepsilon})k^{-7/3}}, \quad \delta\xi^F = \xi_2^F{}_0 - 7/3 \approx 0.13.$$

This slow convergence towards the equilibrium solution can explain why the value of c_F measured in the simulations of [8,20] is different from the one estimated from the EDQNM model.

It is also interesting to cast the convergence of the flux in terms of increasing finite Reynolds numbers. More precisely, let us define the local slope of the flux as

$$n(k) = -\frac{k}{f_2(k)}\partial_k f_2(k). \tag{26}$$

From Eq. (24c) this exponent is equal to

$$n(k) = \frac{7}{3} + \delta\xi^F \frac{\frac{c_2^F}{a^F}k^{-\delta\xi^F}}{1 + \frac{c_2^F}{a^F}k^{-\delta\xi^F}}.$$

The value of n closest to 7/3 is obtained at the end of the inertial range, i.e., for a wave number proportional to the inverse of the Kolmogorov scale $k_\eta \ell_T = \mathrm{Re}_\lambda^{3/2}$, where ℓ_T is the integral scale of turbulence and Re_λ is the Reynolds number based on the Taylor microscale. Then one obtains that

$$n(k_\eta) = \frac{7}{3} + \delta\xi^F \frac{x^F \mathrm{Re}_\lambda^{-3\delta\xi^F/2}}{1 + x^F \mathrm{Re}_\lambda^{-3\delta\xi^F/2}},$$

where $x^F = \ell^{-\delta\xi^F} \frac{c_2^F}{a^F}$ is a constant assuming that the zero-mode and equilibrium components of the flux obey a self-similar scaling. Therefore, with $\delta\xi^F \approx 0.13$, one obtains that for large Reynolds numbers

$$|n(k_\eta) - 7/3| \propto \mathrm{Re}_\lambda^{-0.2}.$$

As explained in Sec. V B, this prediction is independent of the Rayleigh-Taylor context and of the anisotropy of the velocity field. It applies whenever a mean scalar gradient exists and in particular it applies to a concentration flux spectrum in isotropic turbulence with a uniform gradient. This situation was treated in Ref. [28], where $7/3 - n(k_\eta)$ was found to decay as $\mathrm{Re}_\lambda^{-0.54}$. This value is much higher than the one obtained here and would correspond to an exponent ${\xi_2^F}_0 = 2.69$ instead of 2.46. Nonetheless, we note that the exponent proposed by [28] is a fit that matches well their low-Reynolds-number data but not necessarily their higher-Reynolds-number data. For $\mathrm{Re}_\lambda > 10^4$, their data appear to be actually better fitted with a smaller exponent. This result already suggests that the concentration flux zero-mode will possess the characteristics predicted in this work only for very high Reynolds numbers. For lower Reynolds numbers, zero-modes can still exist and play a role, but their properties will be different from those predicted here in the infinite-Reynolds-number case, with an infinite inertial range.

VII. VALIDATION

In order to validate the results derived in Secs. V and VI, we perform two sets of simulations. First, we perform high-Reynolds-number ($\mathrm{Re} \sim 10^7$) EDQNM simulations of USH turbulence and assess the predictions made in Secs. V and VI. Second, we carry out the same analysis, this time based on the large-eddy simulation of a Rayleigh-Taylor flow performed in Ref. [17]. Note that a comparison between EDQNM simulations and a 2048^3 USH direct simulation is described in Ref. [21], with details given on the anisotropic properties of the turbulent spectra.

A. High-Reynolds-number EDQNM simulations of a USH flow

1. *Initial conditions and numerical scheme*

The EDQNM simulations discussed hereafter are similar to those already performed in Refs. [19–21]. At initial time, the turbulent spectra are chosen to be isotropic. As a result, the concentration flux is null and we only need to specify the kinetic energy spectrum $E(k,t)$ and the concentration modulus spectrum $E_B(k,t)$ defined as

$$E(k,t) = \frac{k^2}{2} \int R_{jj}(\boldsymbol{k}) d\hat{\boldsymbol{k}}, \quad E_B(k,t) = k^2 \int B(\boldsymbol{k}) d\hat{\boldsymbol{k}}.$$

At $t = 0$, these spectra are chosen equal to

$$E(k,t=0) = A_s h(k), \quad E_B(k,t=0) = B_s h(k),$$

where

$$h(k) = \left(\frac{k}{k_{\mathrm{peak}}}\right)^s \exp\left[-\frac{s}{2}\left(\frac{k}{k_{\mathrm{peak}}}\right)^2\right],$$

with k_{peak} the most energetic wave number, s the slope of the infrared spectrum, and A_s and B_s normalization constants setting the initial values of the kinetic energy $\mathcal{K}$ and concentration variance $\mathcal{B}$:

$$\mathcal{K}(t) = \int_0^\infty E(k,t)dk, \quad \mathcal{B}(t) = \int_0^\infty E_B(k,t)dk.$$

The values of A_s and B_s are set so that $\mathcal{K}(t=0) = \mathcal{B}(t=0) = 0.25$. The initial values of s and k_{peak} are $s = 2$ and $k_{\text{peak}} \approx 44$. The only unspecified remaining parameter is the value of the viscosity ν, which is set to $\nu = 1.25 \times 10^{-4}$.

With these parameters, we solve the EDQNM model equations (4) on a domain spanning six decades, from $k_{\min} = 10^{-2}$ to $k_{\max} = 10^4$. The numerical integration is performed with almost the same method as the one detailed in Refs. [19,41]. We only introduce a small modification consisting in the addition of a local time stepping, ensuring that the nonlinear time scale is well resolved. This modification proves to be decisive for exploring large-Reynolds-number flows. Indeed, without it, the time step Δt of the EDQNM solver proposed in Refs. [19,41] is controlled by realizability constraints and is empirically found to scale as $\Delta t \propto \tau_\eta \text{Re}^{-1/2}$, with τ_η the Kolmogorov time scale. With the proposed modification, the scaling $\Delta t \propto \tau_\eta$ is achieved. As a result, the cost for reaching a Reynolds number of 10^6 in USH turbulence is divided by a factor 10^3 with our local time-stepping scheme.

Note that the cost of running an EDQNM simulation is not innocuous. Indeed, the cost of one EDQNM time step is proportional to $(N_k N_\theta)^2 N_\lambda$, with N_k, N_θ, and N_λ the numbers of points discretizing, respectively, the wave numbers, the cosines of the angle θ, and the directions of the triads appearing in the integrands of the system of equations (4). Doubling the resolution in each direction leads to multiplying the cost of one time step by 32. In practice, while the USH simulations detailed in Ref. [20] with $N_k = 128$, $N_\theta = 20$, and $N_\lambda = 20$ take about 1 h on 128 processors to reach a Reynolds number of 10^6, simulations with $N_k = 1024$, $N_\theta = 80$, and $N_\lambda = 20$, such as those detailed in this work, take about 48 h on 4096 processors to reach the same Reynolds number and about a week to reach a Reynolds number of 10^7. The factor 10^3 gained by modifying the numerical scheme is of course crucial for allowing these simulations to run in an acceptable time.

The reason we need higher resolutions than in Ref. [20] is because the anisotropic quantities discussed in Secs. V and VI appear to converge slowly with the increase of N_k and N_θ. For instance, in Ref. [20], the polarization spectrum R_{33}^{pol}, defined in Eq. (9), was found to be always larger than its directional counterpart R_{33}^{dir}. However, when increasing N_k and N_θ, the ratio $R_{33}^{\text{dir}}/R_{33}^{\text{pol}}$ in the inertial range increases until it becomes larger than one. By contrast, the value of N_λ did not appear to have any effect on this quantity or on any other aspect of the simulation. Figure 6 shows how the ratio $R_{33}^{\text{dir}}/R_{33}^{\text{pol}}$ evolves with N_k and N_θ. It can be seen that a converged value, with a relative variation of less than 1%, is obtained for $N_k \geqslant 1024$ and $N_\theta \geqslant 60$. The simulation discussed hereafter is performed with $N_k = 1024$, $N_\theta = 80$, and $N_\lambda = 20$.

2. *One-point statistics*

Detailed commentaries about the evolutions of the one-point statistics of USH turbulence can be found in Refs. [16,18–21]. Here we recall that, after a transient, the second-order correlations of velocity and concentration reach an exponential self-similar regime. Using the arguments developed in Ref. [17] and concerning the permanence of large eddies, it can be shown that these correlations evolve proportionally to $\exp(\frac{4}{s+3}t)$.

Figure 7 shows the evolution of the kinetic energy $\mathcal{K}$, of the concentration variance $\mathcal{B}$, and of the Reynolds number defined as

$$\text{Re} = \frac{\mathcal{K}^2}{\bar{\varepsilon}\nu},$$

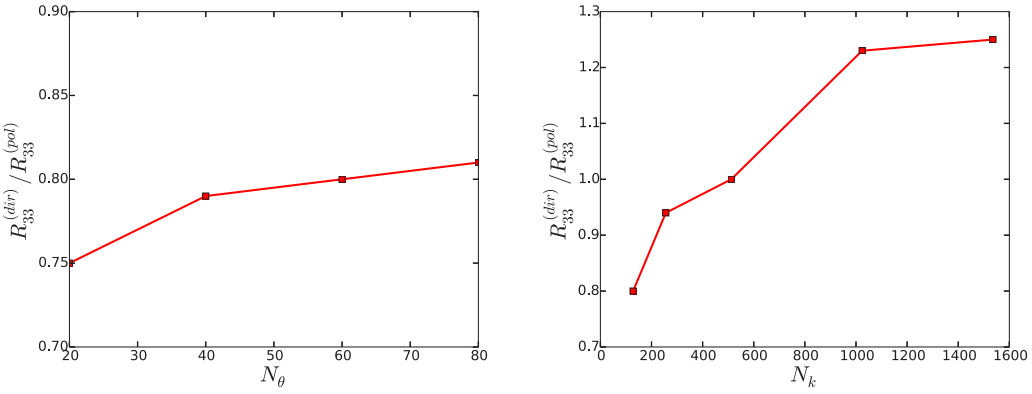

FIG. 6. Evolution of the maximum of the ratio $R_{33}^{\rm dir}/R_{33}^{\rm pol}$ in the inertial range (a) as a function of N_θ for $N_k = 128$ and (b) as a function of N_k for $N_\theta = 60$.

with $\overline{\varepsilon} = 2\nu \int_0^\infty k^2 E(k,t)dk$. The self-similar regime can be observed after $t \approx 3$. The predicted exponential evolutions of $\mathcal{K}$, $\mathcal{B}$, and Re are then well verified: For $t \gtrsim 3$, $\mathcal{K}$, $\mathcal{B}$, and Re $\propto e^{[4/(s+3)]t}$.

The flow being nonstationary, one may wonder how nonstationarity affects the properties of inertial scales. While not detailed here, it can be shown that for harmonics $\ell \geqslant 2$ the unsteady terms of $r_\ell^{\rm dir}$, $r_\ell^{\rm pol}$, f_ℓ, and b_ℓ are small compared to their respective nonlinear transfer and buoyancy terms. As a result, they do not modify the behavior of the inertial range, i.e., they do not affect the existence of an equilibrium spectrum or the properties of zero-modes.

3. Zeroth-order harmonic: Kinetic energy and concentration modulus spectra

Once the Reynolds number becomes high enough, the kinetic energy and concentration modulus spectra $E(k,t)$ and $E_B(k,t)$ develop an inertial range with a Kolmogorov-Obukhov scaling, as expressed by Eq. (7). To assess the validity of this scaling, we introduce normalized spectra

$$E^*(k) = \frac{E(k)}{\overline{\varepsilon}^{2/3}k^{-5/3}}, \quad E_B^*(k) = \frac{E_B(k)}{\overline{\varepsilon}_B\overline{\varepsilon}^{-1/3}k^{-5/3}}.$$

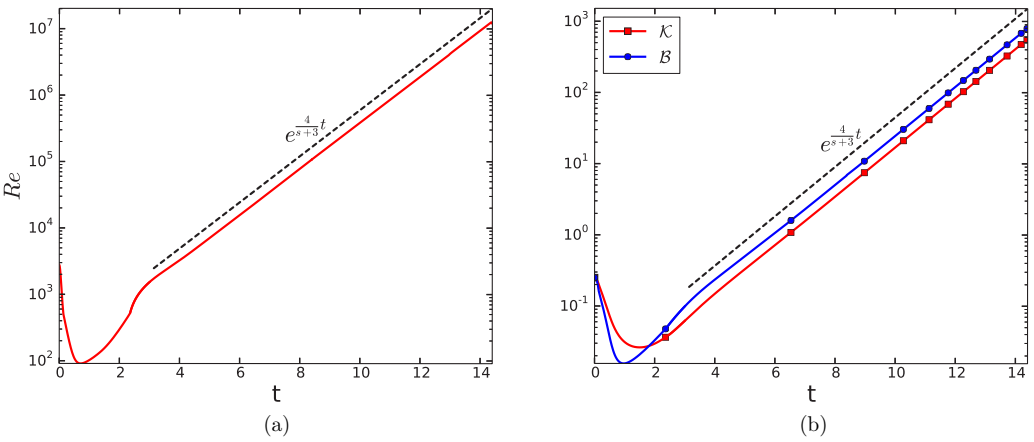

FIG. 7. Evolution of several one-point statistics for (a) Reynolds number Re and (b) kinetic energy and concentration variance.

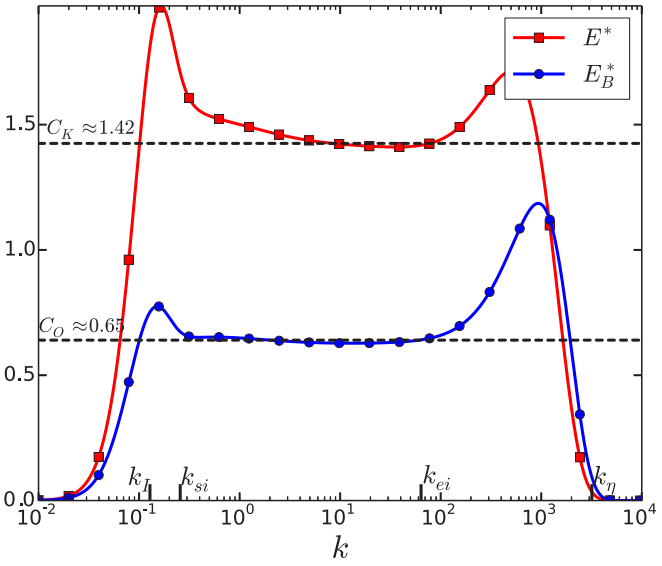

FIG. 8. Normalized spectra $E^*(k)$ and $E_B^*(k)$ for Re $\approx 10^7$.

These two normalized spectra are displayed in Fig. 8 at the final time of the simulation for a Reynolds number Re $\approx 10^7$. They both exhibit a plateau indicating the presence of an inertial range with a Kolmogorov-Obukhov scaling. The heights of the plateau for E^* and E_B^* give the following values of the Kolmogorov and Obukhov constants:

$$C_K \approx 1.42, \quad C_O \approx 0.65.$$

The two plateaus extend for about two decades, from k_{si} to k_{ei}, where

$$k_{si} \approx 2k_I, \quad k_{ei} \approx 0.02k_\eta, \tag{27}$$

with

$$k_I = \frac{\int E(k)dk}{\int \frac{E(k)}{k}dk}, \quad k_\eta = \overline{\varepsilon}^{1/4}\nu^{-3/4}.$$

The wave number k_I is the inverse of an autocorrelation length characteristic of large scales, while k_η is the inverse of the Kolmogorov dissipation scale. These properties were already described, with additional details, in Refs. [19–21]. In the remainder of this section, we will assume that the inertial range starts at k_{si} and ends at k_{ei}:

$$\text{INERTIAL RANGE} \equiv [k_{si}, k_{ei}].$$

Note that the spectral bump occurring beyond k_{ei} is not included into the inertial range. Its existence is generally attributed to the so-called bottleneck phenomenon [42].

4. Velocity spectrum

We now turn our attention to the anisotropic properties of the flow. First, we consider $r_2^{\text{dir}}(k)$ and $r_2^{\text{pol}}(k)$, the second-order harmonics of the velocity spectrum defined by Eq. (10). Figure 9(a) compares these two spectra along with the isotropic component $E(k)$. We observe that $r_2^{\text{dir}}(k)$ and $r_2^{\text{pol}}(k)$ decay faster than $E(k)$ in the inertial range and that their absolute values eventually become much smaller than $E(k)$:

$$|r_2^{\text{dir}}(k)|, |r_2^{\text{pol}}(k)| \ll E(k).$$

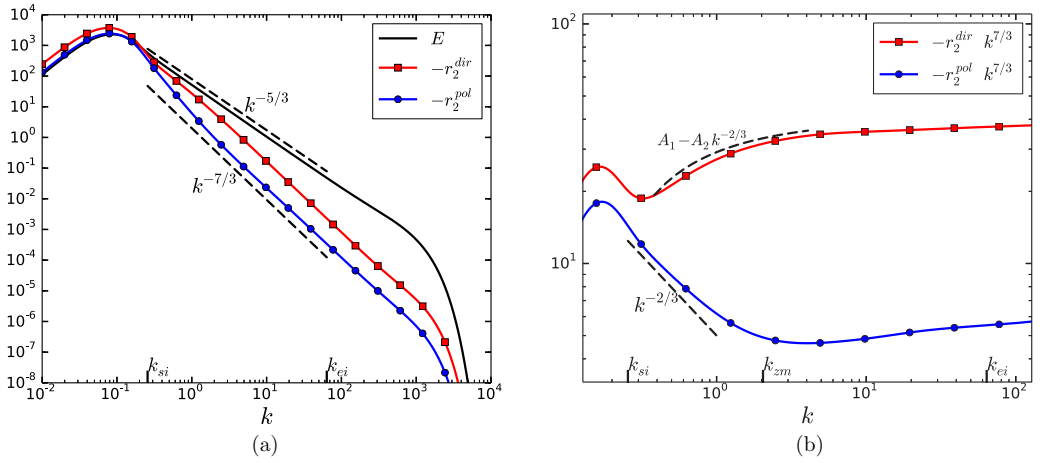

FIG. 9. Second-order harmonics of the velocity spectrum. (a) Comparison between $r_0^{\rm dir}$, $r_2^{\rm dir}$, and $r_2^{\rm pol}$. (b) Compensated spectra $r_2^{\rm dir}k^{7/3}$ and $r_2^{\rm pol}k^{7/3}$.

This observation agrees with the central hypothesis leading to the linearization of the EDQNM model in Sec. IV and the derivation of zero-modes.

We also observe in Fig. 9(a) that $r_2^{\rm dir}(k)$ and $r_2^{\rm pol}(k)$ exhibit an inertial slope close to $-7/3$. To assess this property more precisely, we plot in Fig. 9(b) the compensated spectra $r_2^{\rm dir}k^{7/3}$ and $r_2^{\rm pol}k^{7/3}$, zooming in on the previously identified inertial interval $[k_{si},k_{ei}]$. The inertial range appears to be divided into two parts roughly delimited by a wave number k_{zm} with an observed value of $k_{zm} \approx 8k_{si}$.

For $k_{si} \lesssim k \lesssim k_{zm}$, $r_2^{\rm pol}(k)k^{7/3}$ displays a variation compatible with a $k^{-2/3}$ scaling, while $r_2^{\rm dir}(k)k^{7/3}$ exhibits a variation that can be fitted with a function of the form $A_1 - A_2k^{-2/3}$. For $k_{zm} \lesssim k \lesssim k_{ei}$, both $r_2^{\rm pol}(k)k^{7/3}$ and $r_2^{\rm pol}(k)k^{7/3}$ remain approximately constant. Therefore, we have approximately

$$r_2^{\rm dir}(k) \propto A_1k^{-7/3} - A_2k^{-3}, \quad r_2^{\rm pol}(k) \propto k^{-3} \quad \text{for } k_{si} \lesssim k \lesssim k_{zm},$$
$$r_2^{\rm dir}(k) \propto k^{-7/3}, \quad r_2^{\rm pol}(k) \propto k^{-7/3} \quad \text{for } k_{zm} \lesssim k \lesssim k_{ei}.$$

These observations are coherent with the predictions made in Sec. VI. Indeed, Eqs. (21) predict that $r_2^{\rm dir}$ and $r_2^{\rm pol}$ are the sum of two contributions, an equilibrium contribution scaling like k^{-3} and a zero-mode contribution scaling approximately like $k^{-7/3}$. This description allows for the possibility of observing a k^{-3} spectrum for the largest scales of the inertial range and an approximate $k^{-7/3}$ for its smallest scales. Whether a k^{-3} inertial subrange is actually seen or not depends on the relative intensity of the two components, which is not predicted by the theory. For $r_2^{\rm pol}$, it seems that this relative intensity is sufficient for the occurrence of an approximate k^{-3} component, while for $r_2^{\rm dir}$ it is not. This difference in behavior of $r_2^{\rm pol}$ and $r_2^{\rm dir}$ is also in agreement with the discussion of Sec. VI B.

Thus, the observed scalings of $r_2^{\rm dir}$ and $r_2^{\rm pol}$ are consistent with the existence of velocity zero-modes in the inertial range $[k_{si},k_{ei}]$ and with their predominance in the subinterval $[k_{zm},k_{ei}]$. Then, if this is indeed the case, if zero-modes are indeed prevalent in $[k_{zm},k_{ei}]$, one should obtain a ratio $r_2^{\rm dir}/r_2^{\rm pol} \approx 7.73$, as predicted by the zero-mode theory.

This ratio is displayed in Fig. 10(a). It can be seen that for $k \gtrsim k_{zm}$, the value of $r_2^{\rm dir}/r_2^{\rm pol}$ is close to the expected zero-mode value. We also note that most of the k^{-3} subinterval $[k_{si},k_{zm}]$ corresponds to a transition from a value $r_2^{\rm dir}/r_2^{\rm pol} \approx 1$ to $r_2^{\rm dir}/r_2^{\rm pol} \approx 7.7$. The value $r_2^{\rm dir}/r_2^{\rm pol} \approx 1$ is the one predicted by the equilibrium solution, as explained in Sec. VI B. In Sec. VI B, it was also noted that such high

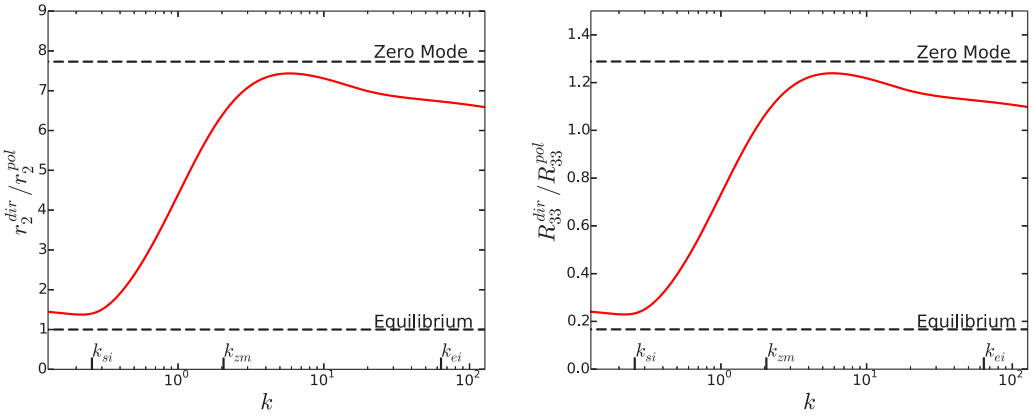

FIG. 10. Ratios of anisotropic components of the velocity spectrum: (a) ratio $r_2^{\rm dir}/r_2^{\rm pol}$ and (b) ratio $R_{33}^{\rm pol}/R_{33}^{\rm dir}$.

values of the ratio $r_2^{\rm dir}/r_2^{\rm pol}$ would correspond to a directional anisotropy larger than the poloidal one. This is indeed the case, as can be seen in Fig. 10(b), which displays the ratio $R_{33}^{\rm dir}/R_{33}^{\rm pol}$.

As a last check of the presence of zero-modes, we plot the nonlinear frequencies $|T_2^{\rm dir}/r_2^{\rm dir}|$ and $|T_2^{\rm pol}/r_2^{\rm pol}|$ in Fig. 11. As explained in Sec. IV B, these frequencies should evolve as $k^{2/3}$ save for the presence of zero-modes. As can be seen in Fig. 11, the nonlinear frequencies exhibit a $k^{2/3}$ dependence only in the subinterval $[k_{si},k_{zm}]$. For $k \gtrsim k_{zm}$, they appear to be almost constant, agreeing with the existence of zero-modes. Therefore, the scalings of $r_2^{\rm dir}$ and $r_2^{\rm pol}$, their ratios, and the nonlinear frequencies $|T_2^{\rm dir}/r_2^{\rm dir}|$ and $|T_2^{\rm pol}/r_2^{\rm pol}|$ are all coherent with the presence of zero-modes for the second harmonic of the velocity spectrum.

This presence has been discussed so far for a Reynolds number $\mathrm{Re} = 1.2 \times 10^7$. One may wonder if it is also observed for smaller Reynolds numbers. To answer this question, we plot in Fig. 12(a) the compensated spectra $r_2^{\rm dir}k^{7/3}$ and $r_2^{\rm pol}k^{7/3}$, nondimensionalized by their value at $k = k_I$, as a

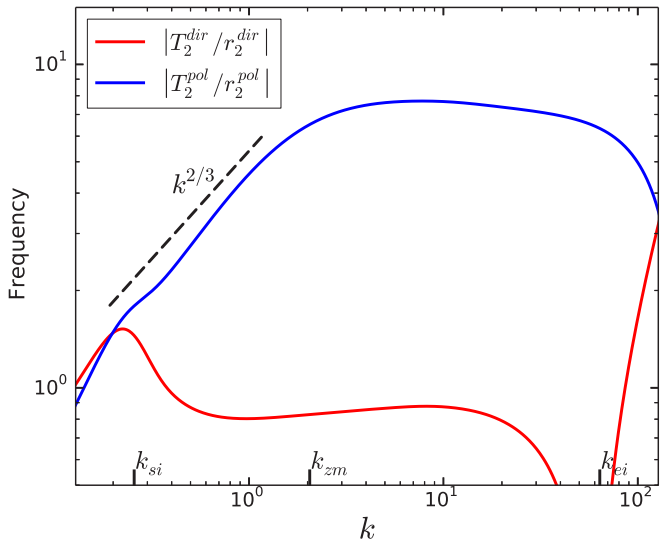

FIG. 11. Nonlinear frequencies $|T_2^{\rm dir}/r_2^{\rm dir}|$ and $|T_2^{\rm pol}/r_2^{\rm pol}|$.

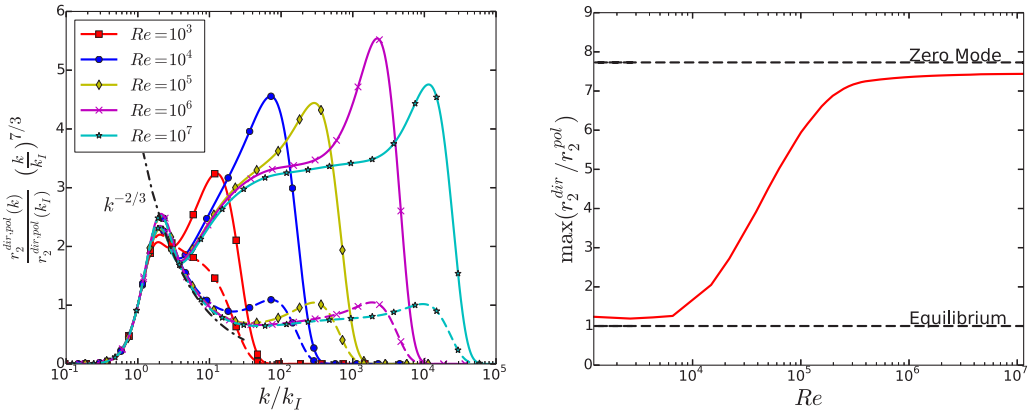

FIG. 12. (a) Compensated spectra $r_2^{\rm dir}(k)k^{7/3}/r_2^{\rm dir}(k_I)k_I^{7/3}$ (solid lines) and $r_2^{\rm pol}(k)k^{7/3}/r_2^{\rm pol}(k_I)k_I^{7/3}$ (dashed lines) at different Reynolds numbers. (b) Maximum value of $r_2^{\rm dir}(k)/r_2^{\rm pol}(k)$ in the inertial range as a function of the Reynolds number.

function of k/k_I, for different Reynolds numbers. We recall that k_I is defined by Eq. (27) and roughly corresponds to the peak of the energy spectrum. It can be seen that plateaus indicative of the $k^{-7/3}$ zero-mode scaling start to appear for Re $\gtrsim 10^5$. We also note that for $10^4 \lesssim$ Re $\lesssim 10^5$, the polarization harmonic $r_2^{\rm pol}$ mostly scales as k^{-3}, but that the directional one $r_2^{\rm dir}$ already differs from this scaling because of the presence of a zero-mode. Hence, even if only partially, the effect of zero-modes can be observed for Re $\gtrsim 10^4$. Another indication of Reynolds convergence is shown in Fig. 12(b). This figure displays the maximum value of the ratio $r_2^{\rm dir}/r_2^{\rm pol}$ in the inertial range. It can be observed that this value converges towards the zero-mode prediction of 7.73 for Re $\gtrsim 10^5$. It can also be seen that it departs significantly from 1, the value corresponding to equilibrium spectra, for Re $\gtrsim 10^4$. These two observations confirm the conclusions already drawn from Fig. 12(a), i.e., that observing the full features of velocity zero-modes requires Reynolds numbers larger than 10^5, but that the presence of zero-modes start influencing the velocity spectrum for Re $\gtrsim 10^4$.

To conclude the description of the anisotropy of the velocity spectrum, we display in Fig. 13 some information about harmonics of order 4 and 6. More precisely, we show the ratios $r_\ell^{\rm dir}/r_2^{\rm dir}$

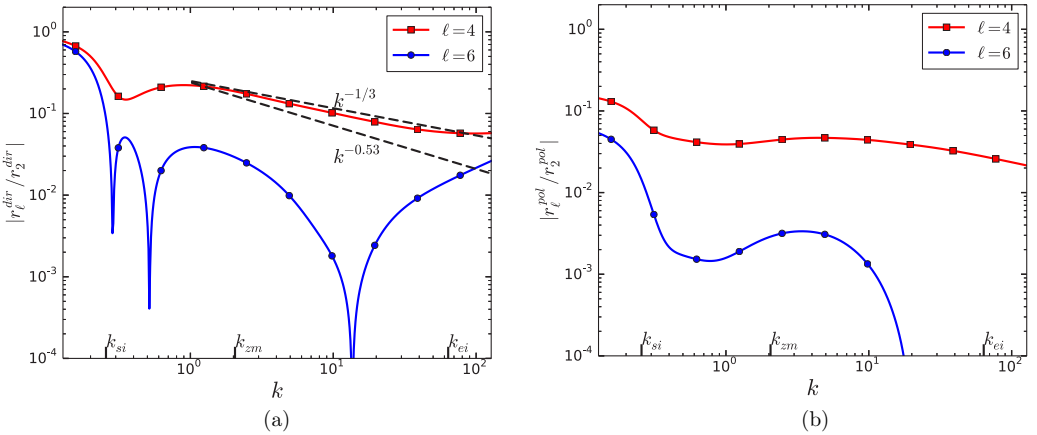

FIG. 13. Ratios (a) $|r_\ell^{\rm dir}/r_2^{\rm dir}|$ and (b) $|r_\ell^{\rm pol}/r_2^{\rm pol}|$ for $\ell = 4$ and 6.

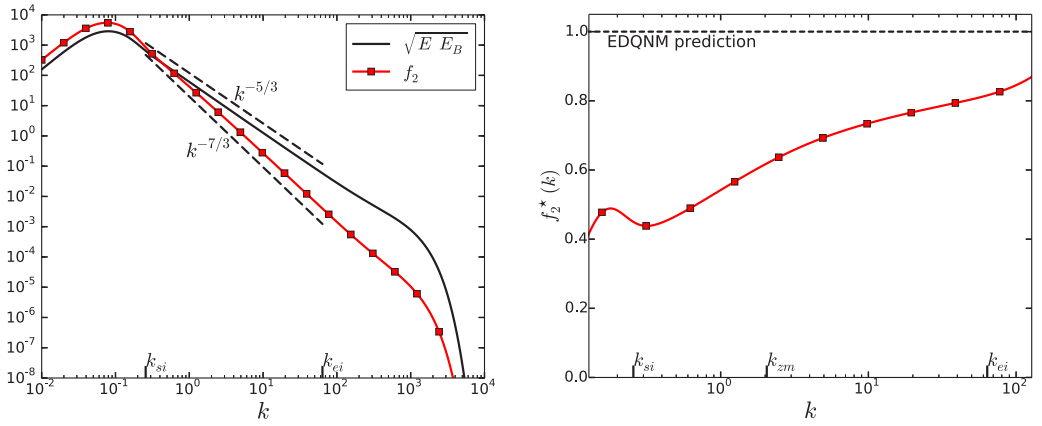

FIG. 14. Second-order harmonic of the concentration flux $f_2(k)$ (a) without renormalization and (b) with the $k^{7/3}$ renormalization defined by Eq. (25): $f_2^\star = \frac{f_2}{c_F \bar{\varepsilon}^{1/3}(c_K + c_O \bar{\varepsilon}_B/\bar{\varepsilon}) k^{-7/3}}$.

and $r_\ell^{\rm pol}/r_2^{\rm pol}$ for $\ell = 4$ and 6. The main observation is that these ratios are small compared to one in the inertial range. This is consistent with the predominance of the second-order harmonic predicted by the zero-mode analysis. However, the scalings of $r_\ell^{\rm dir}$ and $r_\ell^{\rm pol}$ for $\ell = 4{,}6$ do not seem to obey the predictions made in Sec. V A. For $\ell = 4$, $r_4^{\rm dir}/r_2^{\rm dir}$ and $r_4^{\rm pol}/r_2^{\rm pol}$ should decay with an exponent $\xi_{40} - \xi_{20} \approx 0.53$, but the decay of $r_4^{\rm dir}/r_2^{\rm dir}$ is closer to 1/3, while $r_4^{\rm pol}/r_2^{\rm pol}$ appears to be constant. As for $\ell = 6$, $r_6^{\rm dir}$ exhibit numerous changes of sign in the inertial range, which prevent any measure of an inertial slope, while $r_6^{\rm pol}$ does not display any clear power-law scaling. Thus, while evidence of zero-modes can be identified for the second-order harmonics $r_2^{\rm dir}$ and $r_2^{\rm pol}$, this is not the case for higher harmonics $r_\ell^{\rm dir}$ and $r_\ell^{\rm pol}$ with $\ell = 4$ and 6. This may come from the action of buoyancy forces or from the unaccounted nonlocal effect of distant interactions. In particular, as explained in Sec. V A, high-order harmonics can only exhibit the features predicted in this work for very high Reynolds numbers because the contribution from distant interactions becomes higher as ℓ increases.

5. *Concentration flux spectrum*

Figure 14(a) shows $f_2(k)$, the second harmonic of the concentration flux spectrum, at the final time of the simulation for a Reynolds number $\mathrm{Re} \approx 10^7$. As expected from Eq. (24c) and as already observed numerous times [21,28], the inertial slope of the flux spectrum is close to $-7/3$. Figure 14(b) displays a close-up in the inertial range of the renormalized spectrum $f_2^\star(k)$ defined by Eq. (25), with constants set to $c_F = 3.8$, $c_K = 1.42$, and $c_0 = 0.65$, in agreement with the EDQNM model predictions. A non-negligible variation of $f_2^\star$ can be seen between the two wave numbers k_{si} and k_{ei}, which have been previously identified as the limits of the inertial range. Such a variation is compatible with the existence of a zero-mode of the concentration flux in the inertial range. Indeed, the proximity of the zero-mode exponent $\xi_2^F{}_0$ to 7/3 implies a slow convergence of the slope of the flux to $-7/3$. This slow convergence can also explain why $f_2^\star$ is not equal to 1 but only to 0.8 at the end of the inertial range and accordingly why the constant c_F evaluated in simulations is systematically smaller than the EDQNM prediction of $c_F = 3.8$.

A more direct verification of the presence of a zero-mode can be performed by plotting $|1 - f_2^\star|$. According to Eq. (25), this quantity should decay proportionally to $k^{-0.13}$. In Fig. 15, it can be seen that, at the end of the inertial range, $|1 - f_2^\star|$ decays with an exponent close to 0.17, i.e., only 30% higher than the predicted one.

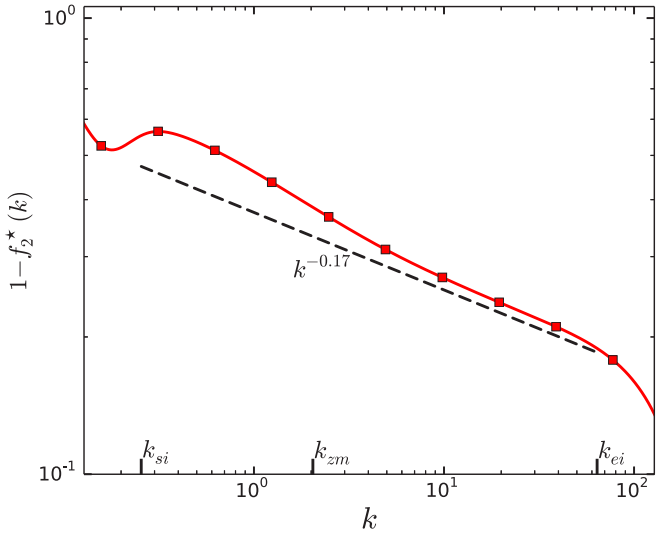

FIG. 15. Difference between $f_2^\star$ and its expected asymptotic value 1.

In addition, the slow convergence due to the presence of a zero-mode was recast in terms of Reynolds numbers in Sec. VI C: The difference between the local slope $n(k)$ at the end of the inertial range and $7/3$ is predicted to evolve as $\mathrm{Re}_\lambda^{-0.2}$ for high Reynolds numbers. In order to verify this prediction, we compute $n(k)$ according to Eq. (26) with a central finite-difference approximation of the gradient. This computation is done at the end of the inertial range, at $k = k_{ei}/2$. Then we plot in Fig. 16 the difference $7/3 - n(k_{ei}/2)$ as a function of the Taylor Reynolds number Re_λ defined as

$$\mathrm{Re}_\lambda = \sqrt{\frac{20}{3}\frac{k^2}{\bar{\varepsilon}\nu}}.$$

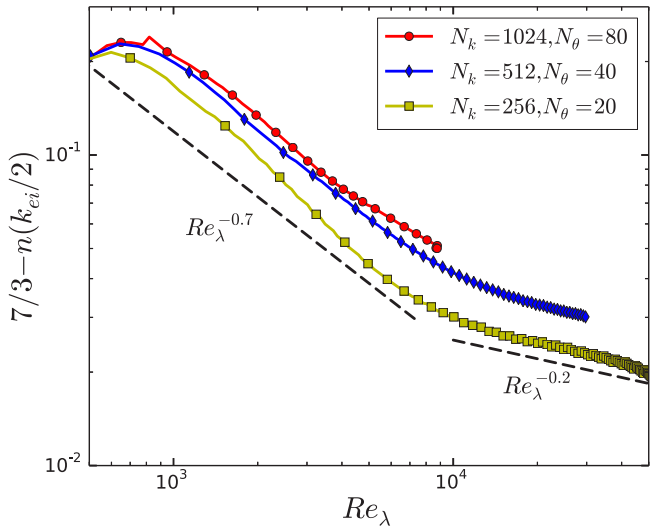

FIG. 16. Difference between $7/3$ and the inertial slope of the concentration flux measured at $k = k_{ei}/2$ as a function of Re_λ.

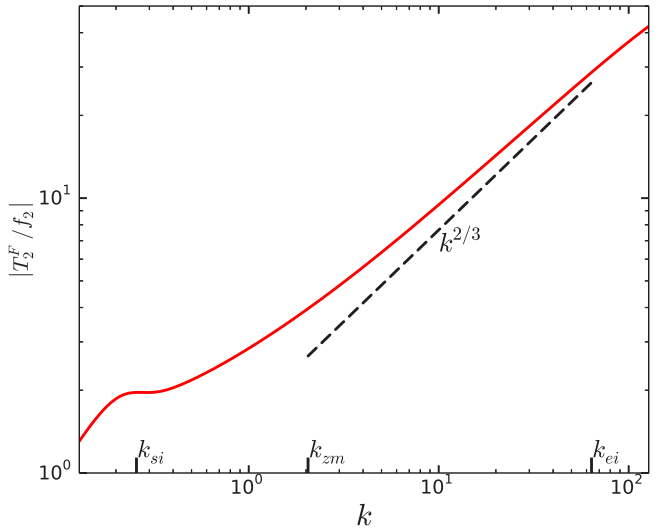

FIG. 17. Nonlinear frequency $|T_2^F/f_2|$.

It can be seen that $7/3 - n(k_{ei}/2)$ decreases approximately like $\mathrm{Re}_\lambda^{-0.7}$, i.e., with an exponent 3.5 times larger than predicted. However, for the highest Reynolds numbers, close to $\mathrm{Re}_\lambda = 5000$, a departure from this approximate power law is observed. With a resolution of $N_k = 1024$, $N_\theta = 80$, and $N_\lambda = 20$, the CPU cost of the simulation was too high to go beyond $\mathrm{Re}_\lambda = 5000$. Therefore, in order to explore the regime $\mathrm{Re}_\lambda > 10^4$, we performed two additional simulations with lower resolutions $N_k = 512$, $N_\theta = 40$, and $N_\lambda = 20$ and $N_k = 256$, $N_\theta = 20$, and $N_\lambda = 20$.

As can be seen in Fig. 16, both high- and low-resolution simulations display similar features for $\mathrm{Re}_\lambda < 5000$, as far as the decay exponent for $7/3 - n(k_{ei}/2)$ is concerned. In addition, for $\mathrm{Re}_\lambda > 10^4$, the two lower-resolution simulations exhibit a change of decay exponent for $7/3 - n(k_{ei}/2)$. This exponent becomes close to 0.2, i.e., to the value predicted by the zero-mode analysis. Note that we performed additional verifications, changing the location where the slope of f_2 is measured over one decade, from $k = 0.1k_{ei}$ to $k = k_{ei}$. The two zones of decay of $7/3 - n(k)$ delimited by $\mathrm{Re}_\lambda = 10^4$ were still observed. In addition, the decay exponent of the highest-Reynolds-number zone varied from approximately 0.24 to 0.16: It still remained close to the zero-mode prediction.

As a last check of the presence of a zero-mode, we plot in Fig. 17 the nonlinear frequency $|T_2^F/f_2|$. According to Eq. (16), $|T_2^F/f_2|$ should increase as $k^{2/3}$ save for the presence of zero-modes. It can be seen in Fig. 17 that the tendency of $|T_2^F/f_2|$ towards $k^{2/3}$ is only achieved at the end of the inertial range. For the largest and intermediate scales of this range, the variation of $|T_2^F/f_2|$ is different from $k^{2/3}$. These observations are in agreement with the presence of a zero-mode that becomes subdominant as k increases.

As a whole, the proximity of the concentration flux zero-mode exponent with its equilibrium counterpart makes the identification of this mode difficult. Still, the compensated spectrum $f_2^\star$, the dependence of the inertial slope $n(k)$ on the Reynolds number, and the nonlinear frequency $|T_2^F/f_2|$ give several indications suggesting that this mode may indeed be present.

Concerning higher-order harmonics of the concentration flux, it can be seen in Fig. 18 that the harmonics of order $\ell = 4$ and 6 are much smaller than the harmonic of order $\ell = 2$. In addition, $|f_4/f_2|$ appears to decay in the inertial zone with an exponent close to the zero-mode prediction $\xi^F_{4\,0} - \xi^F_{2\,0} \approx 0.28$. As for $|f_6/f_2|$, sign changes prevent observing a clear power-law decay. The first part of the inertial range still appears to be compatible with the zero-mode prediction $\xi^F_{6\,0} - \xi^F_{2\,0} \approx 2.29$. Therefore, the harmonics of order $\ell = 4$ and 6 of the concentration flux display characteristics that are not incompatible with the existence of zero-modes.

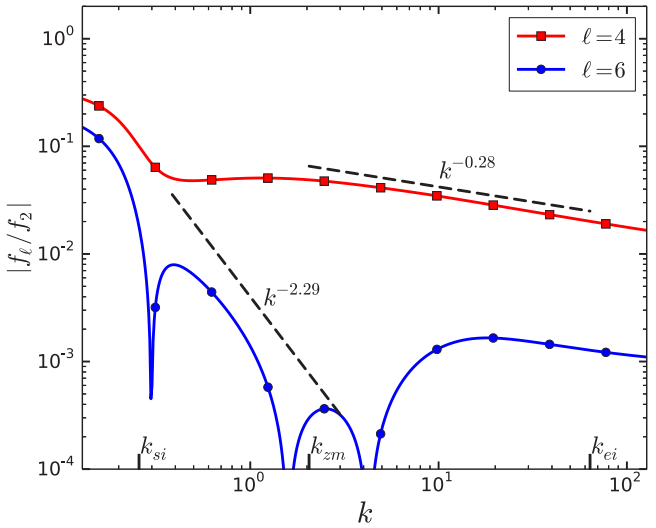

FIG. 18. Ratio $|f_\ell/f_2|$ for $\ell = 4$ and 6.

6. Concentration spectrum

The last spectrum we examine is the concentration spectrum. To begin with, we look at its second-order-harmonic component $b_2(k)$. Figure 19(a) shows that $b_2(k)$ decays faster than the isotropic spectrum $E_B(k)$ in the inertial range and becomes much smaller than E_B. This is similar to what was observed for the velocity spectrum and the first conclusions that can be drawn are identical to those expressed in Sec. VII A 4.

The second observation that can be made from Fig. 19(a) is that the sign of b_2 changes within the inertial range. With $b_2(k)$ being the sum of an equilibrium spectrum $b_2|^{\mathrm{ES}}$ and a zero-mode $b_2|^{\mathrm{ZM}}$, this change suggests that $b_2|^{\mathrm{ES}}$ and $b_2|^{\mathrm{ZM}}$ may have opposite signs. This hypothesis requires further confirmation.

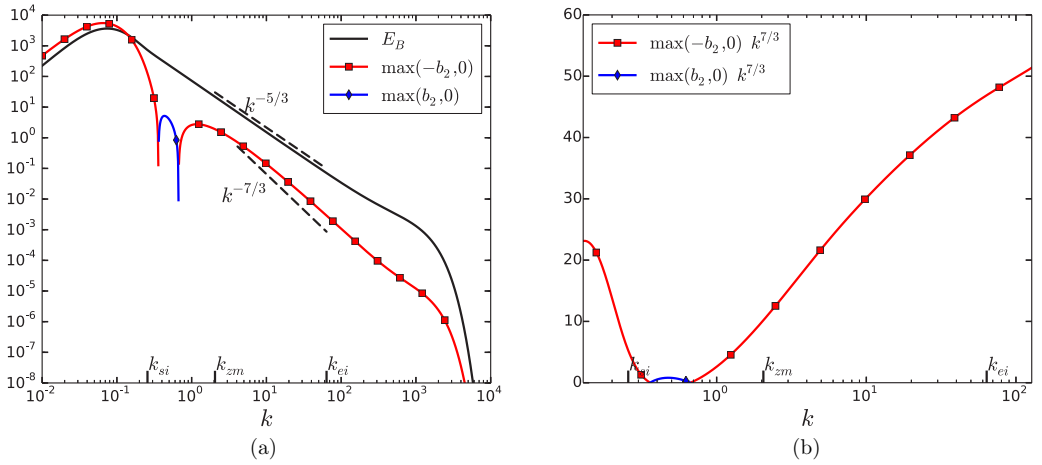

FIG. 19. Second-order harmonics of the concentration spectrum. (a) Comparison between b_0 and b_2. (b) Compensated spectra $b_2 k^{7/3}$.

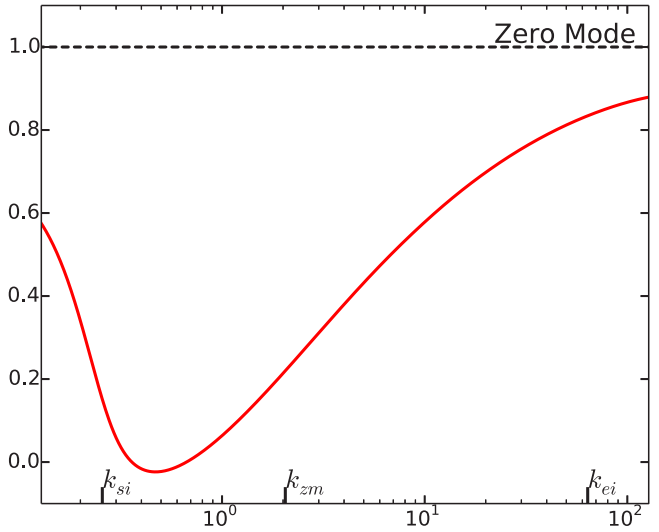

FIG. 20. Ratio between $b_2(k)$ and $b_2^{\mathrm{ZM}}(k)$.

We also observe in Fig. 19(a) that the inertial slope of $b_2(k)$ seems close to $7/3$ in the range $[k_{zm},k_{ei}]$, as is expected from the zero-mode analysis. However, the compensated spectrum $b_2k^{7/3}$ shown in Fig. 19(b) indicates that the actual slope converges very slowly as k increases and that it remains smaller than $7/3$ on the simulated range (but no smaller than 2.2). We note that the change of sign of b_2 limits the domains where power laws can be clearly identified.

Pursuing the analysis, we now look at the ratio between $b_2(k)$ and its zero-mode expression b_2^{ZM} as a function of r_2^{dir} and r_2^{pol}, as given by Eq. (20). It can be seen in Fig. 20 that this ratio is not constant but that it approaches its zero-mode value of 1 towards the end of the inertial range.

Finally, given Eq. (16) and the fact that r_2^{dir}, r_2^{pol}, and b_2 display scalings close to $k^{-7/3}$ for $k \geqslant k_{zm}$, the nonlinear transfer term T_2^B of b_2 should exhibit for $k \geqslant k_{zm}$ a scaling close to $k^{-5/3}$ except for the case when b_2 is a zero-mode. As shown in Fig. 21, T_2^B exhibits a clear $k^{-7/3}$ scaling, suggesting that b_2 behaves indeed as a zero-mode for $k \geqslant k_{zm}$, even if its properties do not match exactly the asymptotic predictions of the zero-mode analysis.

As a whole, these different observations suggest the presence of a zero-mode for the second-order harmonic of the concentration spectrum. Still, they do not allow us to corroborate firmly the predictions of the zero-mode analysis. Clear scalings or proportionality relationships cannot be put forward. This is partly linked to the change of sign of b_2, which seems to delay the establishment of such features. This change of sign itself can be explained by attributing opposite signs to the equilibrium and zero-mode contributions of the concentration spectrum. Despite these restrictions, the properties of the spectrum b_2 at the end of the inertial range seem to approach those expected from the zero-mode analysis. A larger EDQNM simulation would allow us to confirm this tendency.

Concerning the harmonics of order $\ell = 4$ and 6, we observe in Fig. 22 a rather unexpected feature: b_4 and b_6 appear to be much larger than the second-order harmonic b_2 in the interval $[k_{si},k_{zm}]$. While not shown here, b_4 and b_6 nonetheless remain much smaller than E_B, so the linearization of the EDQNM model is still valid. The harmonics b_4 and b_6 only become smaller than b_2 for $k \geqslant k_{zm}$, i.e., when zero-mode properties start to emerge. However, even in that range, b_4 and b_6 do not appear to decay faster than b_2, as is expected from the zero-mode theory. Thus, as for the higher harmonics of the velocity spectrum, there is a discrepancy between the predicted properties of b_4 and b_6 and the present EDQNM simulation. Reasons similar to those proposed at the end of Sec. VII A 4 can possibly explain this difference.

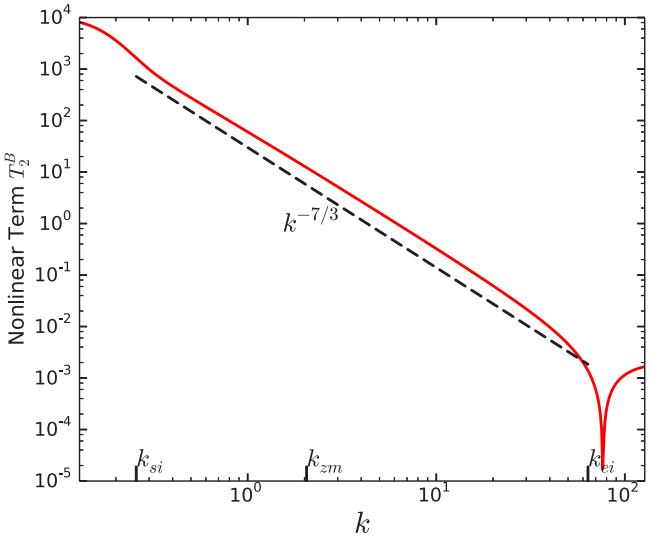

FIG. 21. Second-order harmonic of the nonlinear transfer term of B, T_2^B.

B. Large-eddy simulation of a Rayleigh-Taylor flow

1. Description of the simulation

As a last step in the validation of the results obtained in this article, we perform an implicit large-eddy simulation (ILES) of Rayleigh-Taylor turbulence. More details about ILES can be found in Ref. [43]. The reason for performing an ILES and not a DNS is that we are interested in inertial scales and want to minimize the extent of the dissipation range. The simulation is performed with the code TRICLADE, a massively parallel code intended to solve turbulent mixing of perfect gases in a variable density context [44,45]. A shock capturing scheme provides just enough numerical viscosity and diffusivity to ensure stability. More precisely, for this work, the monotonic upstream-centered scheme for conservation laws–based finite-volume Godunov method referred to as M5 in Ref. [45]

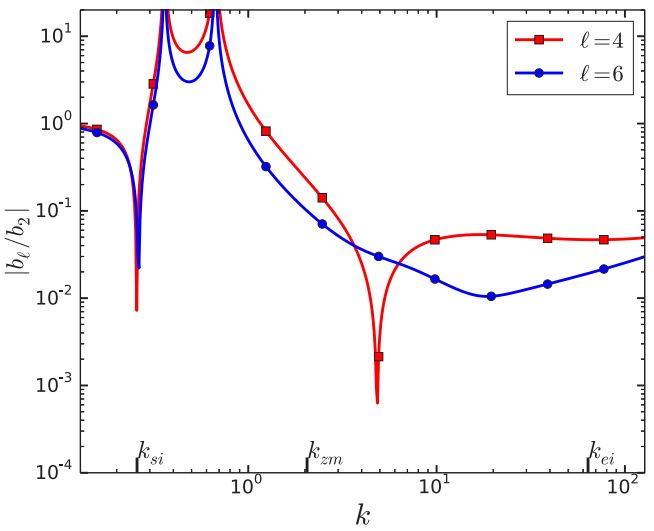

FIG. 22. Ratio $|b_\ell/b_2|$ for $\ell = 4$ and 6.

TABLE I. Simulation parameters in nondimensional units.

Parameter	Quantity
Atwood number $\mathtt{A}_t = \frac{\rho_h - \rho_l}{\rho_h + \rho_l}$	0.1
stratification	isentropic
grid resolution	$1024 \times 1024 \times 1200$

is used. It is accurate to fifth order in space and is combined with a low-storage strong stability preserving Runge-Kutta scheme of third-order time accuracy. The one-dimensional total variation diminishing limiter of [46] is used in reconstructing the primitive variables in order to ensure the total variation diminishing property. The simple low-dissipation advection upstream splitting method's numerical flux of [47] is used at each cell face due to its good performances in the low-Mach-number limit as shown in Ref. [45].

Table I summarizes the main parameters of the simulation. The grid is regular at the center of the domain on a cube of size $1024 \times 1024 \times 1024$. Two grids with a geometric progression are added at both ends of this cube in the inhomogeneous direction.

The simulation is initialized by imposing a random perturbation of the vorticity field on a slab of thickness $4\Delta x$ centered at the interface. The perturbation is initialized by setting a broadband spectrum peaking at $\kappa \approx \frac{\pi}{4\Delta x}$ and decaying as κ^4 for $\kappa \to 0$.

In order to improve the statistical accuracy of the results, this simulation is repeated four times, keeping all parameters constant except for the seed of the random generator used to create the initial perturbation. The results shown below are all ensemble averaged over these four simulations, at each physical time t^*, in addition to using a spatial average operator over the homogeneous directions.

The simulation reaches a self-similar state characterized by a quadratic growth of the mixing zone width L:

$$L = 2\alpha \mathtt{A}_t g t^2.$$

Figure 23 displays the evolution of α, computed by the formula $\alpha = \frac{(d_t L)^2}{8\mathtt{A}_t g L}$, with L defined by the expression $L = 6\int \overline{c}(1-\overline{c})dx_3^\star$. It can be seen that α tends to a self-similar value close to 0.02, in agreement with other numerical simulations [7,48].

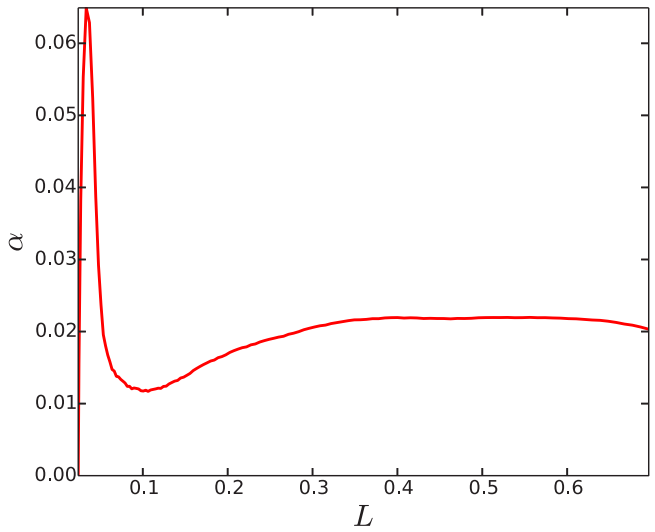

FIG. 23. Evolution of α as a function of the mixing zone width L.

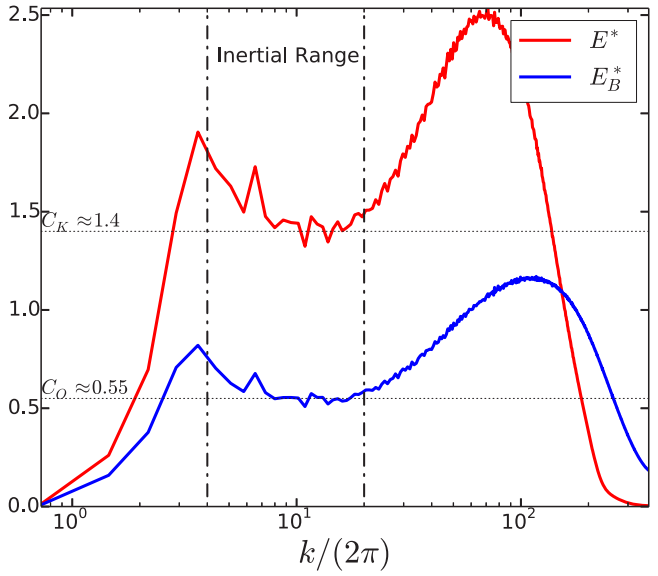

FIG. 24. Compensated energy and concentration modulus spectra $E(k,t)$ and $E_B(k,t)$ at the final time of the simulation.

In the remainder of this section, we will work with nondimensional variables, as we did for USH flows. These variables are defined identically to the USH case by Eq. (2). The only difference is the definition of L, which is here taken equal to the mixing zone size. In particular, the wave number $k = 2\pi$ corresponds to the mixing zone size.

As a last remark, we would like to stress that we do not have access to the local values of the dissipations of the kinetic energy and scalar variance, since we are using an implicit LES. However, when the flow becomes self-similar, we can use the formula derived in Ref. [49] to find the volume-averaged dissipations as a function of the second-order correlations of velocity and concentration. These formulas yield

$$\langle\overline{\varepsilon}\rangle = \langle\overline{u_3 c}\rangle(1 - 12\langle\overline{u_j u_j}\rangle), \quad \langle\overline{\varepsilon}_B\rangle = 2\langle\overline{u_3 c}\rangle(1 - 6\langle\overline{c'^2}\rangle), \tag{28}$$

where

$$\langle\cdots\rangle = \int \cdots dx_3 = \frac{1}{L}\int \cdots dx_3^\star.$$

2. *Inertial range scalings*

In order to verify whether an inertial range appears in the simulation, we plot in Fig. 24, at the end of the simulation, the normalized spectra $E^*(k) = \frac{E(k)}{\langle\overline{\varepsilon}\rangle^{2/3}k^{-5/3}}$ and $E_B^*(k) = \frac{E_B(k)}{\langle\overline{\varepsilon}_B\rangle\langle\overline{\varepsilon}\rangle^{-1/3}k^{-5/3}}$. From $k \approx 4$ to $k \approx 20$, both normalized spectra exhibit a slow variation, which suggests a scaling close to the Kolmogorov-Obukhov one. In addition, in this range, the values of E^* and E_B^* are compatible with a Kolmogorov constant $C_K \approx 1.4$ and an Obukhov constant $C_O \approx 0.55$. Thus, from $k \approx 4$ to $k \approx 20$, the flow displays an interval of scales with characteristics close to those expected from an inertial range. This range is at most half a decade long. While this is not insignificant, all the scaling estimates that will be presented below should be considered with great caution.

In addition, there is also another restriction due to the small extent of this range: If we assume that the EDQNM simulation of Sec. VII A is relevant to this Rayleigh-Taylor configuration, then we will only be able to observe the interval $k \leqslant k_{zm}$ where the imprint of the equilibrium spectrum

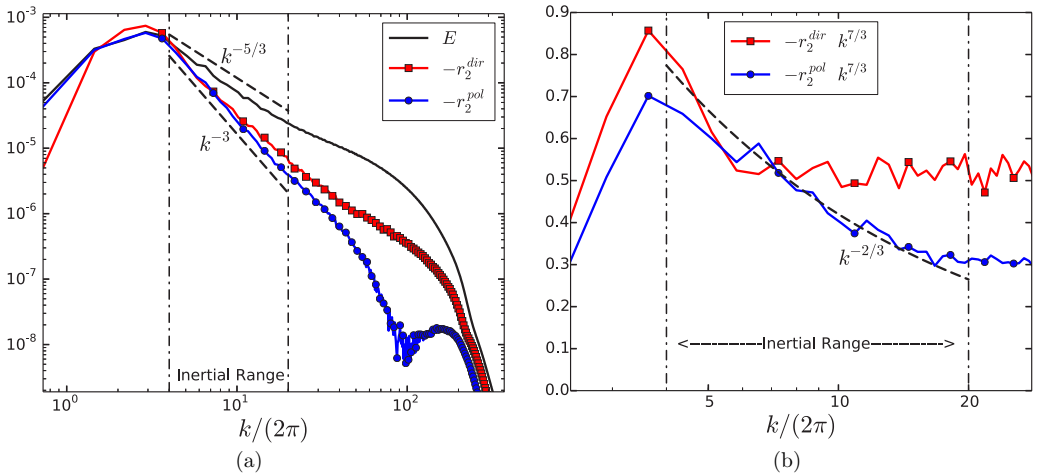

FIG. 25. Second-order harmonics of the velocity spectrum for the Rayleigh-Taylor simulation. (a) Comparison between E, r_2^{dir}, and r_2^{pol}. (b) Compensated spectra $r_2^{\mathrm{dir}}k^{7/3}$ and $r_2^{\mathrm{pol}}k^{7/3}$.

is still strong. The inertial range will not be large enough to reach a subinterval fully dominated by zero-modes.

3. *Velocity spectrum*

We begin by examining the second-order harmonics of the velocity spectrum. Figure 25(a) shows that $r_2^{\mathrm{dir}}(k)$ and $r_2^{\mathrm{pol}}(k)$ decay faster than $E(k)$ in the inertial range, as was the case in the EDQNM simulation of USH turbulence. To estimate the inertial slopes of $r_2^{\mathrm{dir}}(k)$ and $r_2^{\mathrm{pol}}(k)$, we plot in Fig. 25(b) the compensated spectra $r_2^{\mathrm{dir}}k^{7/3}$ and $r_2^{\mathrm{pol}}k^{7/3}$, zooming in on the inertial interval. For the compensated directional spectrum we observe a plateau, indicating that the scaling of $r_2^{\mathrm{dir}}(k)$ is close to $-7/3$. For the compensated polarization spectrum, we observe a decay agreeing with a $k^{-2/3}$ variation and indicating that $r_2^{\mathrm{pol}}(k)$ scales approximately as k^{-3}.

These observations are compatible with the superposition of a k^{-3} equilibrium spectrum and a $k^{-7/3}$ zero-mode as predicted in Eq. (24). They also agree with the EDQNM simulations of USH turbulence presented in Sec. VII A: The variations of $r_2^{\mathrm{dir}}(k)$ and $r_2^{\mathrm{pol}}(k)$ are similar to those observed in Fig. 9(b) for the largest scales of the inertial range ($k \leqslant k_{zm}$).

Figure 26(a) shows the ratio $r_2^{\mathrm{dir}}/r_2^{\mathrm{pol}}$ in the interval identified as the inertial range. It can be seen that this ratio increases with k and that it departs from the value of 1 predicted by the equilibrium assumption, in agreement with the presence of a zero-mode. The largest value of this ratio, obtained at the end of the inertial range, is about 1.8 and is still far from the asymptotic one predicted by the zero-mode analysis. This is not unexpected: As shown in Fig. 12(b) for the EDQNM simulation, this maximum value increases slowly with the Reynolds number. Convergence only occurs at Reynolds numbers above 3×10^5, corresponding to inertial ranges much larger than the one obtained in the present LES. From Fig. 12(b) we also see that a ratio of 1.8 would be obtained from an EDQNM simulation with a Reynolds number on the order of 10^4, corresponding approximately to an inertial range of about half a decade. This is on par with the present LES.

Finally, we display in Fig. 26(b) the nonlinear frequencies $|T_2^{\mathrm{dir}}/r_2^{\mathrm{dir}}|$ and $|T_2^{\mathrm{pol}}/r_2^{\mathrm{pol}}|$. As already explained (see Sec. IV B), these frequencies should evolve as $k^{2/3}$ save for the presence of zero-modes. We see that the polarization frequency $|T_2^{\mathrm{pol}}/r_2^{\mathrm{pol}}|$ evolves indeed as $k^{2/3}$, while $|T_2^{\mathrm{dir}}/r_2^{\mathrm{dir}}|$ does not. This result agrees with previous observations and is coherent with the presence of a zero-mode yielding a dominant contribution for r_2^{dir} and subdominant one for r_2^{pol}.

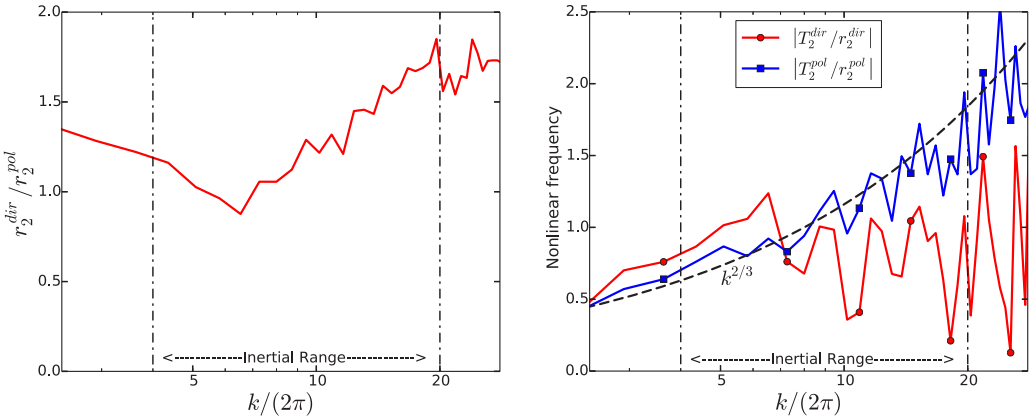

FIG. 26. (a) Ratio $r_2^{\mathrm{dir}}/r_2^{\mathrm{pol}}$. (b) Nonlinear frequencies $|T_2^{\mathrm{dir}}/r_2^{\mathrm{dir}}|$ and $|T_2^{\mathrm{pol}}/r_2^{\mathrm{pol}}|$.

As a whole, the different observations made in Figs. 25 and 26 all point to the presence of zero-modes in the second-order harmonics of the velocity spectrum. This body of corroborating evidence requires further confirmation that can only be achieved by performing larger simulations. In particular, it would be interesting to see if the inertial slope of r_2^{pol} indeed changes to $7/3$ and to determine if the asymptotic value of the ratio $r_2^{\mathrm{dir}}/r_2^{\mathrm{pol}}$ corresponds to its zero-mode prediction.

Concerning higher-order harmonics, simulation results are not displayed but can be summed up as follows: Harmonics of order 4 and 6 are much smaller than the harmonic of order 2. Other than that, their properties appear to be different from those predicted by the zero-mode analysis. This is similar to what was observed in EDQNM simulations and the possible reasons for explaining these differences are the same as those proposed at the end of Sec. VII A 4.

4. Concentration flux spectrum

Figure 27(a) shows $f_2(k)$, the second harmonic of the concentration flux spectrum for the Rayleigh-Taylor simulation. The inertial slope of the flux spectrum is found to be close to $-7/3$.

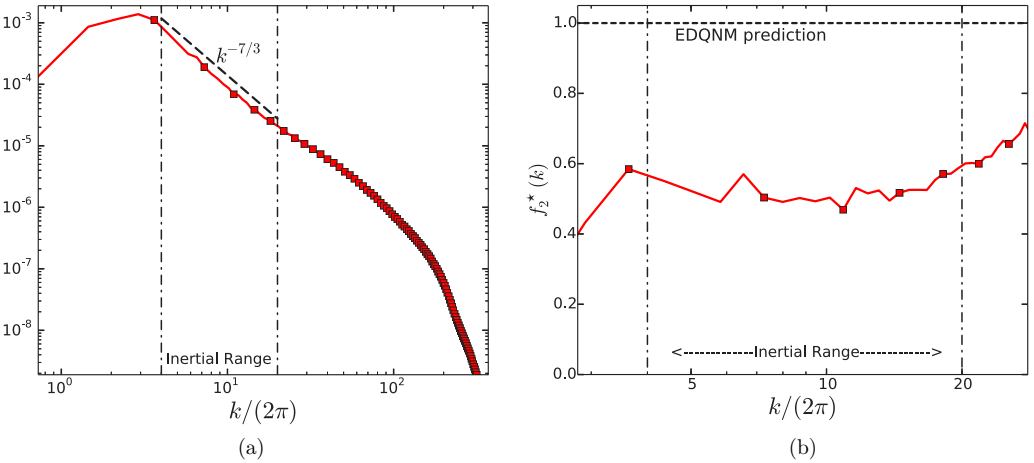

FIG. 27. Second-order harmonic of the concentration flux $f_2(k)$ for the Rayleigh-Taylor simulation (a) without renormalization and (b) with a $k^{7/3}$ renormalization: $f_2^\star = \frac{f_2}{c_F\langle\bar{\varepsilon}\rangle^{1/3}(c_K+c_O\langle\bar{\varepsilon}_B\rangle/\langle\bar{\varepsilon}\rangle)k^{-7/3}}$.

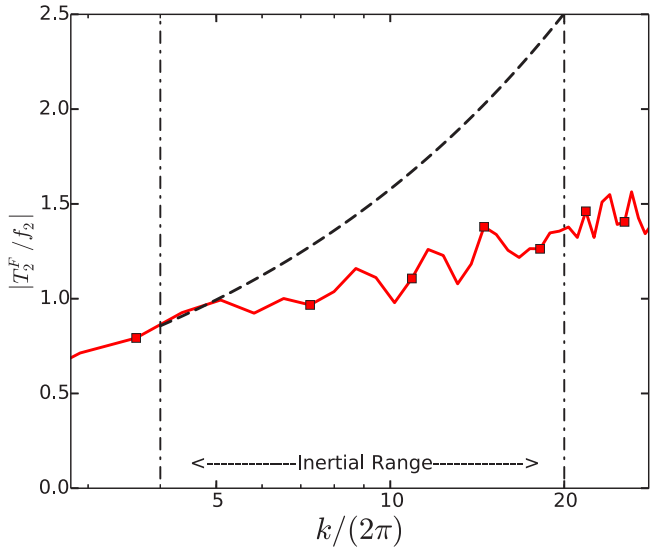

FIG. 28. Nonlinear frequency $|T_2^F/f_2|$.

Zooming in on the inertial range previously identified in Sec. VII B 2, we show in Fig. 27(b) the normalized spectrum $f_2^\star = \frac{f_2}{c_F\langle\bar{\varepsilon}\rangle^{1/3}(c_K+c_O\langle\bar{\varepsilon}_B\rangle/\langle\bar{\varepsilon}\rangle)k^{-7/3}}$, with constants set to $c_F = 3.8$, $c_K = 1.4$, and $c_0 = 0.55$. The latter two values are chosen in agreement with Fig. 24. Variations of less than 20% in relative value are observed for $f_2^\star(k)$, confirming that the scaling of $f_2(k)$ is close to $-7/3$. Comparing Fig. 27(a) to its EDQNM equivalent in Fig. 14(b) may lead to the impression that the variations of $f_2^\star(k)$ in the EDQNM case are much stronger than those obtained in the LES case. However, most of this impression comes from the different scales of the figures and the different inertial range sizes. Focusing on the first half decade of inertial range in Fig. 14(b), one can measure relative variations of $f_2^\star(k)$ on the order of 25% for the EDQNM simulation. This is larger than but still on the same order as the variation observed in the LES case.

In addition, we note that the value of the plateau of $f_2^\star$ is about 0.5, i.e., half as big as the one predicted by the EDQNM model. Still, the EDQNM prediction is only for asymptotically small scales. The first half decade of the inertial range of the EDQNM simulation shown in Fig. 14(b) shows values of $f_2^\star$ that are also on the order of 0.5.

Unfortunately, the inspection of the second-order-harmonic spectrum of the flux f_2 does not give any clue as to the presence of a zero-mode. The small extent of the inertial range does not allow us to separate scalings as close as $k^{-7/3}$ and $k^{-7/3-\delta\xi^F}$ with $\delta\xi^F = 0.13$. There is still one more piece of information that can be looked at: According to Eq. (16), the nonlinear frequency $|T_2^F/f_2|$ is expected to scale as $k^{2/3}$ in the inertial range, save for the presence of a zero-mode. Figure 28 shows that $|T_2^F/f_2|$ scales differently from $k^{2/3}$, indicating that a zero-mode may be present. However, this sole indication is certainly not sufficient to make any definitive conclusions about the presence of zero-modes. We also note that in the derivation of the equilibrium spectrum [8], it is explicitly assumed that $|T_2^F/f_2|$ scales as $k^{2/3}$. Figure 28 consequently shows that the equilibrium explanation is not fully satisfactory and that an element is missing.

5. Concentration spectrum

As in the EDQNM simulation, one of the most striking features of the second-order harmonic of the concentration spectrum b_2 in the inertial range is that its sign changes. As shown in Fig. 29(a), from the middle to the end of the inertial range, b_2 is positive, while it is negative for energetic scales. In the EDQNM case, this positive interval was followed for larger k by another negative one

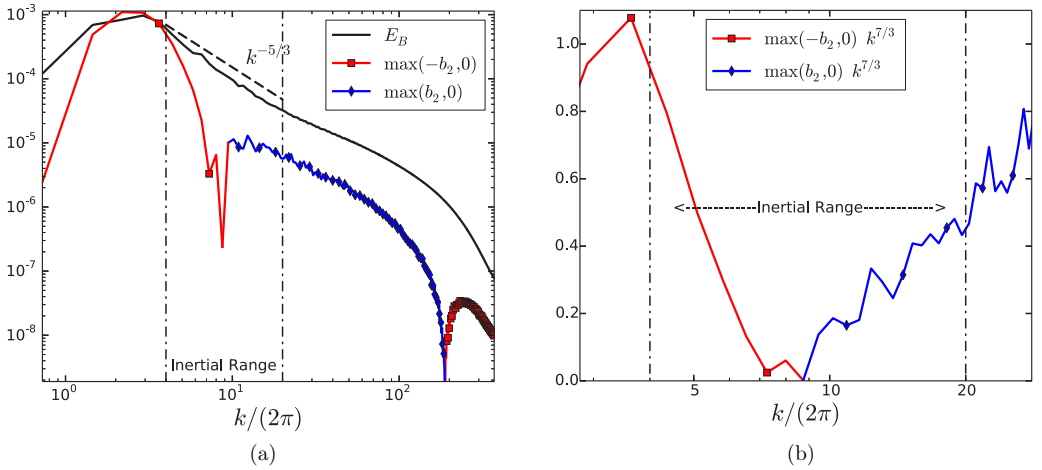

FIG. 29. Second-order harmonics of the concentration spectrum for the Rayleigh-Taylor simulation. (a) Comparison between b_0 and b_2. (b) Compensated spectra $b_2 k^{7/3}$.

displaying approximately zero-mode properties. In the present LES simulation, the small extent of the inertial range does not allow us to determine whether another negative interval will appear in the inertial range. In addition, as in the EDQNM case, the change of sign prevents the identification of any clear scaling, as can be seen from Fig. 29(b). Therefore, no conclusion can be drawn about the influence of zero-modes on b_2 in this simulation.

VIII. CONCLUSION

The purpose of this work was to study the anisotropic properties of the inertial range of USH and Rayleigh-Taylor turbulence. Following [22–24], two main physical mechanisms are expected to control these properties. The first one corresponds to the direct and local action of buoyancy forces and gives rise to equilibrium spectra. The second one results from the nonlocal action of transfer terms and translates into the apparition of zero-modes, i.e., of modes that nullify the anisotropic part of transfer terms. The issue at stake in this article was to determine which of these two physical mechanisms sustains anisotropy for small inertial scales. The equilibrium mechanism was already studied in Ref. [8] and leads to a k^{-3} scaling for the velocity and concentration anisotropic spectra and to a $k^{-7/3}$ scaling for the concentration flux spectrum. The study of the second mechanism, i.e., of the properties of zero-modes, was the main objective of the present paper.

To determine zero-mode properties, we performed a zero-mode analysis of the EDQNM model proposed in Ref. [19] with the procedure developed in Ref. [24]. From this analysis, we derived that the velocity and concentration zero-modes display approximate $k^{-7/3}$ scalings. As a consequence, velocity and concentration zero-modes become predominant at very small scales compared to their equilibrium counterparts, which, we recall, scale as k^{-3}. Therefore, one of the main result of this study is that, at the smallest scales of the inertial range, the anisotropy of the velocity and concentration spectra is maintained by the nonlocal action of nonlinear terms and scales approximately as $k^{-7/3}$.

As for the concentration flux, the zero-mode analysis also yields an approximate $k^{-7/3}$ scaling. This scaling is close to the equilibrium scaling, but is different from it. This small difference is such that the zero-mode contribution will eventually become subdominant as k increases. Therefore, the conclusion is here the converse of the one obtained for the velocity and concentration spectra: At the smallest scales of the inertial range, the anisotropy of the concentration flux spectrum is due to the direct and local action of buoyancy forces. In addition, we also derived another noticeable result for the concentration flux spectrum. Indeed, the zero-mode contribution decays only slightly

more rapidly than the corresponding equilibrium contribution. When cast in terms of Reynolds numbers, this property implies that the inertial slope of the concentration flux exhibits a slow convergence to $-7/3$. Therefore, zero-modes provide a possible explanation for observations of this slow convergence, which have already been made in different contexts [28,29].

To verify these predictions, we performed an EDQNM simulation of USH turbulence at a Reynolds number of 10^7. This simulation confirmed the presence of zero-modes in the inertial range for the second-order harmonic of the velocity spectrum. The scalings and ratio of the directional and polarization anisotropy were found to be close to the ones derived from the zero-mode analysis. In addition, the influence of zero-modes was also detected for the second-order harmonic of the concentration flux spectrum through the slow convergence of its inertial slope to $-7/3$. As for the second-order harmonic of the concentration spectrum, it displayed properties that approached those predicted by the zero-mode analysis for the smallest scales of the inertial range. However, a larger simulation would be required to confirm whether this tendency is real or not.

Finally, we performed a LES of Rayleigh-Taylor turbulence in order to check whether zero-modes could be identified in the configuration that originally motivated the study. The main difficulty in achieving this task lay in the small extent of the simulated inertial range. This prevented the identification of clear scalings and of any other asymptotic properties of the spectra. Nonetheless, keeping this limitation in mind, the velocity spectrum appeared to display features that were compatible with the predictions of this work. In particular, the second-order harmonic of the directionality spectrum showed a clear departure from the k^{-3} scaling originally proposed in Ref. [8] and seemed to be compatible with the $k^{-7/3}$ scaling of zero-modes. As for the concentration and concentration flux spectra, no sign of zero-modes could be firmly exhibited. Independently of these results on zero-modes, good agreement was observed between LES and EDQNM simulations when comparing inertial ranges of similar extents.

ACKNOWLEDGMENT

The authors would like to thank Dr J. Griffond (CEA, DAM, DIF) for useful discussions and for helping to carry out the numerical simulations of this work.

APPENDIX A: LINEARIZED TRANSFER TERMS OF THE EDQNM MODEL

Neglecting terms quadratic in r_{ij}, b, and f in Eqs. (5), we deduce the following linear approximation for the EDQNM transfer terms in the inertial range:

$$T^R_{ab}(\boldsymbol{k}) = \int_{\boldsymbol{k}+\boldsymbol{k}'+\boldsymbol{k}''=0} M^R_{abcd}(\boldsymbol{k},\boldsymbol{k}',\boldsymbol{k}'') r_{cd}(\boldsymbol{k}')d\boldsymbol{k}' + \int_{\boldsymbol{k}+\boldsymbol{k}'+\boldsymbol{k}''=0} N^R_{abcd}(\boldsymbol{k},\boldsymbol{k}',\boldsymbol{k}'')d\boldsymbol{k}' r_{cd}(\boldsymbol{k}) + \int_{\boldsymbol{k}+\boldsymbol{k}'+\boldsymbol{k}''=0} \Theta^{\mathrm{dir}}(\boldsymbol{k},\boldsymbol{k}',\boldsymbol{k}'') Q^R_{ab}(\boldsymbol{k},\boldsymbol{k}',\boldsymbol{k}'')d\boldsymbol{k}', \tag{A1a}$$

$$T^B(\boldsymbol{k}) = \int_{\boldsymbol{k}+\boldsymbol{k}'+\boldsymbol{k}''=0} M^B(\boldsymbol{k},\boldsymbol{k}',\boldsymbol{k}'') b(\boldsymbol{k}')d\boldsymbol{k}' + \int_{\boldsymbol{k}+\boldsymbol{k}'+\boldsymbol{k}''=0} N^B(\boldsymbol{k},\boldsymbol{k}',\boldsymbol{k}'')d\boldsymbol{k}' b(\boldsymbol{k}) + \int_{\boldsymbol{k}+\boldsymbol{k}'+\boldsymbol{k}''=0} S^B_{ab}(\boldsymbol{k},\boldsymbol{k}',\boldsymbol{k}'') r_{ab}(\boldsymbol{k}')d\boldsymbol{k}' + \int_{\boldsymbol{k}+\boldsymbol{k}'+\boldsymbol{k}''=0} \Theta^{\mathrm{dir}}(\boldsymbol{k},\boldsymbol{k}',\boldsymbol{k}'') Q^B(\boldsymbol{k},\boldsymbol{k}',\boldsymbol{k}'')d\boldsymbol{k}', \tag{A1b}$$

$$T^F_a(\boldsymbol{k}) = \int_{\boldsymbol{k}+\boldsymbol{k}'+\boldsymbol{k}''=0} M^F_{ab}(\boldsymbol{k},\boldsymbol{k}',\boldsymbol{k}'') f_b(\boldsymbol{k}')d\boldsymbol{k}' + \int_{\boldsymbol{k}+\boldsymbol{k}'+\boldsymbol{k}''=0} N^F_{ab}(\boldsymbol{k},\boldsymbol{k}',\boldsymbol{k}'')d\boldsymbol{k}' f_b(\boldsymbol{k}), \tag{A1c}$$

with

$$M^R_{abcd}(\boldsymbol{k},\boldsymbol{k}',\boldsymbol{k}'') = \Theta^{\mathrm{KO}}_{kk'k''} \mathcal{P}_{alm}(\hat{\boldsymbol{k}})\big[k\mathcal{P}_{bdj}(\hat{\boldsymbol{k}}) R^{\mathrm{KO}}_{ij}(\boldsymbol{k}'') + k''\mathcal{P}_{idj}(\hat{\boldsymbol{k}}'') R^{\mathrm{KO}}_{ij}(\boldsymbol{k})\big] + \text{Sym. } a \leftrightarrow b, \tag{A1d}$$

$$N^R_{abcd}(\boldsymbol{k},\boldsymbol{k}',\boldsymbol{k}'') = \Theta^{\mathrm{KO}}_{kk'k''} kk'' \mathcal{P}_{aij}(\hat{\boldsymbol{k}}) \mathcal{P}_{ikc}(\hat{\boldsymbol{k}}') R^{\mathrm{KO}}_{kj}(\boldsymbol{k}'')\delta_{bd} + \text{Sym. } a \leftrightarrow b, \tag{A1e}$$

$$M^B(\boldsymbol{k},\boldsymbol{k}',\boldsymbol{k}'') = 2\Theta^{\mathrm{KO}}_{kk'k''} k_i k_j R^{\mathrm{KO}}_{ij}(\boldsymbol{k}''), \tag{A1f}$$

$$N^B(\boldsymbol{k},\boldsymbol{k}',\boldsymbol{k}'') = 2\Theta^{\mathrm{KO}}_{kk'k''} k_i k'_j R^{\mathrm{KO}}_{ij}(\boldsymbol{k}''), \tag{A1g}$$

$$S^B_{ab}(\boldsymbol{k},\boldsymbol{k}',\boldsymbol{k}'') = 2\Theta^{\mathrm{KO}}_{kk'k''} k_a [k_b B^{\mathrm{KO}}(\boldsymbol{k}'') + k''_b B^{\mathrm{KO}}(\boldsymbol{k})], \tag{A1h}$$

$$M^F_{ab}(\boldsymbol{k},\boldsymbol{k}',\boldsymbol{k}'') = \Theta^{\mathrm{KO}}_{kk'k''} k_j \big\{ 2k\mathcal{P}_{abi}(\hat{\boldsymbol{k}}) R^{\mathrm{KO}}_{ij}(\boldsymbol{k}'') + k''[\mathcal{P}_{jbi}(\hat{\boldsymbol{k}}'') + \delta_{jb}\hat{k}''_i] R^{\mathrm{KO}}_{ai}(\boldsymbol{k}) \big\}, \tag{A1i}$$

$$N^F_{ab}(\boldsymbol{k},\boldsymbol{k}',\boldsymbol{k}'') = \Theta^{\mathrm{KO}}_{kk'k''} kk' [\mathcal{P}_{ali}(\hat{\boldsymbol{k}}) \mathcal{P}_{lbj}(\hat{\boldsymbol{k}}') + \hat{k}_i \hat{k}'_j \delta_{ab}] R^{\mathrm{KO}}_{ij}(\boldsymbol{k}''), \tag{A1j}$$

$$\begin{aligned} Q^R_{ab}(\boldsymbol{k},\boldsymbol{k}',\boldsymbol{k}'') = \frac{k}{2} \mathcal{P}_{alm}(\hat{\boldsymbol{k}}) \big[& k \mathcal{P}_{bij}(\hat{\boldsymbol{k}}) R^{\mathrm{KO}}_{il}(\boldsymbol{k}') R^{\mathrm{KO}}_{jm}(\boldsymbol{k}'') \\ & + k' \mathcal{P}_{lij}(\hat{\boldsymbol{k}}') R^{\mathrm{KO}}_{ib}(\boldsymbol{k}) R^{\mathrm{KO}}_{jm}(\boldsymbol{k}'') \\ & + k'' \mathcal{P}_{mij}(\hat{\boldsymbol{k}}'') R^{\mathrm{KO}}_{ib}(\boldsymbol{k}) R^{\mathrm{KO}}_{jl}(\boldsymbol{k}') \big] + \text{Sym. } a \leftrightarrow b, \end{aligned} \tag{A1k}$$

$$Q^B_{ab}(\boldsymbol{k},\boldsymbol{k}',\boldsymbol{k}'') = 2k_i \{ k_j \big[R^{\mathrm{KO}}_{ij}(\boldsymbol{k}'') B^{\mathrm{KO}}(\boldsymbol{k}') \big] + k'_j \big[R^{\mathrm{KO}}_{ij}(\boldsymbol{k}'') B^{\mathrm{KO}}(\boldsymbol{k}) \big] \}, \tag{A1l}$$

and

$$\Theta^{\mathrm{KO}} = \frac{1}{c_\gamma \bar{\varepsilon}^{2/3} (k^{2/3} + k'^{2/3} + k''^{2/3})}, \quad \Theta^{\mathrm{dir}} = -(\Theta^{\mathrm{KO}})^2 [3a_1 N + \eta^{\mathrm{dir}}(k) + \eta^{\mathrm{dir}}(k') + \eta^{\mathrm{dir}}(k'')], \tag{A1m}$$

where $\eta^{\mathrm{dir}}(k) = a_0 [\int_{k' \leqslant k} k'^2 r_{jj}(\boldsymbol{k}') d\boldsymbol{k}'/2]^{1/2}$ and $c_\gamma = a_0 (3c_K/4)^{1/2}$. Substituting the definitions of R^{KO}_{ij} and B^{KO} in these expressions, making the change of variables $\boldsymbol{k}' \leftarrow \boldsymbol{k}'/k$ and $\boldsymbol{k}'' \leftarrow \boldsymbol{k}''/k$ in the integrals, and neglecting the Θ^{dir} contributions, we eventually obtain

$$\begin{aligned} T^R_{ab}(\boldsymbol{k}) = \frac{c_T \bar{\varepsilon}^{1/3} k^{2/3}}{4\pi} \bigg(& \int_{\hat{\boldsymbol{k}}+\hat{\boldsymbol{k}}'+\hat{\boldsymbol{k}}''=0} M^R_{abcd}(\hat{\boldsymbol{k}},\boldsymbol{k}',\boldsymbol{k}'') r_{cd}(k\boldsymbol{k}') d\boldsymbol{k}' \\ & + \int_{\hat{\boldsymbol{k}}+\hat{\boldsymbol{k}}'+\hat{\boldsymbol{k}}''=0} N^R_{abcd}(\hat{\boldsymbol{k}},\boldsymbol{k}',\boldsymbol{k}'') d\boldsymbol{k}' r_{cd}(\boldsymbol{k}) \bigg), \end{aligned} \tag{A2a}$$

$$\begin{aligned} T^B(\boldsymbol{k}) = \frac{2c_T \bar{\varepsilon}^{1/3} k^{2/3}}{4\pi} \bigg(& \int_{\hat{\boldsymbol{k}}+\hat{\boldsymbol{k}}'+\hat{\boldsymbol{k}}''=0} M^B(\hat{\boldsymbol{k}},\boldsymbol{k}',\boldsymbol{k}'') b(k\boldsymbol{k}') d\boldsymbol{k}' + \int_{\hat{\boldsymbol{k}}+\hat{\boldsymbol{k}}'+\hat{\boldsymbol{k}}''=0} N^B(\hat{\boldsymbol{k}},\boldsymbol{k}',\boldsymbol{k}'') d\boldsymbol{k}' b(\boldsymbol{k}) \\ & + \frac{c_O \bar{\varepsilon}_B}{c_K \bar{\varepsilon}} \int_{\hat{\boldsymbol{k}}+\hat{\boldsymbol{k}}'+\hat{\boldsymbol{k}}''=0} S^B_{ab}(\hat{\boldsymbol{k}},\boldsymbol{k}',\boldsymbol{k}'') r_{ab}(k\boldsymbol{k}') d\boldsymbol{k}' \bigg), \end{aligned} \tag{A2b}$$

$$T^F_a(\boldsymbol{k}) = \frac{c_T \bar{\varepsilon}^{1/3} k^{2/3}}{4\pi} \bigg(\int_{\hat{\boldsymbol{k}}+\hat{\boldsymbol{k}}'+\hat{\boldsymbol{k}}''=0} M^F_{ab}(\hat{\boldsymbol{k}},\boldsymbol{k}',\boldsymbol{k}'') f_b(k\boldsymbol{k}') d\boldsymbol{k}' + \int_{\hat{\boldsymbol{k}}+\hat{\boldsymbol{k}}'+\hat{\boldsymbol{k}}''=0} N^F_{ab}(\hat{\boldsymbol{k}},\boldsymbol{k}',\boldsymbol{k}'') d\boldsymbol{k}' f_b(\boldsymbol{k}) \bigg), \tag{A2c}$$

where $c_T = c_K/c_\gamma$, $c_\gamma = a_0(3c_K/4)^{1/2}$, and

$$M^R_{abcd}(\boldsymbol{k},\boldsymbol{k}',\boldsymbol{k}'') = \Theta^{\mathrm{KO}}_{k'k''} \mathcal{P}_{aci}(\hat{\boldsymbol{k}}) [\mathcal{P}_{bdj}(\hat{\boldsymbol{k}}) P_{ij}(\hat{\boldsymbol{k}}'') k''^{-11/3} + k'' \mathcal{P}_{idj}(\hat{\boldsymbol{k}}'') P_{bj}(\hat{\boldsymbol{k}})] + \text{Sym. } a \leftrightarrow b, \tag{A3a}$$

$$N^R_{abcd}(\boldsymbol{k},\boldsymbol{k}',\boldsymbol{k}'') = \Theta^{\mathrm{KO}}_{k'k''} k' k''^{-11/3} \mathcal{P}_{aij}(\hat{\boldsymbol{k}}) \mathcal{P}_{ikc}(\hat{\boldsymbol{k}}') P_{kj}(\hat{\boldsymbol{k}}'') \delta_{bd} + \text{Sym. } a \leftrightarrow b, \tag{A3b}$$

$$M^B(\boldsymbol{k},\boldsymbol{k}',\boldsymbol{k}'') = \Theta^{\mathrm{KO}}_{k'k''} k''^{-11/3} \hat{k}_i \hat{k}_j P_{ij}(\hat{\boldsymbol{k}}''), \tag{A3c}$$

$$N^B(\boldsymbol{k},\boldsymbol{k}',\boldsymbol{k}'') = \Theta^{\mathrm{KO}}_{k'k''} k' k''^{-11/3} \hat{k}_i \hat{k}'_j P_{ij}(\hat{\boldsymbol{k}}''), \tag{A3d}$$

$$S^B_{ab}(\boldsymbol{k},\boldsymbol{k}',\boldsymbol{k}'') = \Theta^{\mathrm{KO}}_{k'k''} \hat{k}_a (\hat{k}_b k''^{-11/3} + k'' \hat{k}''_b), \tag{A3e}$$

$$M^F_{ab}(\boldsymbol{k},\boldsymbol{k}',\boldsymbol{k}'') = \Theta^{\mathrm{KO}}_{k'k''}\hat{k}_j\{2k''^{-11/3}\mathcal{P}_{abi}(\hat{\boldsymbol{k}})P_{ij}(\hat{\boldsymbol{k}}'') + k''[\mathcal{P}_{jbi}(\hat{\boldsymbol{k}}'') + \delta_{jb}\hat{k}''_i]P_{ia}(\hat{\boldsymbol{k}})\}, \tag{A3f}$$

$$N^F_{ab}(\boldsymbol{k},\boldsymbol{k}',\boldsymbol{k}'') = \Theta^{\mathrm{KO}}_{k'k''}k'k''^{-11/3}P_{ij}(\hat{\boldsymbol{k}}'')[\mathcal{P}_{ali}(\hat{\boldsymbol{k}})\mathcal{P}_{lbj}(\hat{\boldsymbol{k}}') + \hat{k}_i\hat{k}'_j\delta_{ab}], \tag{A3g}$$

with

$$\Theta^{\mathrm{KO}}_{k'k''} = \frac{1}{1 + k'^{2/3} + k''^{2/3}}. \tag{A3h}$$

APPENDIX B: SPHERICAL HARMONIC DECOMPOSITION OF THE LINEARIZED TRANSFER TERMS

In order to project the linearized EDQNM transfer terms defined in Eq. (A2) onto the spherical harmonic decomposition, we apply the procedure proposed in Ref. [24]. This procedure is detailed here for the directional harmonics of T^R_{ab} only. The procedure is identical for the remaining harmonics of the nonlinear terms.

The directional harmonics of T^R_{ab} are defined as, for $\ell \geqslant 0$,

$$T^{\mathrm{dir}}_\ell(k) = \frac{2\ell+1}{2}k^2\int T^R_{ab}(\boldsymbol{k})P_{ab}(\hat{\boldsymbol{k}})Y_\ell(\cos\theta)d\hat{\boldsymbol{k}}. \tag{B1a}$$

Injecting the definition of the linearized EDQNM transfer terms Eq. (A2), we obtain that

$$\begin{aligned}\frac{T^{\mathrm{dir}}_\ell(k)}{\frac{2\ell+1}{8\pi}c_T\bar{\varepsilon}^{1/3}k^{2/3}} = 4\pi k^2\iint_{\hat{\boldsymbol{k}}+\hat{\boldsymbol{k}}'+\hat{\boldsymbol{k}}''=0}&\big[M^R_{abcd}(\hat{\boldsymbol{k}},\boldsymbol{k}',\boldsymbol{k}'')r_{cd}(k\boldsymbol{k}')\\ &+ N^R_{abcd}(\hat{\boldsymbol{k}},\boldsymbol{k}',\boldsymbol{k}'')r_{cd}(\boldsymbol{k})\big]P_{ab}(\hat{\boldsymbol{k}})Y_\ell(\cos\theta)d\boldsymbol{k}'d\hat{\boldsymbol{k}}.\end{aligned} \tag{B1b}$$

Injecting the spherical harmonics decomposition of $\boldsymbol{r}$, we derive that

$$\begin{aligned}&\frac{T^{\mathrm{dir}}_\ell(k)}{\frac{2\ell+1}{8\pi}c_T\bar{\varepsilon}^{1/3}k^{2/3}}\\ &= \sum_{m\geqslant 0}\iint_{\hat{\boldsymbol{k}}+\hat{\boldsymbol{k}}'+\hat{\boldsymbol{k}}''=0} M^R_{abcd}(\hat{\boldsymbol{k}},\boldsymbol{k}',\boldsymbol{k}'')\big[P_{cd}(\hat{\boldsymbol{k}}')r^{\mathrm{dir}}_m(kk')k'^{-2}Y_m(\cos\theta')\big]P_{ab}(\hat{\boldsymbol{k}})Y_\ell(\cos\theta)d\boldsymbol{k}'d\hat{\boldsymbol{k}}\\ &+ \sum_{m\geqslant 2}\iint_{\hat{\boldsymbol{k}}+\hat{\boldsymbol{k}}'+\hat{\boldsymbol{k}}''=0} M^R_{abcd}(\hat{\boldsymbol{k}},\boldsymbol{k}',\boldsymbol{k}'')\big[D_{cd}(\hat{\boldsymbol{k}}',\hat{\boldsymbol{n}})r^{\mathrm{pol}}_m(kk')k'^{-2}\ddot{Y}_m(\cos\theta')\big]P_{ab}(\hat{\boldsymbol{k}})Y_\ell(\cos\theta)d\boldsymbol{k}'d\hat{\boldsymbol{k}}\\ &+ \sum_{m\geqslant 0}r^{\mathrm{dir}}_m(k)\iint_{\hat{\boldsymbol{k}}+\hat{\boldsymbol{k}}'+\hat{\boldsymbol{k}}''=0} N^R_{abcd}(\hat{\boldsymbol{k}},\boldsymbol{k}',\boldsymbol{k}'')P_{cd}(\hat{\boldsymbol{k}})Y_m(\cos\theta)P_{ab}(\hat{\boldsymbol{k}})Y_\ell(\cos\theta)d\boldsymbol{k}'d\hat{\boldsymbol{k}}\\ &+ \sum_{m\geqslant 2}r^{\mathrm{pol}}_m(k)\iint_{\hat{\boldsymbol{k}}+\hat{\boldsymbol{k}}'+\hat{\boldsymbol{k}}''=0} N^R_{abcd}(\hat{\boldsymbol{k}},\boldsymbol{k}',\boldsymbol{k}'')D_{cd}(\hat{\boldsymbol{k}},\hat{\boldsymbol{n}})\ddot{Y}_m(\cos\theta)P_{ab}(\hat{\boldsymbol{k}})Y_\ell(\cos\theta)d\boldsymbol{k}'d\hat{\boldsymbol{k}}.\end{aligned} \tag{B1c}$$

As explained in Ref. [24], the result of the inner integrals $\int_{\hat{\boldsymbol{k}}+\hat{\boldsymbol{k}}'+\hat{\boldsymbol{k}}''=0}\cdots d\boldsymbol{k}'$ only depends on k and $\cos\theta$. Then, using the definition $\cos\theta = \hat{\boldsymbol{k}}\cdot\hat{\boldsymbol{n}}$, we can replace the outer integration over $\hat{\boldsymbol{k}}$ by an integration over $\hat{\boldsymbol{n}}$:

$$\iint_{\hat{\boldsymbol{k}}+\hat{\boldsymbol{k}}'+\hat{\boldsymbol{k}}''=0}\cdots d\boldsymbol{k}'d\hat{\boldsymbol{k}} = \iint_{\hat{\boldsymbol{k}}+\hat{\boldsymbol{k}}'+\hat{\boldsymbol{k}}''=0}\cdots d\boldsymbol{k}'d\hat{\boldsymbol{n}}.$$

The only terms depending explicitly on $\hat{\boldsymbol{n}}$ are the Legendre polynomials, their derivatives, and $D_{ab}(\hat{\boldsymbol{k}},\hat{\boldsymbol{n}})$. Therefore, exchanging the order of integration between $\boldsymbol{k}'$ and $\hat{\boldsymbol{n}}$ and

knowing that

$$\frac{2\ell+1}{4\pi}\int Y_\ell(\cos\theta)Y_m(\cos\theta')d\hat{\boldsymbol{n}} = Y_\ell(\hat{\boldsymbol{k}}\cdot\hat{\boldsymbol{k}}')\delta_{lm},$$
$$\frac{2\ell+1}{4\pi}\int Y_\ell(\cos\theta)D_{cd}(\hat{\boldsymbol{k}}',\hat{\boldsymbol{n}})\ddot{Y}_m(\cos\theta')d\hat{\boldsymbol{n}} = \hat{k}_i\hat{k}_j\mathcal{D}_{cdij}(\hat{\boldsymbol{k}}')\ddot{Y}_\ell(\hat{\boldsymbol{k}}\cdot\hat{\boldsymbol{k}}')\delta_{lm},$$
$$Y_\ell(1)=1,\quad \ddot{Y}_\ell(1)=\frac{(\ell-1)\ell(\ell+1)(\ell+2)}{8},$$

we obtain

$$\begin{aligned}\frac{T_\ell^{\rm dir}(k)}{\frac{c_T}{2}\bar{\varepsilon}^{1/3}k^{2/3}} &= \int_{\hat{\boldsymbol{k}}+\hat{\boldsymbol{k}}'+\hat{\boldsymbol{k}}''=0} M^R_{abcd}(\hat{\boldsymbol{k}},\hat{\boldsymbol{k}}',\hat{\boldsymbol{k}}'')P_{ab}(\hat{\boldsymbol{k}})P_{cd}(\hat{\boldsymbol{k}}')Y_\ell(\hat{\boldsymbol{k}}\cdot\hat{\boldsymbol{k}}')r_\ell^{\rm dir}(kk')k'^{-2}d\boldsymbol{k}'\\ &+\int_{\hat{\boldsymbol{k}}+\hat{\boldsymbol{k}}'+\hat{\boldsymbol{k}}''=0} M^R_{abcd}(\hat{\boldsymbol{k}},\hat{\boldsymbol{k}}',\hat{\boldsymbol{k}}'')P_{ab}(\hat{\boldsymbol{k}})\mathcal{D}_{cdij}(\hat{\boldsymbol{k}}')\hat{k}_i\hat{k}_j\ddot{Y}_\ell(\hat{\boldsymbol{k}}\cdot\hat{\boldsymbol{k}}')r_\ell^{\rm pol}(kk')k'^{-2}d\boldsymbol{k}'\\ &+r_\ell^{\rm dir}(k)\int_{\hat{\boldsymbol{k}}+\hat{\boldsymbol{k}}'+\hat{\boldsymbol{k}}''=0} N^R_{abcd}(\hat{\boldsymbol{k}},\hat{\boldsymbol{k}}',\hat{\boldsymbol{k}}'')P_{ab}(\hat{\boldsymbol{k}})P_{cd}(\hat{\boldsymbol{k}})d\boldsymbol{k}'\\ &+r_\ell^{\rm pol}(k)\frac{(\ell-1)\ell(\ell+1)(\ell+2)}{8}\int_{\hat{\boldsymbol{k}}+\hat{\boldsymbol{k}}'+\hat{\boldsymbol{k}}''=0} N^R_{abcd}(\hat{\boldsymbol{k}},\hat{\boldsymbol{k}}',\hat{\boldsymbol{k}}'')P_{ab}(\hat{\boldsymbol{k}})\mathcal{D}_{cdij}(\hat{\boldsymbol{k}})\hat{k}_i\hat{k}_j d\boldsymbol{k}'.\end{aligned} \tag{B2}$$

Now, as explained in Ref. [24], the integrand in the remaining integral over $\boldsymbol{k}'$ only depends on k' and $\hat{\boldsymbol{k}}'\cdot\hat{\boldsymbol{k}}$. Then, using spherical coordinates k', Θ', and Φ', with the angle Θ' defined from the axis $\hat{\boldsymbol{k}}$, we can neglect the dependence on Φ' and simplify the above integrals as

$$\begin{aligned}\frac{T_\ell^{\rm dir}(k)}{\frac{c_T}{2}\bar{\varepsilon}^{1/3}k^{2/3}} &= 2\pi\int_0^\infty r_\ell^{\rm dir}(kk')\int_{-1}^1 M^R_{abcd}(\hat{\boldsymbol{k}},\hat{\boldsymbol{k}}',-\hat{\boldsymbol{k}}'-\hat{\boldsymbol{k}})P_{ab}(\hat{\boldsymbol{k}})P_{cd}(\hat{\boldsymbol{k}}')Y_\ell(\mathtt{a})d\mathtt{a}\,dk'\\ &+2\pi\int_0^\infty r_\ell^{\rm pol}(kk')\int_{-1}^1 M^R_{abcd}(\hat{\boldsymbol{k}},\hat{\boldsymbol{k}}',-\hat{\boldsymbol{k}}'-\hat{\boldsymbol{k}})P_{ab}(\hat{\boldsymbol{k}})\mathcal{D}_{cdij}(\hat{\boldsymbol{k}}')\hat{k}_i\hat{k}_j\ddot{Y}_\ell(\mathtt{a})d\mathtt{a}\,dk'\\ &+2\pi r_\ell^{\rm dir}(k)\int_0^\infty k'^2\int_{-1}^1 N^R_{abcd}(\hat{\boldsymbol{k}},\hat{\boldsymbol{k}}',-\hat{\boldsymbol{k}}'-\hat{\boldsymbol{k}})P_{ab}(\hat{\boldsymbol{k}})P_{cd}(\hat{\boldsymbol{k}})d\mathtt{a}\,dk'\\ &+2\pi r_\ell^{\rm pol}(k)\frac{(\ell-1)\ell(\ell+1)(\ell+2)}{8}\\ &\times\int_0^\infty k'^2\int_{-1}^1 N^R_{abcd}(\hat{\boldsymbol{k}},\hat{\boldsymbol{k}}',-\hat{\boldsymbol{k}}-\hat{\boldsymbol{k}}')P_{ab}(\hat{\boldsymbol{k}})\mathcal{D}_{cdij}(\hat{\boldsymbol{k}})\hat{k}_i\hat{k}_j d\mathtt{a}\,dk',\end{aligned} \tag{B3}$$

where $\mathtt{a}=\cos(\hat{\boldsymbol{k}}\cdot\hat{\boldsymbol{k}}')=\cos(\Theta')$ and $\hat{\boldsymbol{k}}$ and $\boldsymbol{k}'$ are now expressed in a two-dimensional (2D) reference frame based on $\hat{\boldsymbol{k}}$ and on a second unit vector $\hat{\boldsymbol{z}}$ orthogonal to $\hat{\boldsymbol{k}}$ as

$$\hat{\boldsymbol{k}}=(0,1),\quad \boldsymbol{k}'=(k'\sqrt{1-\mathtt{a}^2},k'\mathtt{a}).$$

Thus, due to the reasoning proposed in Ref. [24], we expressed the directional harmonics of the linearized transfer terms of the velocity spectrum with 2D integrals. All that needs to be done is to replace the $r_\ell^{\rm dir}$ and $r_\ell^{\rm pol}$ with their power-law dependence given by Eq. (12).

The same procedure also applies to the remaining harmonics of the linearized transfer terms. It eventually yields Eq. (14). In these equations, the following definitions apply:

$$\begin{aligned}L_\ell^{ij}(\xi_\ell) &= \int_0^\infty k'^{-\xi_\ell}\int_{-1}^1 M^R_{abcd}(\hat{\boldsymbol{k}},\hat{\boldsymbol{k}}',-\hat{\boldsymbol{k}}'-\hat{\boldsymbol{k}})\Lambda^{ij}_{abcd}(\hat{\boldsymbol{k}},\hat{\boldsymbol{k}}')d\mathtt{a}\,dk'\\ &+\int_0^\infty k'^2\int_{-1}^1 N^R_{abcd}(\hat{\boldsymbol{k}},\hat{\boldsymbol{k}}',-\hat{\boldsymbol{k}}'-\hat{\boldsymbol{k}})\Lambda^{ij}_{abcd}(\hat{\boldsymbol{k}},\hat{\boldsymbol{k}})d\mathtt{a}\,dk',\end{aligned} \tag{B4a}$$

$$L_\ell^F\left(\xi_\ell^F\right) = \int_0^\infty k'^{-\xi_\ell^F} \int_{-1}^1 M_{ab}^F(\hat{\boldsymbol{k}},\boldsymbol{k}', -\boldsymbol{k}'-\hat{\boldsymbol{k}})\Lambda_{ab}^F(\hat{\boldsymbol{k}},\hat{\boldsymbol{k}}')d\mathtt{a}\,dk' + \int_0^\infty k'^2 \int_{-1}^1 N_{ab}^F(\hat{\boldsymbol{k}},\boldsymbol{k}', -\boldsymbol{k}'-\hat{\boldsymbol{k}})\Lambda_{ab}^F(\hat{\boldsymbol{k}},\hat{\boldsymbol{k}})d\mathtt{a}\,dk', \tag{B4b}$$

$$L_\ell^B\left(\xi_\ell^B\right) = \int_0^\infty k'^{-\xi_\ell^B} \int_{-1}^1 M^B(\hat{\boldsymbol{k}},\boldsymbol{k}', -\boldsymbol{k}'-\hat{\boldsymbol{k}})\Lambda^B(\hat{\boldsymbol{k}},\hat{\boldsymbol{k}}')d\mathtt{a}\,dk' + \int_0^\infty k'^2 \int_{-1}^1 N^B(\hat{\boldsymbol{k}},\boldsymbol{k}', -\boldsymbol{k}'-\hat{\boldsymbol{k}})\Lambda^B(\hat{\boldsymbol{k}},\hat{\boldsymbol{k}})d\mathtt{a}\,dk', \tag{B4c}$$

$$L_\ell^{B1}(\xi_\ell) = \int_0^\infty k'^{-\xi_\ell} \int_{-1}^1 S_{ab}(\hat{\boldsymbol{k}},\boldsymbol{k}', -\boldsymbol{k}'-\hat{\boldsymbol{k}})\Lambda_{ab}^{B1}(\hat{\boldsymbol{k}},\hat{\boldsymbol{k}}')d\mathtt{a}\,dk', \tag{B4d}$$

$$L_\ell^{B2}(\xi_\ell) = \int_0^\infty k'^{-\xi_\ell} \int_{-1}^1 S_{ab}(\hat{\boldsymbol{k}},\boldsymbol{k}', -\boldsymbol{k}'-\hat{\boldsymbol{k}})\Lambda_{ab}^{B2}(\hat{\boldsymbol{k}},\hat{\boldsymbol{k}}')d\mathtt{a}\,dk', \tag{B4e}$$

with

$$\Lambda_{abcd}^{11}(\hat{\boldsymbol{k}},\hat{\boldsymbol{k}}') = P_{ab}(\hat{\boldsymbol{k}})P_{cd}(\hat{\boldsymbol{k}}')Y_\ell(\mathtt{a}), \tag{B5a}$$

$$\Lambda_{abcd}^{12}(\hat{\boldsymbol{k}},\hat{\boldsymbol{k}}') = P_{ab}(\hat{\boldsymbol{k}})\mathcal{D}_{cdij}(\hat{\boldsymbol{k}}')\hat{k}_i\hat{k}_j\ddot{Y}_\ell(\mathtt{a}), \tag{B5b}$$

$$\Lambda_{abcd}^{21}(\hat{\boldsymbol{k}},\hat{\boldsymbol{k}}') = P_{cd}(\hat{\boldsymbol{k}}')\mathcal{D}_{abij}(\hat{\boldsymbol{k}})\hat{k}_i'\hat{k}_j'\ddot{Y}_\ell(\mathtt{a}), \tag{B5c}$$

$$\begin{aligned}\Lambda_{abcd}^{22}(\hat{\boldsymbol{k}},\hat{\boldsymbol{k}}') = {} & P_{ab}(\hat{\boldsymbol{k}})P_{cd}(\hat{\boldsymbol{k}}')\left[\left(\frac{\ell(\ell+1)}{2}\right)^2 Y_\ell(\mathtt{a}) - (\ell^2+\ell-1)\mathtt{a}\dot{Y}_\ell(\mathtt{a}) + \mathtt{a}^2\ddot{Y}_\ell(\mathtt{a})\right] \\ & + [P_{ab}(\hat{\boldsymbol{k}})P_{ci}(\hat{\boldsymbol{k}}')P_{dj}(\hat{\boldsymbol{k}}')\hat{k}_i\hat{k}_j + P_{cd}(\hat{\boldsymbol{k}}')P_{ai}(\hat{\boldsymbol{k}})P_{bj}(\hat{\boldsymbol{k}})\hat{k}_i'\hat{k}_j'] \\ & \times\left(\frac{(\ell-1)(\ell+2)}{2}\ddot{Y}_\ell(\mathtt{a}) - \mathtt{a}\dddot{Y}_\ell(\mathtt{a})\right) \\ & + [P_{ai}(\hat{\boldsymbol{k}})P_{ic}(\hat{\boldsymbol{k}}')P_{bj}(\hat{\boldsymbol{k}})P_{jd}(\hat{\boldsymbol{k}}') + P_{ai}(\hat{\boldsymbol{k}})P_{id}(\hat{\boldsymbol{k}}')P_{bj}(\hat{\boldsymbol{k}})P_{jc}(\hat{\boldsymbol{k}}')]\ddot{Y}_\ell(\mathtt{a}) \\ & + P_{ai}(\hat{\boldsymbol{k}})P_{bj}(\hat{\boldsymbol{k}})\{\hat{k}_i'\hat{k}_m[P_{jc}(\hat{\boldsymbol{k}}')P_{md}(\hat{\boldsymbol{k}}') + P_{jd}(\hat{\boldsymbol{k}}')P_{mc}(\hat{\boldsymbol{k}}')] \\ & + \hat{k}_j'\hat{k}_m[P_{ic}(\hat{\boldsymbol{k}}')P_{md}(\hat{\boldsymbol{k}}') + P_{id}(\hat{\boldsymbol{k}}')P_{mc}(\hat{\boldsymbol{k}}')]\}\dddot{Y}_\ell(\mathtt{a}) \\ & + [P_{ai}(\hat{\boldsymbol{k}})P_{bj}(\hat{\boldsymbol{k}})P_{cm}(\hat{\boldsymbol{k}}')P_{dn}(\hat{\boldsymbol{k}}')\hat{k}_i'\hat{k}_j'\hat{k}_m\hat{k}_m]\ddddot{Y}_\ell(\mathtt{a}),\end{aligned} \tag{B5d}$$

$$\Lambda_{ab}^F(\hat{\boldsymbol{k}},\hat{\boldsymbol{k}}') = P_{ai}(\hat{\boldsymbol{k}})P_{bi}(\hat{\boldsymbol{k}}')\dot{Y}_{\ell-1}(\mathtt{a}) + P_{ai}(\hat{\boldsymbol{k}})P_{bj}(\hat{\boldsymbol{k}}')\hat{k}_j\hat{k}_i'\ddot{Y}_{\ell-1}(\mathtt{a}), \tag{B5e}$$

$$\Lambda^B(\hat{\boldsymbol{k}},\hat{\boldsymbol{k}}') = Y_\ell(\mathtt{a}), \tag{B5f}$$

$$\Lambda_{ab}^{B1}(\hat{\boldsymbol{k}},\hat{\boldsymbol{k}}') = P_{ab}(\hat{\boldsymbol{k}}')Y_\ell(\mathtt{a}), \tag{B5g}$$

$$\Lambda_{ab}^{B2}(\hat{\boldsymbol{k}},\hat{\boldsymbol{k}}') = \mathcal{D}_{abij}(\hat{\boldsymbol{k}}')\hat{k}_i\hat{k}_j\ddot{Y}_\ell(\mathtt{a}). \tag{B5h}$$

Note that, for $\hat{\boldsymbol{k}} = \hat{\boldsymbol{k}}'$, i.e., for $\mathtt{a} = \hat{\boldsymbol{k}}\cdot\hat{\boldsymbol{k}}' = 1$, one has

$$\Lambda_{abcd}^{11}(\hat{\boldsymbol{k}},\hat{\boldsymbol{k}}) = P_{ab}(\hat{\boldsymbol{k}})P_{cd}(\hat{\boldsymbol{k}}), \quad \Lambda_{abcd}^{12}(\hat{\boldsymbol{k}},\hat{\boldsymbol{k}}) = 0, \quad \Lambda_{abcd}^{21}(\hat{\boldsymbol{k}},\hat{\boldsymbol{k}}) = 0,$$

$$\Lambda_{abcd}^{22}(\hat{\boldsymbol{k}},\hat{\boldsymbol{k}}) = \frac{(\ell-1)\ell(\ell+1)(\ell+2)}{8}[-P_{ab}(\hat{\boldsymbol{k}})P_{cd}(\hat{\boldsymbol{k}}) + P_{ac}(\hat{\boldsymbol{k}})P_{bd}(\hat{\boldsymbol{k}}) + P_{ad}(\hat{\boldsymbol{k}})P_{bc}(\hat{\boldsymbol{k}})],$$

$$\Lambda_{ab}^F(\hat{\boldsymbol{k}},\hat{\boldsymbol{k}}) = \frac{(\ell-1)\ell}{2}P_{ab}(\hat{\boldsymbol{k}}), \quad \Lambda^B(\hat{\boldsymbol{k}},\hat{\boldsymbol{k}}) = 1, \quad \Lambda_{ab}^{B1}(\hat{\boldsymbol{k}},\hat{\boldsymbol{k}}) = P_{ab}(\hat{\boldsymbol{k}}), \quad \Lambda_{ab}^{B2}(\hat{\boldsymbol{k}},\hat{\boldsymbol{k}}) = 0.$$

APPENDIX C: NUMERICAL METHOD

Once again, we follow [24] in order to solve numerically the 2D integrals appearing in the Eqs. (B4) giving the values of L_ℓ^*, where $*$ stands for any of ij, F, B, $B1$, and $B2$. A Newton-Cotes method of order 10 is used for the integration over $\mathtt{a}$ and a Simpson method for the integration over k'. The bounds defining the integral over k' are set to $k'_{\max} = 10^6$ and $k'_{\min} = 10^{-8}$ for $\ell = 2$, $k'_{\min} = 10^{-6}$ for $\ell = 4$, and $k'_{\min} = 10^{-4}$ for $\ell = 6$. A logarithmic repartition of points is used to discretize this interval. A number of 10^5 points is used in each direction.

As shown in Ref. [24], the integrals $L_\ell^{ij}(\xi)$ converge provided $\xi < \xi_\ell^\star = 3$ for $\ell \leqslant 2$ and $\xi < \xi_\ell^\star = \ell - 1$ for $\ell > 2$. This is also the case for L_ℓ^F, L_ℓ^{B1}, and L_ℓ^{B1}. Here L_ℓ^B only diverges for $\ell \leqslant 2$ and the convergence criterion is then $\xi < 3$. Because of this diverging behavior, the interval $[0, k'_{\min}]$ has a non-negligible contribution to the value of the integrals $L_\ell^*(\xi)$ when ξ is close to $\xi_\ell^\star$. To account for this contribution, L'vov *et al.* [24] propose to split the integrals over k' appearing in Eqs. (B4) in the form

$$L_\ell^*(\xi) = \int_0^\infty \cdots dk' = I_\ell^*(\xi) + \delta I_\ell^*(\xi),$$

with

$$I_\ell^*(\xi) = \int_{k'_{\min}}^\infty \cdots dk', \quad \delta I_\ell^*(\xi) = \int_0^{k'_{\min}} \cdots dk'.$$

The first integral is the one that is computed numerically with the method described above. The second one can be estimated analytically knowing the asymptotic behavior of the integrand. This estimate takes the form

$$\delta I_\ell^*(\xi) = \alpha_\ell^* \frac{k'^{\xi_\ell^\star - \xi}_{\min}}{\xi_\ell^\star - \xi}.$$

The values of α_ℓ^* are determined by performing a Taylor expansion of the integrands of L_ℓ^*: For $\ell = 2$,

$$\alpha_\ell^{11} = \tfrac{968}{945}, \quad \alpha_\ell^{12} = \tfrac{752}{315}, \quad \alpha_\ell^{21} = \tfrac{64}{35}, \quad \alpha_\ell^{22} = -\tfrac{752}{105}, \quad \alpha_\ell^F = \tfrac{8}{15},$$
$$\alpha_\ell^B = -\tfrac{2}{15}, \quad \alpha_\ell^{B1} = \tfrac{88}{189}, \quad \alpha_\ell^{B2} = \tfrac{44}{315};$$

for $\ell = 4$,

$$\alpha_\ell^{11} = -\tfrac{2192}{2835}, \quad \alpha_\ell^{12} = \tfrac{2192}{189}, \quad \alpha_\ell^{21} = \tfrac{128}{21}, \quad \alpha_\ell^{22} = \tfrac{7568}{63}, \quad \alpha_\ell^F = \tfrac{192}{35},$$
$$\alpha_\ell^B = 0, \quad \alpha_\ell^{B1} = \tfrac{-836}{2835}, \quad \alpha_\ell^{B2} = -\tfrac{836}{189};$$

and for $\ell = 6$,

$$\alpha_\ell^{11} = -\tfrac{721\,480}{729\,729}, \quad \alpha_\ell^{12} = -\tfrac{2\,885\,920}{104\,247}, \quad \alpha_\ell^{21} = \tfrac{24\,320}{1287}, \quad \alpha_\ell^{22} = \tfrac{20\,615\,200}{34\,749}, \quad \alpha_\ell^F = \tfrac{5120}{231},$$
$$\alpha_\ell^B = 0, \alpha_\ell^{B1} = -\tfrac{27\,590}{66\,339}, \quad \alpha_\ell^{B2} = -\tfrac{110\,360}{9477}.$$

[1] G. Boffetta and A. Mazzino, Incompressible Rayleigh-Taylor turbulence, Annu. Rev. Fluid Mech. **49**, 119 (2017).

[2] K. O. Mikaelian, Turbulent mixing generated by Rayleigh-Taylor and Richtmyer-Meshkov instabilities, Physica D **36**, 343 (1989).

[3] Y. Zhou, A scaling analysis of turbulent flows driven by Rayleigh-Taylor and Richtmyer-Meshkov instabilities, Phys. Fluids **13**, 538 (2001).

[4] M. Chertkov, Phenomenology of Rayleigh-Taylor Turbulence, Phys. Rev. Lett. **91**, 115001 (2003).

[5] S. I. Abarzhi, On fundamentals of Rayleigh-Taylor turbulent mixing, Europhys. Lett. **91**, 35001 (2010).
[6] O. Soulard, Implications of the Monin-Yaglom Relation for Rayleigh-Taylor Turbulence, Phys. Rev. Lett. **109**, 254501 (2012).
[7] W. H. Cabot and A. W. Cook, Reynolds number effects on Rayleigh-Taylor instability with possible implications for type Ia supernovae, Nat. Phys. **2**, 562 (2006).
[8] O. Soulard and J. Griffond, Inertial-range anisotropy in Rayleigh-Taylor turbulence, Phys. Fluids **24**, 025101 (2012).
[9] V. M. Canuto and M. S. Dubovikov, A dynamical model for turbulence. I. General formalism, Phys. Fluids **8**, 571 (1995).
[10] T. Ishihara, K. Yoshida, and Y. Kaneda, Anisotropic Velocity Correlation Spectrum at Small Scales in a Homogeneous Turbulent Shear Flow, Phys. Rev. Lett. **88**, 154501 (2002).
[11] Y. Kaneda and K. Yoshida, Small-scale anisotropy in stably stratified turbulence, New J. Phys. **6**, 34 (2004).
[12] J. L. Lumley, The spectrum of nearly inertial turbulence in a stably stratified fluid, J. Atmos. Sci. **21**, 99 (1964).
[13] J. L. Lumley, Similarity and the turbulent energy spectrum, Phys. Fluids **10**, 855 (1967).
[14] A. Yoshizawa, A statistical theory of thermally-driven turbulent shear flows, with the derivation of a subgrid model, J. Phys. Soc. Jpn. **52**, 1194 (1983).
[15] G. Boffetta, A. Mazzino, S. Musacchio, and L. Vozella, Kolmogorov scaling and intermittency in Rayleigh-Taylor turbulence, Phys. Rev. E **79**, 065301 (2009).
[16] J. Griffond, B.-J. Gréa, and O. Soulard, Unstably stratified homogeneous turbulence as a tool for turbulent mixing modeling, J. Fluids Eng. **136**, 091201 (2014).
[17] O. Soulard, J. Griffond, and B.-J. Gréa, Large-scale analysis of self-similar unstably stratified homogeneous turbulence, Phys. Fluids **26**, 015110 (2014).
[18] J. Griffond, B.-J. Gréa, and O. Soulard, Numerical investigation of self-similar unstably stratified homogeneous turbulence, J. Turbul. **16**, 167 (2015).
[19] A. Burlot, B.-J. Gréa, F. S. Godeferd, C. Cambon, and J. Griffond, Spectral modeling of high Reynolds number unstably stratified homogeneous turbulence, J. Fluid Mech. **765**, 17 (2015).
[20] A. Burlot, B.-J. Gréa, F. S. Godeferd, C. Cambon, and O. Soulard, Large Reynolds number self-similar states of unstably stratified homogeneous turbulence, Phys. Fluids **27**, 065114 (2015).
[21] B.-J. Gréa, A. Burlot, F. Godeferd, J. Griffond, O. Soulard, and C. Cambon, Dynamics and structure of unstably stratified homogeneous turbulence, J. Turbul. **17**, 651 (2016).
[22] K. Yoshida, T. Ishihara, and Y. Kaneda, Anisotropic spectrum of homogeneous turbulent shear flow in a lagrangian renormalized approximation, Phys. Fluids **15**, 2385 (2003).
[23] L. Biferale and I. Procaccia, Anisotropy in turbulent flows and in turbulent transport, Phys. Rep. **414**, 43 (2005).
[24] V. S. L'vov, I. Procaccia, and V. Tiberkevich, Scaling exponents in anisotropic hydrodynamic turbulence, Phys. Rev. E **67**, 026312 (2003).
[25] I. Arad, V. S. L'vov, E. Podivilov, and I. Procaccia, Anomalous scaling in the anisotropic sectors of the Kraichnan model of passive scalar advection, Phys. Rev. E **62**, 4904 (2000).
[26] I. Arad, L. Biferale, and I. Procaccia, Nonperturbative spectrum of anomalous scaling exponents in the anisotropic sectors of passively advected magnetic fields, Phys. Rev. E **61**, 2654 (2000).
[27] R. Rubinstein and Y. Zhou, Constant flux states in anisotropic turbulence, J. Fluids Eng. **136**, 060914 (2014).
[28] W. J. T. Bos, H. Touil, and J.-P. Bertoglio, Reynolds number dependency of the scalar flux spectrum in isotropic turbulence with a uniform scalar gradient, Phys. Fluids **17**, 125108 (2005).
[29] L. Mydlarski, Mixed velocity-passive scalar statistics in high-Reynolds-number turbulence, J. Fluid Mech. **475**, 173 (2003).
[30] J. H. Lienhard and C. W. Van Atta, The decay of turbulence in a thermally stratified flow, J. Fluid Mech. **210**, 57 (1990).
[31] F. S. Godeferd and C. Cambon, Detailed investigation of energy transfers in homogeneous stratified turbulence, Phys. Fluids **6**, 2084 (1994).

[32] H. Hanazaki and J. C. R. Hunt, Linear processes in unsteady stably stratified turbulence, J. Fluid Mech. **318**, 303 (1996).
[33] C. Staquet and F. S. Godeferd, Statistical modeling and direct numerical simulations of decaying stably stratified turbulence. Part 1. Flow energetics, J. Fluid Mech. **360**, 295 (1998).
[34] F. S. Godeferd and C. Staquet, Statistical modeling and direct numerical simulations of decaying stably stratified turbulence. Part 2. Large-scale and small-scale anisotropy, J. Fluid Mech. **486**, 115 (2003).
[35] M. Galmiche and J. C. R. Hunt, The formation of shear and density layers in stably stratified turbulent flows, J. Fluid Mech. **455**, 243 (2002).
[36] P. Sagaut and C. Cambon, *Homogeneous Turbulence Dynamics* (Cambridge University Press, Cambridge, 2008).
[37] M. Lesieur and S. Ossia, 3D isotropic turbulence at very high reynolds numbers: EDQNM study, J. Turbul. **1**, N7 (2000).
[38] C. Cambon and R. Rubinstein, Anisotropic developments for homogeneous shear flows, Phys. Fluids **18**, 085106 (2006).
[39] R. Rubinstein, S. Kurien, and C. Cambon, Scalar and tensor spherical harmonics expansion of the velocity correlation in homogeneous anisotropic turbulence, J. Turbul. **16**, 1058 (2015).
[40] R. G. Barrera, G. A. Estévez, and J. Giraldo, Vector spherical harmonics and their application to magnetostatics, Eur. J. Phys. **6**, 287 (1985).
[41] A. Burlot, Étude et modélisation de la turbulence homogène stratifiée instable, Ph.D. thesis, Université Lyon, 2015.
[42] G. Falkovich, Bottleneck phenomenon in developed turbulence, Phys. Fluids **6**, 1411 (1994).
[43] *Implicit Large Eddy Simulation: Computing Turbulent Fluid Dynamics*, edited by F. F. Grinstein, L. G. Margolin, and W. J. Rider (Cambridge University Press, New York, 2007).
[44] M. Boulet and J. Griffond, *Proceedings of the Tenth International Workshop on the Physics of Compressible Turbulent Mixing, Paris, 2006*, edited by M. Legrand and M. Vandenboomgaerde (CEA, Paris, 2007), pp. 33–36.
[45] S. Shanmuganathan, D. L. Youngs, J. Griffond, B. Thornber, and R. J. R. Williams, Accuracy of high-order density-based compressible methods in low Mach vortical flows, Int. J. Numer. Methods Fluids **74**, 335 (2013).
[46] K. H. Kim and C. Kim, Accurate, efficient and monotonic numerical methods for multi-dimensional compressible flows: Part II: Multi-dimensional limiting process, J. Comput. Phys. **208**, 570 (2005).
[47] E. Shima and K. Kitamura, Parameter-free simple low-dissipation AUSM-family scheme for all speeds, AIAA J. **49**, 1693 (2011).
[48] D. L. Youngs, The density ratio dependence of self-similar Rayleigh-Taylor mixing, Philos. Trans. R. Soc. A **371**, 20120173 (2013).
[49] O. Soulard, J. Griffond, and B.-J. Gréa, Influence of the mixing parameter on the second order moments of velocity and concentration in Rayleigh-Taylor turbulence, Phys. Fluids **28**, 065107 (2016).